A STUDY OF THE HOLLOW-CATHODE METAL-VAPOUR LASER DISCHARGE

Ibrahim K. Belal

A Thesis Submitted for the Degree of PhD
at the
University of St Andrews

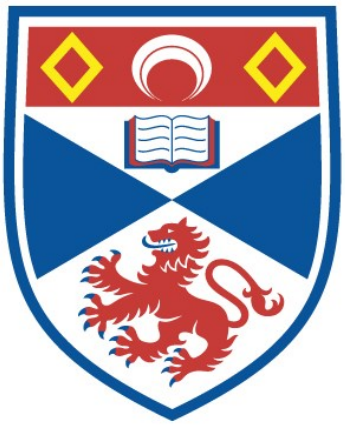

1977

A STUDY OF THE HOLLOW - CATHODE METAL - VAPOUR LASER DISCHARGE

A thesis

presented by

I K BELAL

to the

University of St Andrews

In application for the Degree of

Doctor of Philosophy

July 1977

ABSTRACT

This work is a plasma diagnostic study of the hollow cathode metal vapour laser. It can be divided into three sections.

Section one concerns the study of the basic parameters (cathode fall potential electric field, cathode fall width, negative glow length and gas temperature) of the hollow cathode discharge.

Section two concerns the use of absorption, linewidth and laser heterodyne techniques to measure the number densities of He (2^1S), (2^3S) states and He^+ ions (electrons) since these species are involved in the pumping mechanisms (Penning and Duffendack) leading to population inversions.

Section three concerns the emission radial profiles of the excited states of He I and He II so the influence of the high energy electrons which enter the negative glow from the cathode fall region can be studied as they cross the glow.

Although the metastable number densities in the hollow cathode are comparable to those in the positive column, they behave differently. In the positive column both singlet and triplet metastables saturate with respect to the discharge current. In the hollow cathode the singlets saturate not only with respect to discharge current but also with respect to pressure. On the other hand the triplets increase linearly with the discharge current and follow the cathode fall potential as a function of pressure. In the positive column the saturation of the metastable number densities with current combined with the cadmium ion drive-out to the walls lead to the laser power output limitation. In the hollow cathode cadmium ion drive-out still occurs, however this can be compensated by increasing the metal atom number density since in this case the cathode fall potential, and hence electron energy, is not thereby decreased.

Stark broadening and laser heterodyning were used to measure the ion number density and both techniques agree well. They show that the ion number density increases linearly with current and follows the cathode fall potential as a function of pressure. Also they show that the electron (ion) number density in a hollow cathode is about two orders of magnitude larger than that in a positive column which may lead to an enhancement in the Duffendack reaction.

The excitation radial profiles show that the negative glow receives a flux of electrons with energy derived directly from the cathode fall potential. These electrons play an important part in the collision processes in the negative glow. The correlation between these regions is shown clearly by studying the rate equations for different species. The behaviour of the species number densities in the negative glow with the discharge parameters can be related to the fundamental process occuring in the dark space.

DECLARATION

I hereby certify that this thesis has been composed by me, and is a record of work done by me, and has not previously been presented for a higher degree.

This research was carried out in the School of Physical Sciences, in the University of St Andrews, under the supervision of Dr M H Dunn and Dr A Maitland.

I K Belal

CERTIFICATE

We certify that Ibrahim K Belal, B.Sc, has spent nine terms at research work in the School of Physical Sciences, in the University of St Andrews, under our direction, that he has fulfilled the conditions of the Resolution of the University Court, 1967, No. 1, and that he is qualified to submit the accompanying thesis in application for the degree of Doctor of Philosophy.

M H Dunn

A Maitland

CAREER

I K Belal was born in Sheikh Saad, Tartous, Syria on 10 March 1949 and educated at Tartous Boys' High School. He was admitted to the University of Damascus and obtained the degree of BSc with Honours in Mathematics and Physics in 1972. After seven months of teaching in high schools in Tartous he came to Britain in March 1973 to study for a PhD degree at The University of St Andrews. He was awarded a S A R C scholarship in August 1974.

ACKNOWLEDGEMENTS

I am grateful to Dr M H Dunn for many lively and interesting discussions, and to Dr A Maitland for his thoughtful remarks. I would like to thank Professor J F Allen for encouraging me in the first place to come to this Department. I thank the S A R C for financial support during this work and every member of my family for giving me a good start. I am indebted to Mr R McCraw and the workshop staff for their mechanical skills, and to Miss Patricia Russell for typing the manuscript.

ABSTRACT

This work is a plasma diagnostic study of the hollow cathode metal vapour laser. It can be divided into three sections.

Section one concerns the study of the basic parameters (cathode fall potential electric field, cathode fall width, negative glow length and gas temperature) of the hollow cathode discharge.

Section two concerns the use of absorption, linewidth and laser heterodyne techniques to measure the number densities of He (2^1S), (2^3S) states and He^+ ions (electrons) since these species are involved in the pumping mechanisms (Penning and Duffendack) leading to population inversions.

Section three concerns the emission radial profiles of the excited states of He I and He II so the influence of the high energy electrons which enter the negative glow from the cathode fall region can be studied as they cross the glow.

Although the metastable number densities in the hollow cathode are comparable to those in the positive column, they behave differently. In the positive column both singlet and triplet metastables saturate with respect to the discharge current. In the hollow cathode the singlets saturate not only with respect to discharge current but also with respect to pressure. On the other hand the triplets increase linearly with the discharge current and follow the cathode fall potential as a function of pressure. In the positive column the saturation of the metastable number densities with current combined with the cadmium ion drive-out to the walls lead to the laser power output limit... ... the hollow cathode cadmium ion drive-out still occurs, however this can be compensated by increasing the metal atom number density since in this case the cathode fall potential, and hence electron energy, is not thereby decreased.

Stark broadening and laser heterodyning were used to measure the ion number density and both techniques agree well. They show that the ion number density increases linearly with current and follows the cathode fall potential as a function of pressure. Also they show that the electron (ion) number density in a hollow cathode is about two orders of magnitude larger than that in a positive column which may lead to an enhancement in the Duffendack reaction.

The excitation radial profiles show that the negative glow receives a flux of electrons with energy derived directly from the cathode fall potential. These electrons play an important part in the collision processes in the negative glow. The correlation between these regions is shown clearly by studying the rate equations for different species. The behaviour of the species number densities in the negative glow with the discharge parameters can be related to the fundamental process occuring in the dark space.

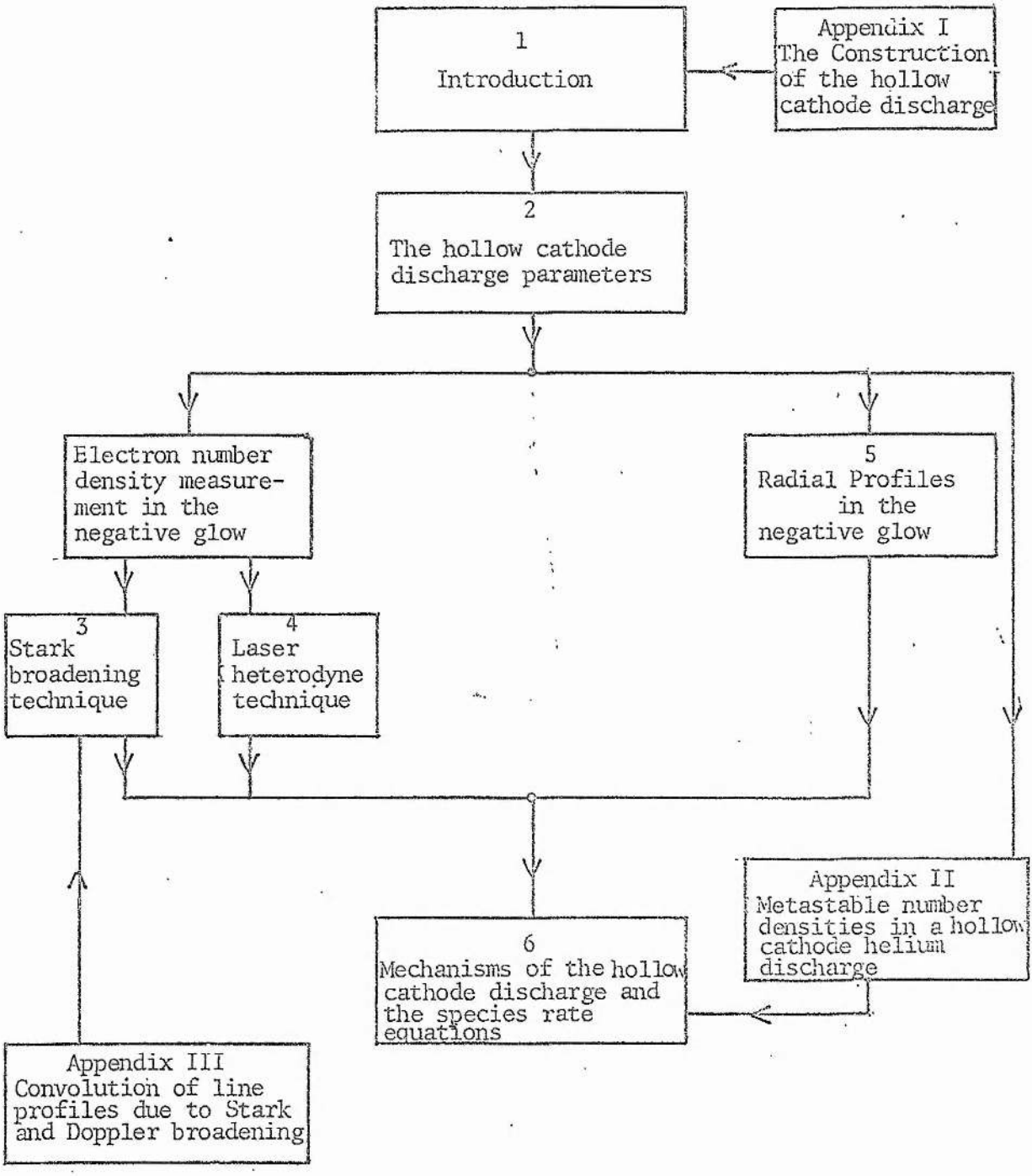

Format of the Thesis

Table of Contents

Chapter I	Introduction	1.1 - 1.9
	Figure 1.1	1.10
Chapter II	The hollow cathode discharge parameters	2.1
2.1	Introduction	2.2 - 2.3
2.2	Cathode fall potential	2.3 - 2.4
2.3	The length of the negative glow	2.4 - 2.6
2.4	The operating regime of the present discharge	2.6 - 2.8
2.5	Linewidth measurements using a scanning Fabry Perot interferometer	2.8 - 2.9
2.6	Neutral gas temperature	2.10- 2.11
	Figures 2.1 - 2.8	2.12- 2.18
Chapter III	Electron density in the negative glow, measurements using Stark broadening technique	3.1
3.1	Introduction	3.2
3.2	The validity of the general Stark broadening theory in the hollow cathode	3.3 - 3.12
3.3	The Doppler broadening of Hβ transition	3.12- 3.16
3.4	Extraction of the Stark full width at half maximum from the measured Hβ profile	3.16- 3.17
3.5	The experimental set-up and the results	3.17- 3.18
	Tables 3.1 - 3.3	3.19- 3.21
	Figures 3.1 - 3.4	3.22- 3.26
Chapter IV	Electron Density measurements using laser heterodyne technique	4.1
4.1	Introduction	4.2 - 4.3
4.2	Heterodyne technique as plasma diagnostic method	4.3 - 4.6
4.3	Laser heterodyne technique for species measurements in the hollow cathode discharge	4.6 - 4.10

4.4	The theoretical aspects of laser heterodyning	4.10
4.4.1	The general theory of laser heterodyning	4.10- 4.13
4.4.2	Conditions for optimum laser heterodyning signal	4.13
4.5	Factors affecting the stability of a laser	4.13- 4.15
4.5.1	Factors contributed by the lasers and their cavities	4.15- 4.18
4.5.2	Factors contributed by the studied discharge	4.18- 4.19
4.6	The study of the laser heterodyne in a decaying plasma	4.19- 4.22
4.7	Description of the experimental arrangement	4.22
4.7.1	The anti-vibration mount	4.23
4.7.2	The set up of the laser system	4.23- 4.24
4.7.3	The hollow cathode discharge	4.24
4.7.4	The optical arrangement for optimum heterodyne signal	4.24- 4.28
4.8	The experimental results	4.28- 4.29
4.8.1	Estimation of the ground state atoms affect on the beat shift	4.29- 4.31
4.8.2	The electron number density	4.31- 4.35
	Tables 4.1 - 4.5	4.36- 4.44
	Figures 4.1 - 4.11	4.45- 4.55
Chapter V	The emission radial profiles in the negative glow	5.1
5.1	Introduction	5.2
5.2	Apparatus	5.2 - 5.4
5.3	Factors affecting the radial profiles	5.4 - 5.5
5.4	The emission of the helium neutral and ion transitions	5.5
5.4.1	The emission as a function of the discharge current and pressure	5.5 - 5.6
5.4.2	The emission radial profiles	5.6 - 5.7

5.5	The effect of the cathode surface conditioning on the excitation in the negative glow.	5.8
5.5.1	The effect of cathode heating on the excitation of 3889 Å	5.8
5.5.2	The effect of transverse magnetic field on 3889 Å emission	5.8 - 5.9
5.6	The emission of 4416 Å and 5378 Å	5.9 - 5.10
5.7	The general features of the emission in the negative glow	5.10
	Figures 5.1 - 5.7	5.11- 5.20
Chapter VI	Mechanisms of the hollow cathode discharge and the species rate equations	6.1
6.1	Introduction	6.2 - 6.3
6.2	The mechanisms of the hollow cathode discharge	6.3 - 6.10
6.3	The general species rate equations	6.10- 6.12
6.4	The electron energy distribution in the hollow cathode discharge	6.12- 6.15
6.5	The particles number densities	6.15
6.5.1	The magnitude of the electron number density	6.15- 6.17
6.5.2	The dependence of the metastable number density on the discharge parameters.	6.17- 6.20
6.6	The excitation in the negative glow	6.20- 6.21
6.6.1	The excitation of the 3889 Å transition	6.21
6.6.2	The excitation mechanisms of 4416 Å and 5378 Å transitions	6.21- 6.24
	Table 6.1	6.25 - 6.26
Appendix I	The construction of the hollow cathode discharge	A1.1
A1.1	The construction of the hollow cathode discharge for the steady state case	A1.2-A1.3

A1.2	Description of the hollow cathode discharge and its circuit which is used in the laser heterodyne experiment	A1.3-A1.4
	Figure A1.1	A1.5
Appendix II	Metastable number densities in a hollow cathode helium discharge	A2.1
A2.1	Introduction	A2.2
A2.2	Population of He (2^3S) and He (2^1S) levels	A2.2-A2.4
A2.3	Radial profiles of metastable densities	A2.4
A2.4	Influence of cadmium on metastable densities	A2.4
	Figures A2.1 - A2.5	A2.5-A2.10
Appendix III	Convolution of line profiles due to Stark and Doppler broadening	A3.1-A3.4
	References	R.1 - R.5

Flow diagram of the physical parameters in the thesis

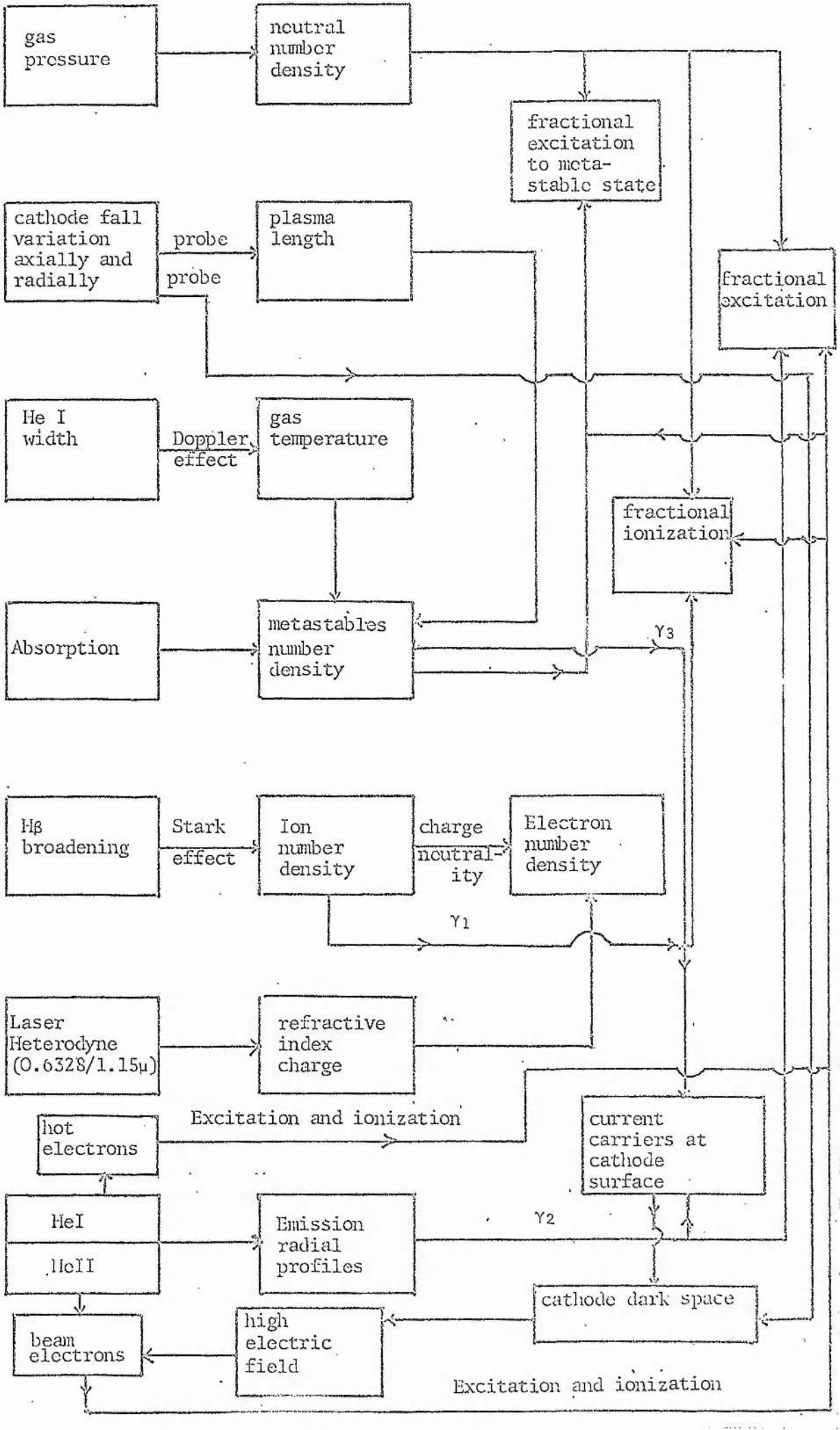

CHAPTER I

INTRODUCTION

In 1968 Silfvast[1] demonstrated continuous laser oscillation on transitions in the cadmium ion using a helium discharge seeded with the metal vapour. Due to population inversions in Cd II, laser power can be extracted at 4416 $\mathring{A}$ ($5s^2\ ^2D_{5/2} - 5p\ ^2P_{3/2}$) and 3250 $\mathring{A}$ ($5s^2\ ^2D_{3/2} - 5p\ ^2P_{1/2}$)[2]. Subsequently a large number of metal vapours (Zn, Se, Mg, Cu and Pb) were made to lase continuously in similar discharge configurations.

Metal vapour lasers are important because they offer a large variety of transitions in the visible and near infrared regions (for example 46 transitions in Se alone[3]). They can be made to lase easily using well established techniques[4], giving laser power outputs of about 10 mw - 100 mw per meter of active length.

The excitation mechanism creating population inversions between levels of the metal ion can be either the Penning ionization reaction[1-5], for example

$$He\ (2^1S,\ 2^3S) + X \rightarrow He + X^{+*} + e,$$

or the charge exchange (Duffendack[6]) reaction, for example

$$He^+ + X \rightarrow He + X^{+*},$$

where X represents the metal and X^{+*} the upper laser level in the metal ion.

In earlier metal vapour lasers, the active medium was the positive column of a conventional glow discharge. The output power of these lasers is limited by the low densities of the particles involved in the pumping process. It has been shown that the Penning ionization reaction saturates with discharge current because the metastable densities saturate with current[7]. Recently[8] it has been found that a more fundamental reason for power output limitation is the increasing cadmium ion drive-out towards the tube wall with increasing discharge

current. This causes depletion in the metal vapour density in the discharge and subsequently limits the power output.

In 1970 Schuebel[9] demonstrated continuous laser oscillation in He-Cd using a hollow cathode structure. Since then the hollow cathode discharge has been used extensively as an active medium for many rare gas-metal vapour lasers[6,10] (He-Cd, He-Zn ...).

The hollow cathode discharge is particularly advantageous due to its non-Maxwellian electron energy distribution (see Chapters V and VI), which has a large number of electrons with energies well above the ionization potential of the rare gas or the metal atoms. This promises rare gas ion densities one or two orders of magnitude larger than that of a positive column operating under the same discharge conditions. The resulting increase in the Duffendack pumped population inversions should lead to greater output power on these transitions. Another advantage of the hollow cathode discharge is that unlike the positive column the discharge is comparatively insensitive to the metal concentration (see Chapter II). Although metal ions are still driven out of the active medium (this time by the electric field of the cathode fall), the effect can be compensated by increasing the metal concentration. Hence the power limiting effect due to ion drive-out in positive column lasers can be compensated in hollow cathodes.

The hollow cathode effect can be understood by considering two planar parallel cathodes having a common anode perpendicular to their common axis. Electrons are emitted from each cathode in opposite directions. At large inter-cathode distances, each cathode has its separate, well characterized negative glow which behaves independently of the other (see figure 1.1a). For a fixed potential, as the inter-cathode distance is reduced, the two

negative glows begin to merge and finally coalesce (see figure 1.1b). The condition for merging negative glows depends on the filling gas pressure P, the cathode separation, a, and the type of the cathode material[11,12].

As the glows coalesce, the cathode current density increases by several orders of magnitude. Simultaneously the emission intensity from the negative glow increases dramatically. This is the hollow cathode effect. Moreover, the gas temperature is low, so Doppler broadening is small, hence the emitted lines are very sharp. As a result of the coalescence of the two negative glows, the cathode region of the discharge has only two parts; the dark space, close to the cathode surface and the very bright common negative glow. Furthermore when the distance between the anode and the cathode is reduced sufficiently, so the anode current is supplied by electron diffusion from the negative glow, the positive column and the anode fall regions disappear (see figure 1.1b). This is the condition in the hollow cathode laser to be described. (The discharge of interest here is inside a metal tube, and so has cylindrical geometry as shown in figure 1.1c.)

We now consider briefly the basic mechanisms taking place in a hollow cathode discharge, in particular examining how they differ from those in a conventional cold cathode discharge. The basic function of the cathode region is to facilitate the transfer of electric current from the external electrical circuit into the discharge. The current transfer can be made by positively charged particles (ions) moving to the cathode surface where they become neutralized, or by electrons being ejected from the cathode surface. The latter process requires an energy source to overcome the work function of the surface. In the case of a cold cathode this is through secondary emission processes due to bombardment of the surface by ions, photons, metastable atoms, etc.

In the dark space immediately adjoining the cathode surface there is a high electric field, resulting in a large potential difference between the cathode surface and the negative glow (cathode fall potential). The large potential difference arises because a significant multiplication of ion pairs is required in the dark space to sustain the discharge[13].

The origin of the field is a positive-ion space charge due to the initial large electron flux from the region, because of the higher electron mobility. At the cathode wall the current is carried predominantly by ions, and to a lesser extent by electrons released from the wall by secondary processes. Because of the high electric field in the dark space, the ion velocity is large. At the negative glow edge the current is carried by electrons originating from the cathode and from multiplication in the dark space. Because of the higher mobility of the electrons compared to the ions, only a small electric field is required to maintain the current flow. The changeover from high to low electric field marks the glow boundary.

From the dark space the glow receives a large flux of electrons of high energy (up to the cathode fall potential). These electrons are in two groups; primary electrons which have energy derived from the cathode fall in potential V, and secondary electrons resulting from ionization collisions in the dark space. The primary electrons advance further through the negative glow making further excitation and ionization and penetrating through the retarding potential of the other cathode. This leads to a reduction in the space charge and causes an increased current density and a lower cathode fall in potential. The secondary electrons cannot advance through the retarding field of the opposite cathode

so they lose their energy in the negative glow creating more excitation and ionization.

In the negative glow there is charge neutrality, and hence, because of their higher mobility, the electrons carry the current. Also the glow is supplied with a flux of energetic electrons from the dark space, and hence only a small residual electric field[14] is required in the glow to maintain the ionization against loss processes. Because the field is small, electron drift velocity to the anode is small, and hence under similar current density conditions the electron density (and hence ion density) in the hollow cathode glow is much higher than in a positive column situation.

As the gas pressure is increased the distance over which high energy electrons penetrate beyond the dark space decreases and hence the glow contracts. Eventually electrons cannot penetrate into the dark space of the other cathode. Further, because of the changing glow geometry the efficiency with which photons and metastables feed the secondary emission processes at either cathode diminishes. Eventually a situation is reached when the two cathodes act separately (ie normal cathodes). Because this is less efficient a higher field is required to carry a similar discharge current.

Although the above was discussed in relation to plane cathodes a cylindrical cathode can be used. The net effect is similar to the planar case, but some corrections due to geometrical considerations are required.

The present hollow cathode discharge consists of a long cylindrical tube (35 cm long, 6 mm bore) surmounted by a number of anodes (1-4) positioned at appropriate intervals along the hollow cathode structure (see figure 1.1d and Appendix I). The dimensions are characteristics of hollow cathode discharge. We have chosen the present dimensions to enable us to do probe, line profile and heterodyne measurements. Each anode is ballasted separately to ensure equal division of the total current among them. The hollow cathode structure was made from stainless steel tube to ensure an even distribution of temperature along its length. Metal vapour was introduced from a side arm located mid way along the hollow cathode structure and can be controlled independently. A flowing gas system was used to ensure a continuous purge of the system impurities and aids the distribution of metal vapour throughout the discharge region (see Appendix I).

In this thesis a plasma diagnostic study of a hollow cathode discharge will be presented. This study will concentrate on the regime which is appropriate to the He-Cd laser discharge. It covers mainly the pure helium case while the He-Cd case will be considered whenever it is necessary. This study will cover the following points:

[1] The negative glow length (Chapter II)

The hollow cathode discharge consists of a long metal tube surmounted by a number of anodes. These anodes produce a continuous plasma when neighbouring glows overlap. To study the overlapping conditions, the extent of the negative glow resulting from a single anode was measured as a function of the discharge parameters using a probe method. The extent of the negative glow is also important in determining the metastable number density by absorption methods (see below) and in determining the operating regime of the discharge.

[2] Singlet and triplet metastable densities

Because of their role in the Penning ionization it is important to know the singlet and triplet metastable densities. These number

densities are measured by an absorption technique. Using the measured absorption coefficient, the measured gas temperature, the measured plasma length and Einstein A coefficient the metastable number densities were determined (Chapter II and Appendix II).

The measured metastable number densities are comparable with those of a positive column operating under the same discharge conditions ($\sim 10^{12}$ cm^{-3}), but unlike the positive column they do not saturate with increasing discharge current, but continue increasing linearly.

[3] Helium ion density

Because of their role in creating population inversions in the upper levels of Cd^+, it is important to know the number density of the helium ions. This was determined using two different techniques, Stark broadening and laser heterodyning.

It will be shown in Chapter III and Appendix III that the Stark broadening of the Hβ transition is predominantly due to the He^+ ion. From the linewidth at half maximum, the He^+ density can be deduced. However the Stark broadening was found to be comparable to the Doppler broadening of the Hβ transition for the ion densities associated with the hollow cathode, and so it was decided to measure the ion density using an alternative technique. This is described in Chapter IV, and is based on a laser heterodyning method. This method gives the electron density from the measured laser beat shift due to the change in the refractive index of the discharge plasma.

Both techniques give similar ion number densities in the range of 10^{13} cm^{-3}, and confirm the expected two orders of magnitude increase over the positive column discharge operating under the same discharge conditions. Also they show a linear increase with current, which promises the possibility of scaling the Duffandack reaction

transitions to give larger laser output power.

[4] The radial profiles of the emission in the negative glow

The cathode dark space is the source of the high energy electrons which enter the negative glow. These electrons in making excitations as they move across the negative glow lose energy. The emissions of He I and He II transitions are expected to vary accordingly across the negative glow. To study this effect the radial profiles of He I and He II transitions were measured (Chapter V). Furthermore the dominant excitation mechanisms of the Cd II transitions 4416 Å and 5378 Å are considered by studying their radial profiles and inferring from them the dominant mechanism for each transition.

The effect of a transverse magnetic field normal to the discharge electric field on the radial profiles of the He transitions will be studied also.

[5] The theoretical analysis of the hollow cathode discharge

The plasma diagnostic study will be followed in Chapter VI by a theoretical study of the basic mechanisms taking place in a hollow cathode discharge. The measured parameters will be correlated with these mechanisms through rate equations for the different particle species. These equations show the dominant mechanisms in the hollow cathode as a laser medium.

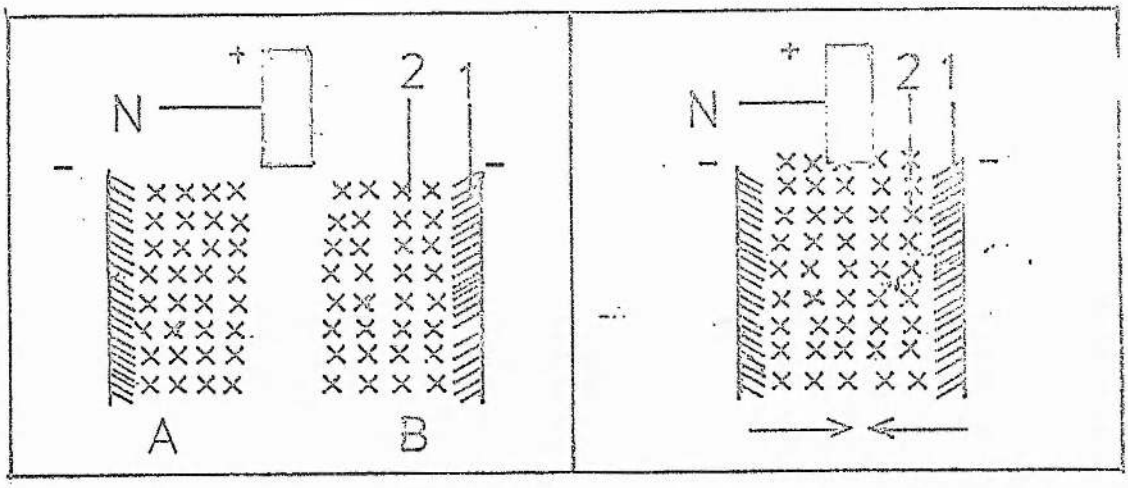

Figure 1.1a. Two plane parallel cathodes with common anode (N). When the intercathode distance is large they act as two separate discharges (A,B) each with its cathode dark space (1) and its negative glow (2).

Figure 1.1b. The intercathode distance is reduced. The two negative glows begin to merge in a common negative glow (2) and cathode dark spaces beside the walls (1). The anode (N) is immersed in the negative glow.

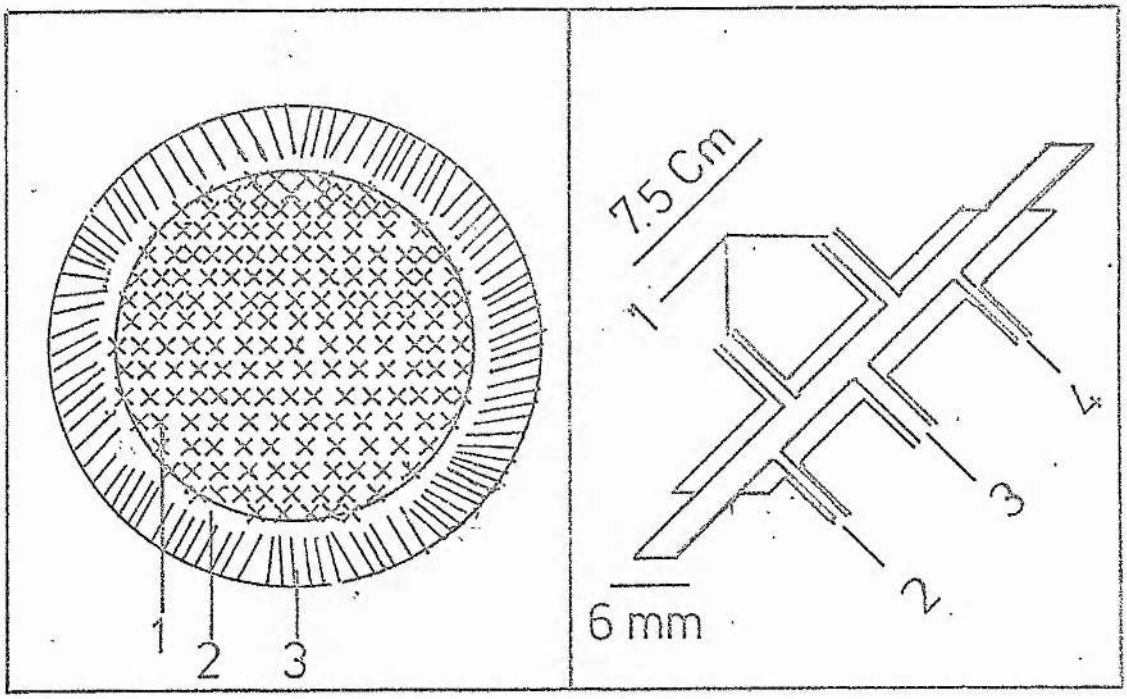

Figure 1.1c. A cross-section in the hollow cathode discharge, (1) negative glow in the centre, (2) the boundary area and (3) the cathode dark space.

Figure 1.1d. The hollow cathode structure. (1) two anodes separated by 7.5 cm, (2) gas outlet, (3) oven, and (4) gas inlet.

CHAPTER II

THE HOLLOW CATHODE DISCHARGE PARAMETERS

2.1 Introduction

This chapter considers the measurement of the cathode fall in potential, the length of the negative glow and the gas temperature in pure helium discharge.

The cathode region of the discharge is the source of the high energy electrons in the discharge. The energy of these electrons as a function of the discharge parameters can be studied by measuring the cathode fall in potential as a function of the discharge parameters.

The cathode fall in potential shows a distinctive behaviour as a function of pressure at constant current. As the pressure increases it decreases to a minimum (203 V) at low pressures (3 Torr), then increases with increasing pressure to a maximum (220 V) at 9 Torr, then decreases for further pressure increase.

The negative glow length and the gas temperature with Einstein. A coefficient will be used in Appendix II to calculate the metastable number densities from the absorption experiment. Furthermore the extent of the negative glow length is important in determining the condition for overlapping adjacent glows and in determining the operating regime of the discharge.

Measurements of the axial extent of the negative glow showed that it increases with increasing discharge current for currents $\lesssim$ 80 mA where it reaches a constant length for further increase of the current. A similar behaviour was observed when the extent of the negative glow was measured as a function of the pressure. The negative glow length was approximately constant for $p \gtrsim 4$ Torr. These measurements are used to determine the conditions for a continuous plasma and to find a criterion for the operating regime of the discharge.

The gas temperature was found to be approximately independent of the discharge current and pressure.

A detailed experimental description and theoretical analysis of the

discharge parameters will follow.

2.2 Cathode fall potential

The total voltage across the discharge was measured as a function of current and pressure. These results can be seen in figures (2.1a,b). The total voltage is made up of the cathode fall in potential V and the potential drop across the negative glow (there is no anode fall in potential, because the anode is immersed in the negative glow). Probe measurements (to be discussed in § 2.3) showed that the potential variation within the glow is very small compared to the total. Therefore the dependence of the total voltage on the discharge current and pressure in figures (2.1a,b) is interpreted as the dependence of the cathode fall in potential V on current and pressure.

Figure (2.1a) shows that the potential is independent of current for currents above 30 mA (per anode) and for pressures between 1 and 15 Torr. Figure (2.1b) shows that at constant current the potential varies in a distinctive fashion with pressure. As the pressure is increased, the potential initially falls to reach a minimum value at around 3 Torr, and then increases to reach a maximum value at around 9 Torr, before falling again for higher pressures. This characteristic behaviour was observed for all discharge currents.

Similar results were found by Thachenko and Tyutyunnik[15] in a kovar tube (30 mm bore and 180 mm long) operating under discharge conditions of 300 mA and 1 to 10 Torr. As the pressure radius product increases, the cathode fall in potential behaves similarly to that described above, taking a minimum value at 0.45cm Torr (equivalent to 1.5 Torr in our discharge) and a maximum value at 3 cm Torr (equivalent to 10 Torr in our discharge).

The above refers to the behaviour of the cathode fall in potential under stable discharge conditions, when there is a unique value of cathode fall in potential for every current and pressure value. It was observed, however, that if the discharge was initially operated under high current

conditions (> 150 mA), then on reducing the current the cathode fall in potential did not stabilize immediately but monotonically increased or decreased over periods of the order of 10-15 minutes before reaching its original stable value. This behaviour will be considered more fully in Chapter V and Appendix II.

When Cd was introduced into the discharge, the characteristic behaviour of the cathode fall in potential as a function of the discharge current or pressure did not change. However the value of the potential was increased by about 15% over that for pure helium for a Cd oven temperature range of 250-350°C. Thus the cathode fall in potential is insensitive to the metal concentration, and hence discharge limitations due to ion drive-out by the cathode fall potential can be compensated by increasing the metal concentration.

2.3 The length of the negative glow

In order to measure the axial extent of the negative glow associated with one anode a movable tungsten probe was inserted along the bore of the tube. The probe is a sharpened tungsten rod enveloped in a fused quartz sheath except for the tip (see figure 2.2a). At about 7 cm from the probe tip the quartz sheath diameter was increased gradually to 5.8 mm to facilitate vacuum sealing. Vacuum sealing was achieved by mounting a simple O ring round the quartz sheath, this being compressed by a brass fitting screwed to the discharge tube end (see figure 2.2b). When the discharge tube is under vacuum, atmospheric pressure will be exerted on the probe and force it to slide forward. To prevent this, the probe diameter at the end was increased to 11.5 mm (nearly twice the discharge tube diameter).

Mobility of the probe forwards and backwards was achieved by fastening the probe end to a horizontal optical mount which was fixed firmly on the working table. It was possible to move the probe in and out by a distance of 5 cm (this is more than half the distance between the anodes). The width of the negative glow varies as the discharge

pressure varies (see § 2.4). This width assumes a minimum value of about 0.20 cm at low pressures ($P \lesssim 1$ Torr), when the discharge is contracted to the centre of the tube. This width is large compared to the probe diameter (0.08 cm) so the probe lay inside the negative glow. At high pressures the discharge (and hence the negative glow) contracts towards the tube wall, so the probe may then be outside the negative glow. However, the axial region is equipotential with the glow, so this means the probe still gives the plasma potential of the glow. Making the probe dimensions small ensures that the plasma disturbances are small and that space charge neutrality is preserved after the insertion of the probe. This is true because the current drawn from the discharge by the probe is very small (about 20 μA; the voltage was measured with a voltmeter having an input impedance of 10 MΩ). This means that the measured potential is not the plasma potential but it differs from it by few volts (in fact it differs by the electron energy at the tube centre). When the probe is inside the negative glow it is screened from the wall, being approximately at the plasma potential. Assuming that when the probe is outside the negative glow it is at the wall potential (0V), then estimates of the negative glow length can be obtained from the probe measurements. It was found that as the probe was withdrawn from the anode (the starting point) its voltage initially remained approximately constant at the anode potential and then changed rapidly over distances of 2 mm to reach the cathode potential. The plasma boundary is therefore well defined, and the plasma length was taken as the distance from the anode to the point where the probe voltage had fallen to half the anode-cathode voltage (see figure 2.3).

Plasma length measurements as a function of pressure and current can be seen in figures (2.4a,b). At a constant current the negative glow length increases initially with increasing pressure and then for pressures $\geq$ 4 Torr this length becomes approximately independent of the pressure. At a constant pressure the plasma length increases slowly with increasing current and then it becomes approximately constant for I $\geq$ 80 mA.

These measurements were taken with only one anode operating. The interanode spacing in the present tube is 7.5 cm, and hence we see from figures (2.4a,b) that at currents above 80 mA and pressures $\geq$ 5 Torr the negative glows associated with neighbouring anodes will begin to overlap when several anodes are operating together.

The present probe is designed to measure the extent of the negative glow length which is based on detecting a large drop in the value of the potential at the boundaries of the negative glow. The probe is not sensitive enough to measure precisely the small expected value of the negative glow potential and its variations along its axis. However figure (2.3) gives an indication of the magnitude of that field (few volts/cm).

2.4 The operating regime of the present discharge

Little and von Engel[12] have considered the hollow cathode effect for the case of planar electrodes, and for helium the increase in the current density at constant cathode fall becomes apparent for (ap) values less than 5 cm Torr, where (a) is the intercathode distance and (p) is the gas pressure. In the present case the tube bore is 0.6 cm, and so for pressure less than 9 Torr the hollow cathode effect should be operative, although some correction would be expected on account of the different geometry.

At pressures less than 12 Torr, the glow emission is continuous across the tube diameter reaching a maximum value at the tube axis (see Chapter V). For pressures higher than 12 Torr the negative glow is discontinuous across the tube centre. The condition of merging glows is one criterion identified by Little and von Engel[12] as indicating the onset of the hollow cathode effect. The glow appearance is therefore consistent with the prediction of hollow cathode behaviour based on (ap) value.

For the pressure range of 1 to 20 Torr and at a current of 100 mA, J/p^2 values range from 10^{-2} A cm^{-2} Torr^{-2} to 10^{-5} A cm^{-2} Torr^{-2} respectively. Over this operating range the cathode fall in potential varies between 203 and 220 V (see figure 2.1b). In figure (2.5) experimental values of J/p^2 (corrected for the plasma length) are plotted for different (ap) values and are compared with J/p^2 to be expected from a conventional cathode[16] (Jo/p^2). It may be seen that for pressures in excess of about 10 Torr, the behaviour of the present discharge approaches that of a conventional cathode, the hollow cathode enhancement only occurring at lower pressures as expected. This means that the efficiency of the hollow cathode discharge compared with the conventional cathode, $\frac{J-Jo}{J}$, decreases by increasing the pressure.

The cathode dark space was measured using a small probe (its design is similar to the probe described in § 2.3) inserted across the discharge with a radial resolution of 0.1 mm. These measurements indicate that as the pressure decreases to about 1 Torr, the cathode dark space width d increases to a value of 0.1 cm. This is comparable in extent to the negative glow, indicating that the discharge may be operating in an obstructed mode at low pressures.

The observations on (J/p^2) values, the visual appearance of the negative glow, and the extent of the dark space indicate that at low pressures (< 3 Torr) the discharge operates in the obstructed mode, at intermediate pressures (3 - 12 Torr) as a hollow cathode, while at high pressures (> 12 Torr) it begins to operate as a normal cathode. The behaviour of the cathode fall potential (see figure 2.1b) with pressure is also consistent with the above. The rapid rise of cathode fall on going to low pressures corresponds to the onset of the obstructed mode, while the maximum in cathode fall at intermediate pressures corresponds to the transition from hollow cathode to normal cathode operation.

2.5 Linewidth measurements using a scanning Fabry-Perot interferometer

The Fabry-Perot is a multi-reflection interferometer with two plane mirrors. A parallel beam of monochromatic light (with wavelength λ) incident normally on the interferometer will be transmitted with maximum intensity when

$$\lambda = \frac{2L}{m}$$

or

$$\nu = \frac{mc}{2L} \qquad (2.5.1)$$

where L is the mirror separation, m is an integer, ν is the frequency and c is the velocity of light. In the scanning Fabry-Perot interferometer one mirror is scanned through one or more half wavelengths when the frequencies of the transmitted maxima are scanned through one or more free spectral ranges (c/2L). The linewidth of the transmitted maxima depends on the flatness, the reflectivity and the parallelism of the mirrors.

The measured line profiles were analysed using the method of Ballik[17] to extract the Doppler and Lorentzian linewidths. The

Lorentzian linewidth was taken as an indication of the finesse of the system, since it was found to be independent of plasma conditions. The value of the finesse so deduced was 13.5 (the finesse was defined as the ratio between the free spectral range and full width of the Lorentzian profile). The Fabry-Perot interferometer has two plane mirrors each with a flatness of $\frac{\lambda}{100}$ at 5000 Å and a reflectivity of 98%. One mirror was mounted on a piezoceramic transducer which could be scanned over two free spectral ranges.

The optical system can be seen in figure (2.6). A point x in the plasma is imaged by lens L_1 on to the stop A which is positioned in the focal plane of Lens L_2. In moving off or along the tube axis from the point x the gathering power of the optical system rapidly decreases since the imaging condition is no longer fulfilled. Hence the system effectively gathers light only from the vicinity of point x. The lens L_2 transforms the incident beam into a parallel beam with diameter comparable to the mirror diameters of the Fabry-Perot interferometer. The transmitted beam is focused symmetrically across a pin hole of 100 μm diameter. This arrangement gives pin hole finesse equal to 20 (the pin hole finesse is defined as the ratio of the central spot diameter to the pin hole diameter).

The studied lines were separated by a monochromator attached to a photomultiplier (see Appendix I). The photomultiplier output was displayed on an X-Y recorder as the piezoceramic was electrically scanned. A typical scan of the 5016 Å profile at 100 mA and 5.5 and 9.5 Torr can be seen in figure (2.7).

An upper limit of the instrumental width was obtained by measuring the line profile of the 4880 Å Argon transition which is close to the studied line but which has a reduced Doppler width because of the larger atomic weight.

The instrumental profile (which is assumed to be Lorentzian) must have a full width at half maxima (FWHM) less than the measured linewidth at 4880 Å. The measured linewidth of 2 GHz gives a minimum value of the finesse of about 12.5 (the free spectral range is 25 GHz).

2.6 Neutral gas temperature

It is known that the line broadening of He I transitions due to the thermal motion of the atoms (Doppler broadening) is a Gaussian and is given by

$$\frac{\Delta \nu_o}{\nu_o} = 7.16 \times 10^{-7} \left(\frac{T}{M}\right)^{\frac{1}{2}} \qquad (2.6.1)$$

where ν_o is the central frequency, $\Delta\nu_o$ is Doppler full width at half maxima and T and M are the temperature and the atomic weight of the studied species respectively. The species temperature can be calculated from the measurement of the line profile providing that natural, collisional and Stark broadenings of the studied transition are negligible.

The natural linewidth is proportional to the Einstein A coefficient and for 5016 $\mathring{A}$ is about 2.3 MHz[18]. Fugal et al[18] derived empirical relations for the widths due to the collisional broadening and showed that this broadening depends on the gas temperature and pressure. This broadening for helium transitions at the expected temperature of 600 $\mathring{K}$ and 1 to 20 Torr ranges between 10-200 MHz. The Stark effect is a function of the ion (electron) density in the plasma[19], and for 5016 $\mathring{A}$ is not significant for electron densities less than 10^{18} cm^{-3}. The electron density measurements in our plasma (see Chapter III) give electron density in the range of 10^{13} cm^{-3}, which indicate that Stark broadening in the present discharge can be ignored. We can conclude that natural, collisional, and Stark broadening effects for the transition 5016 $\mathring{A}$ can be ignored. The transition 5016 $\mathring{A}$ arises from singlet s levels so there is no hyperfine structure complications.

Since the lower level of the 5016 $\mathring{A}$ transition is the singlet metastable state 2^1S, self-absorption may be important and may distort the line shape. Hence it is necessary to estimate the likely effect of self-absorption on the line profile at 5016 $\mathring{A}$ and

consequently on the gas temperature.

For a singlet number density of 3.2×10^{11} cm^{-3} and a plasma length of 6 cm, the effect of self-absorption on the 5016 $\mathring{A}$ line profile is to increase the width by 8%. This means that if no correction were made the gas temperature would be overestimated by 16%, equivalent to 100 $\mathring{K}$.

The singlet metastable number density described in Appendix II reaches a maximum value of 3.2×10^{11} cm^{-3} at a He pressure of 1 Torr and a discharge current of 100 mA. As the pressure or current increases the 2^1S number density saturates for I > 40 mA or P > 2 Torr. Hence the above effect of the self-absorption is the maximum value which it can attain. Furthermore because of the saturation this effect does not change as the discharge current or pressure varies. Hence ignoring the effect of the self-absorption on the line profile does not change the behaviour of the gas temperature as a function of the discharge parameters, but leads to an overestimate in its magnitude by a maximum of 16%.

The gas temperature of He I measured at 5016 $\mathring{A}$ at the tube centre as a function of the discharge current and pressure can be seen in figures (2.8a,b) respectively. Within the experimental scatter (12%) there is no systematic change in temperature with either pressure or current. This conclusion is important in relating the neutral particle density to pressure and in deducing metastable number densities from the absorption experiment.

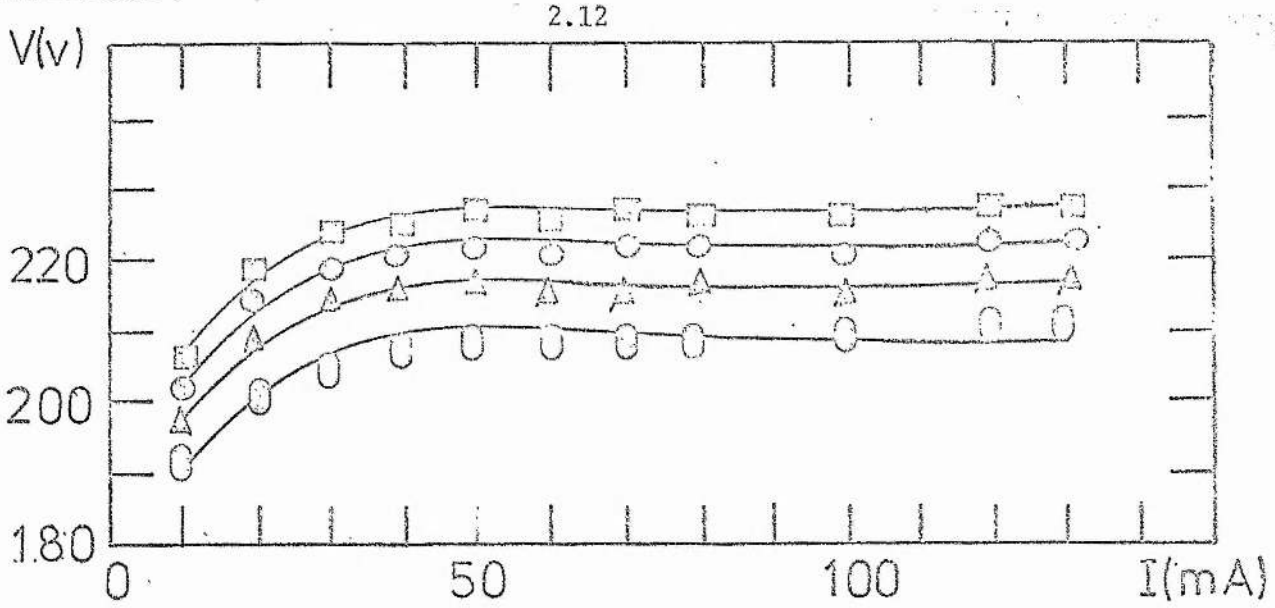

Figure 2.1a. The cathode fall potential as a function of current at different gas pressures, □1 Torr, △7 Torr, ○10 Torr and ○ 15 Torr.

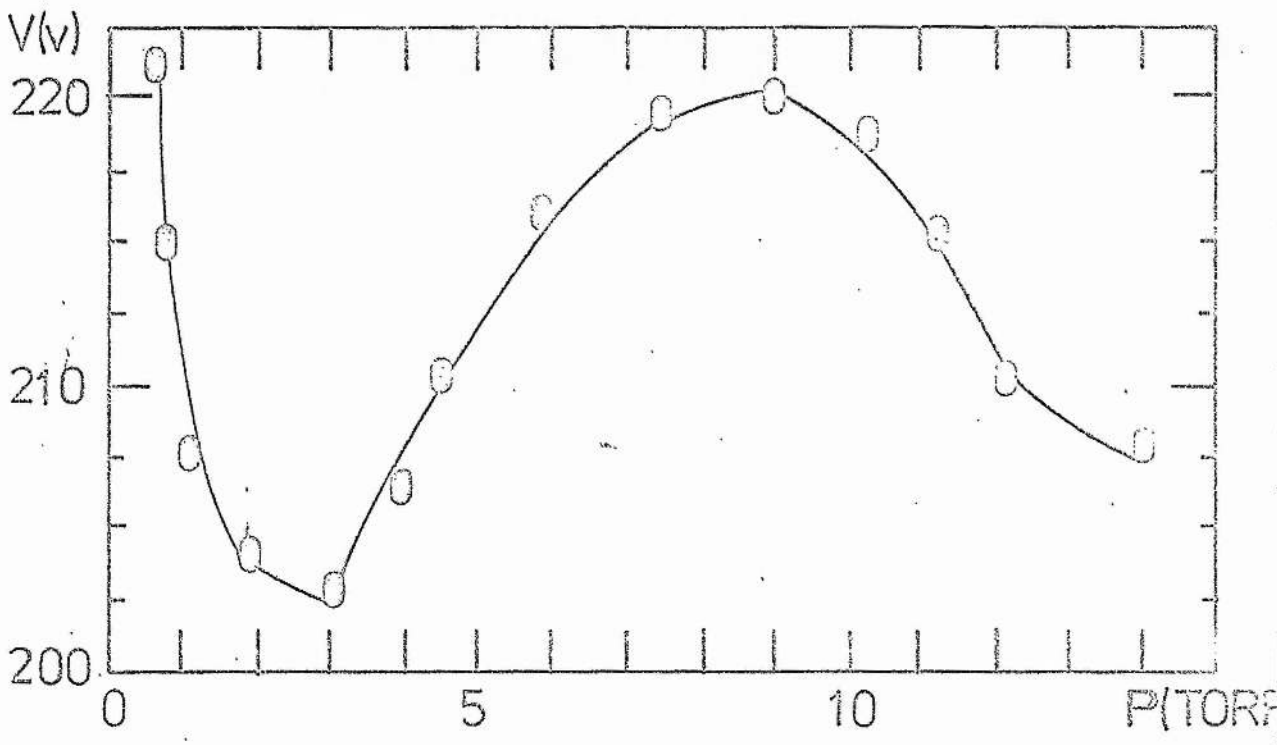

Figure 2.1b. The cathode fall potential as a function of the helium filling pressure at a constant current of 100 mA.

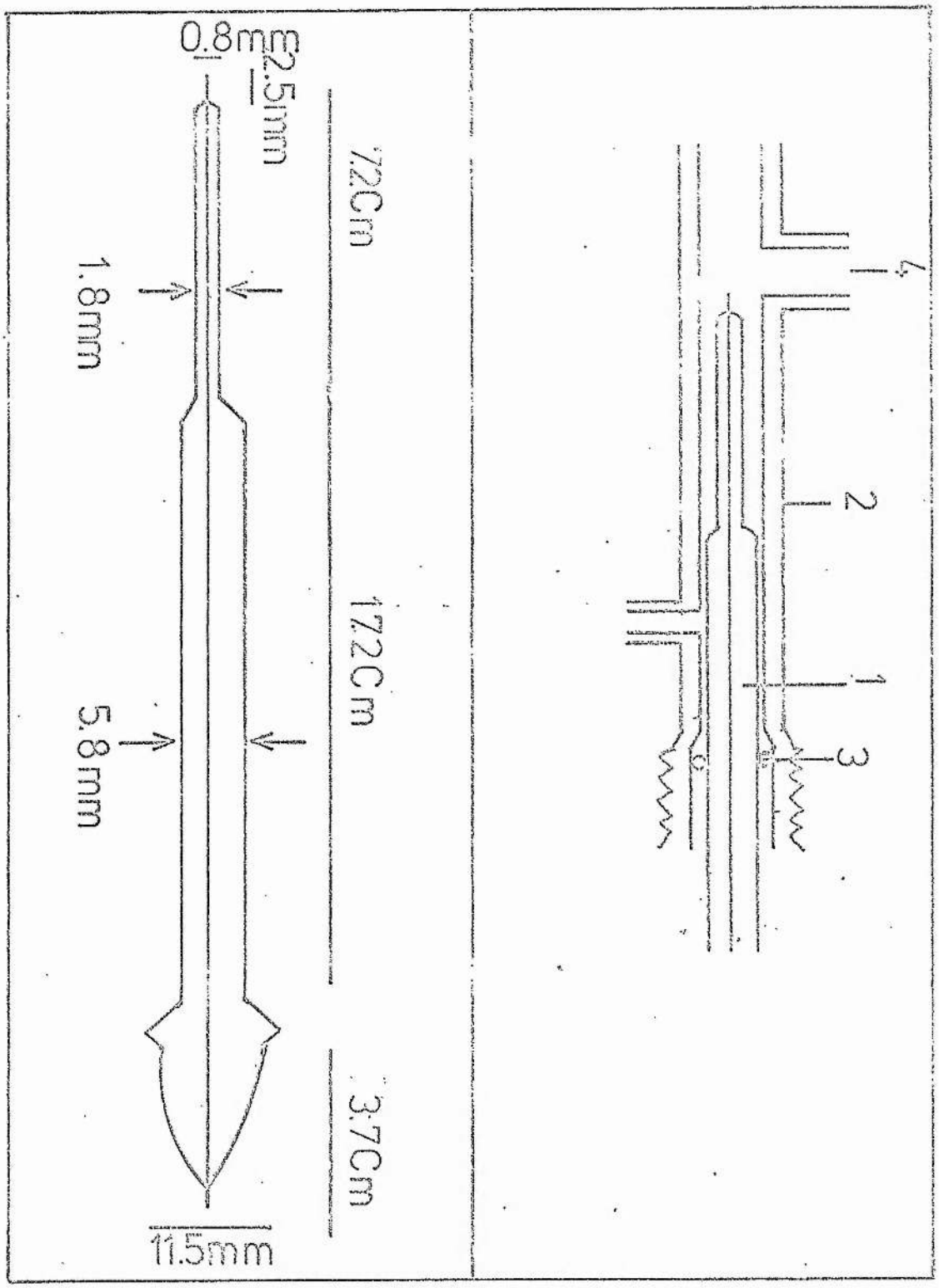

Figure 2.2a. A structure of the tungsten probe used to measure the length of the negative glow.

Figure 2.2b. The probe fitted inside the discharge. (1) probe (2) discharge and (3) O ring and (4) is the anode which was taken as the starting point.

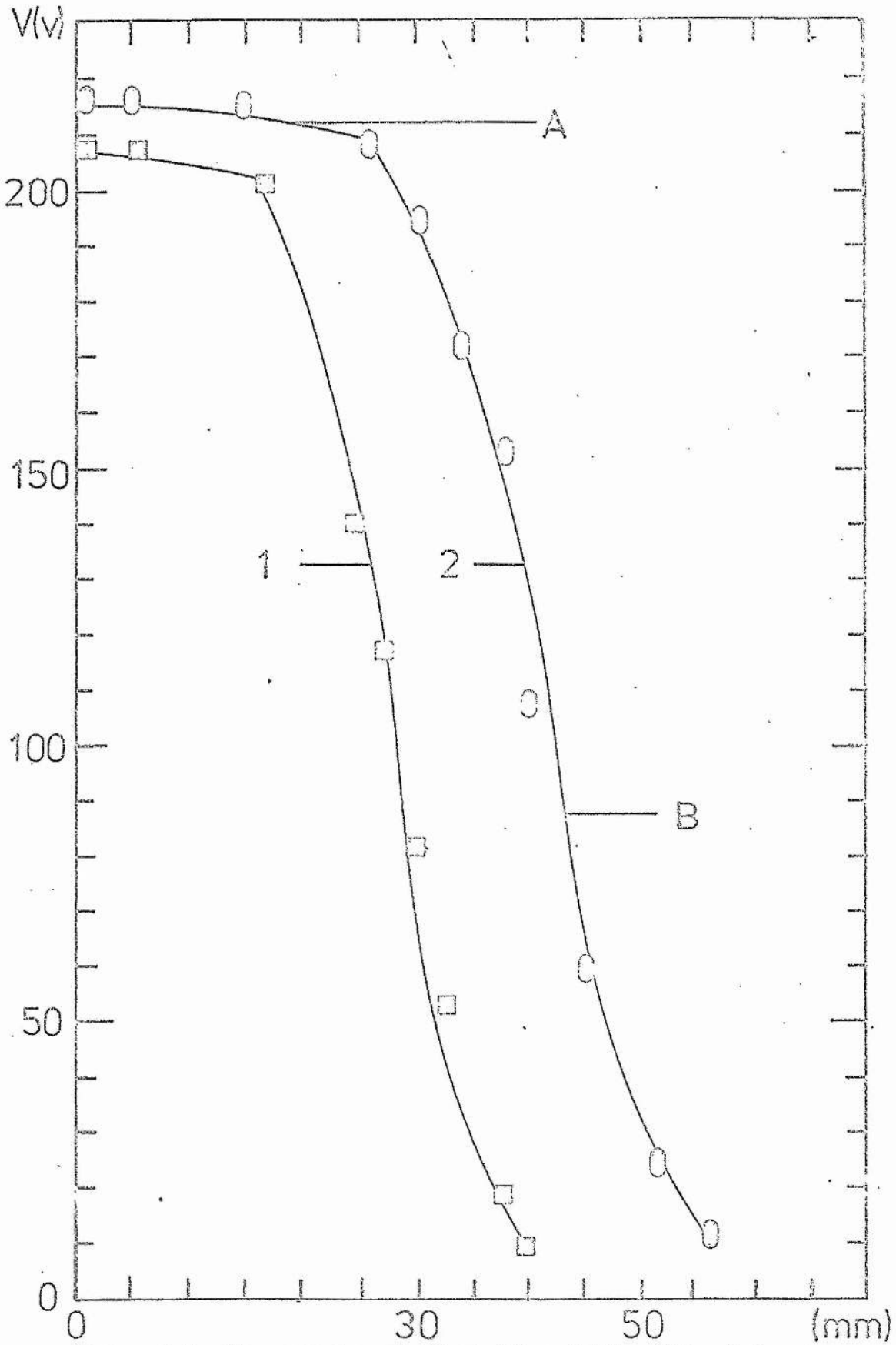

Figure 2.3. Two examples at 50 mA (1) and 100 mA(2) of the change in the discharge voltage as the probe is withdrawn from the anode. Each curve consists of two parts,(A) the probe inside the discharge and (B) the probe is outside it.

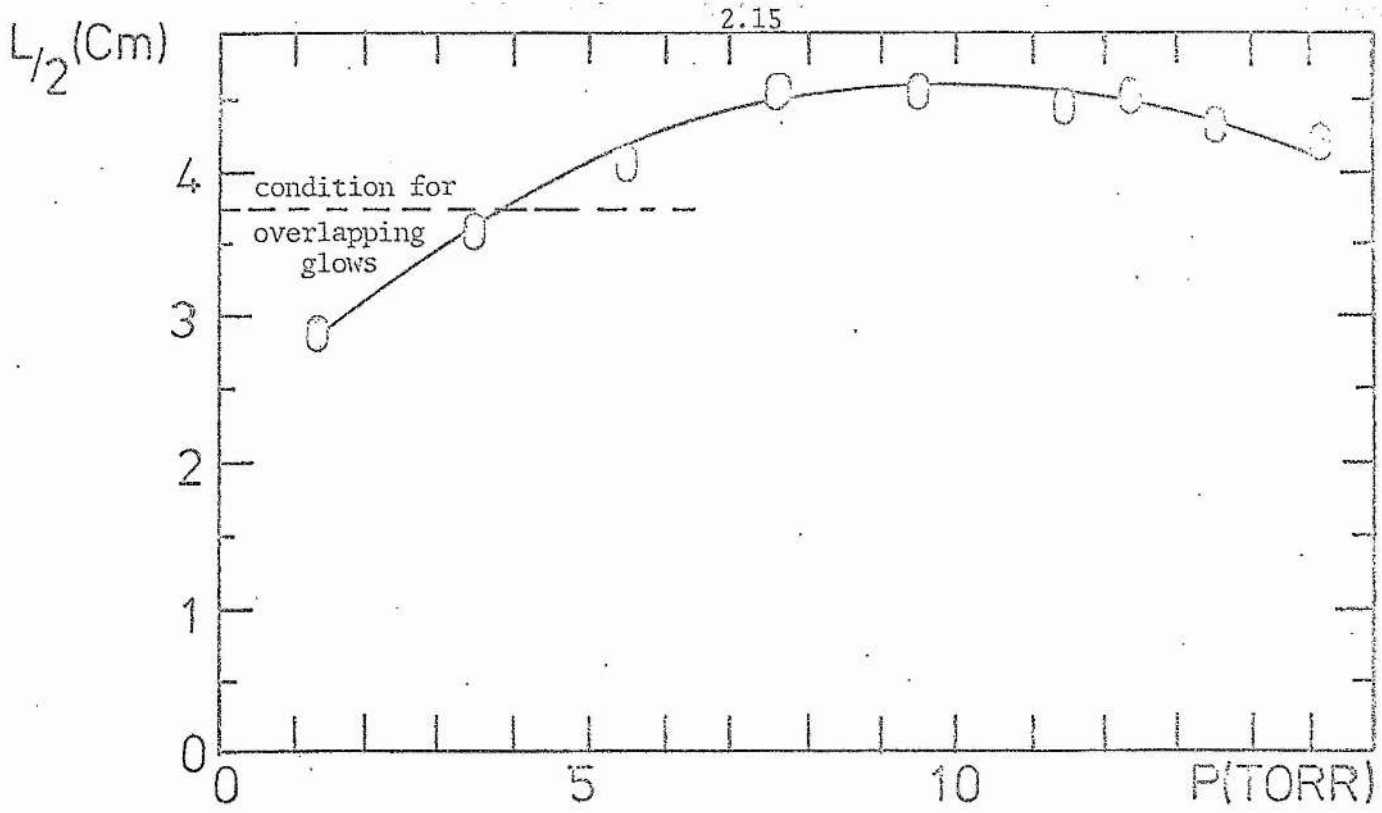

Figure 2.4a. The negative glow length measured from the anode as a function of the helium filling pressure at a constant discharge current of 100 mA.

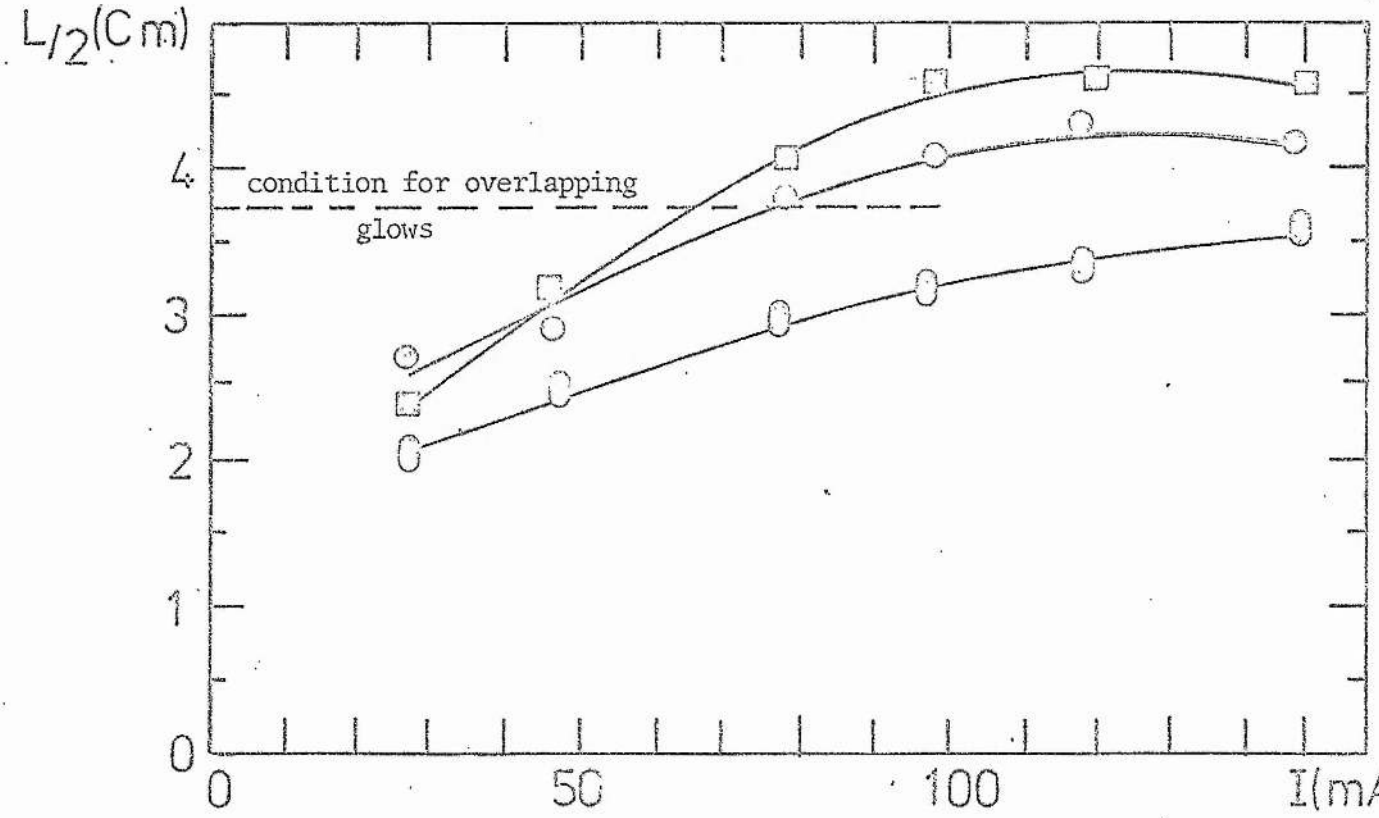

Figure 2.4b. The negative glow length measured from the anode as a function of the discharge current at different helium filling pressures ○ 1.5 Torr, ○ 5.5 Torr and □ 12.5 Torr.

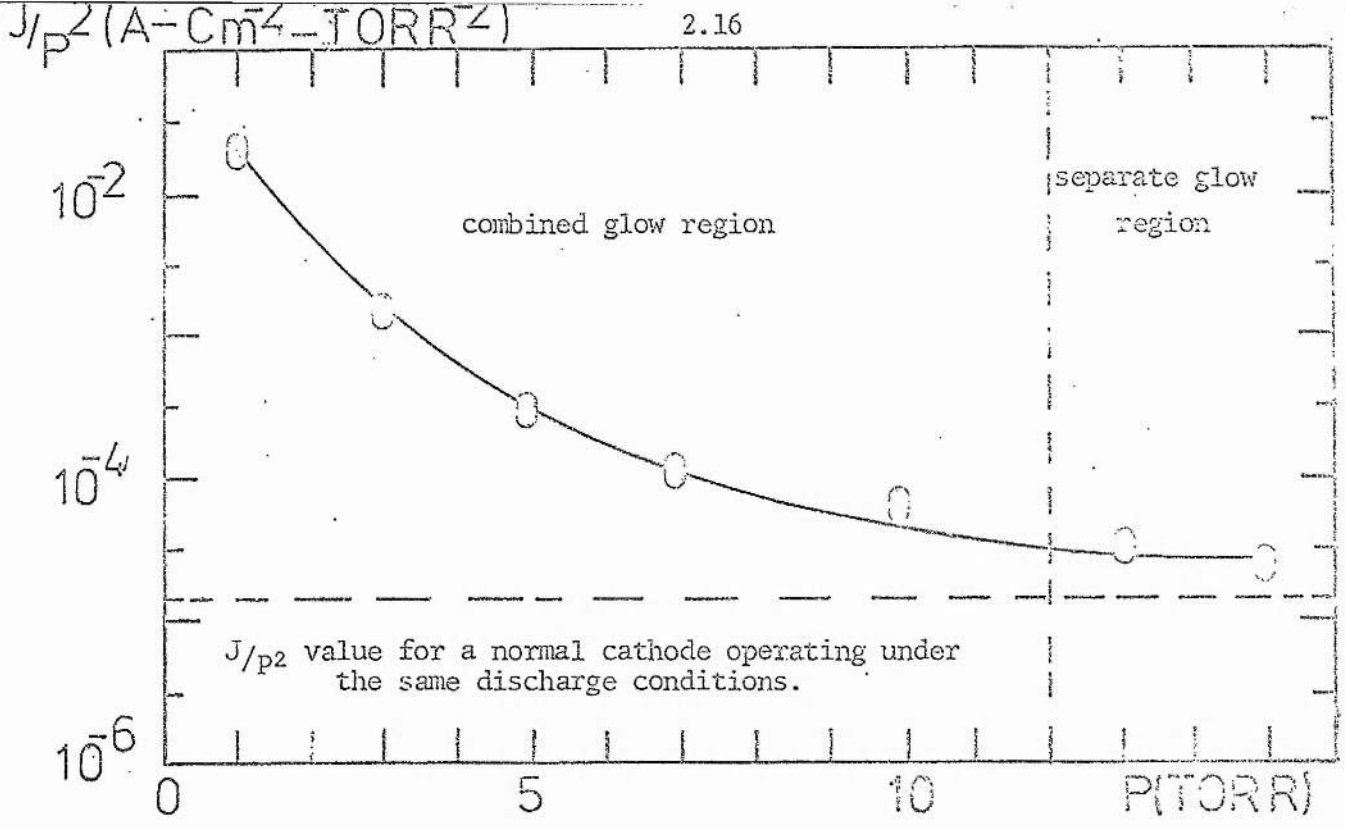

Figure 2.5. The discharge current density at the cathode (at a constant discharge current of 100 mA) as a function of the helium filling pressure.

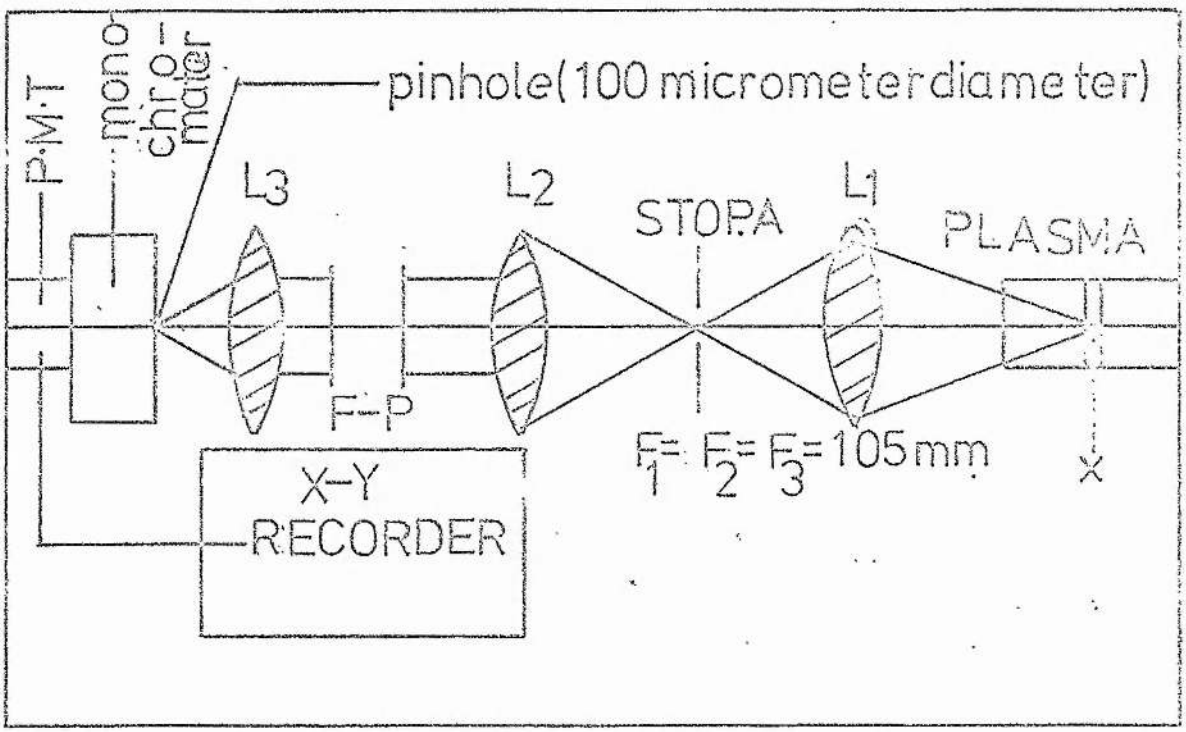

Figure 2.6. The optical arrangement used to measure the neutral gas temperature.

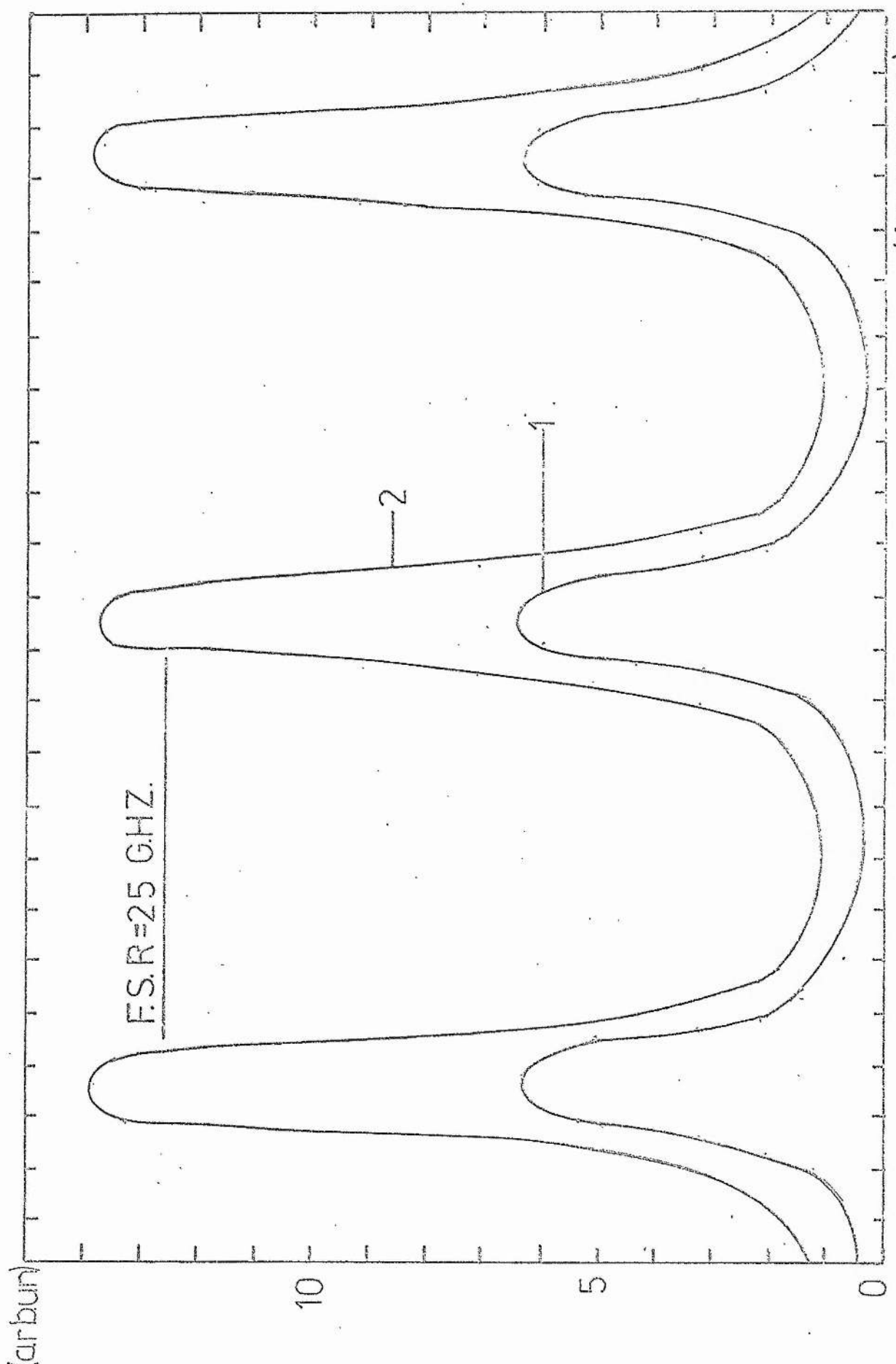

Figure 2.7. Two examples of the Fabry-Perot interferometer scan of 5016 Å at a constant discharge current of 100 mA and (1) 9.5 Torr and (2) 5.5 Torr.

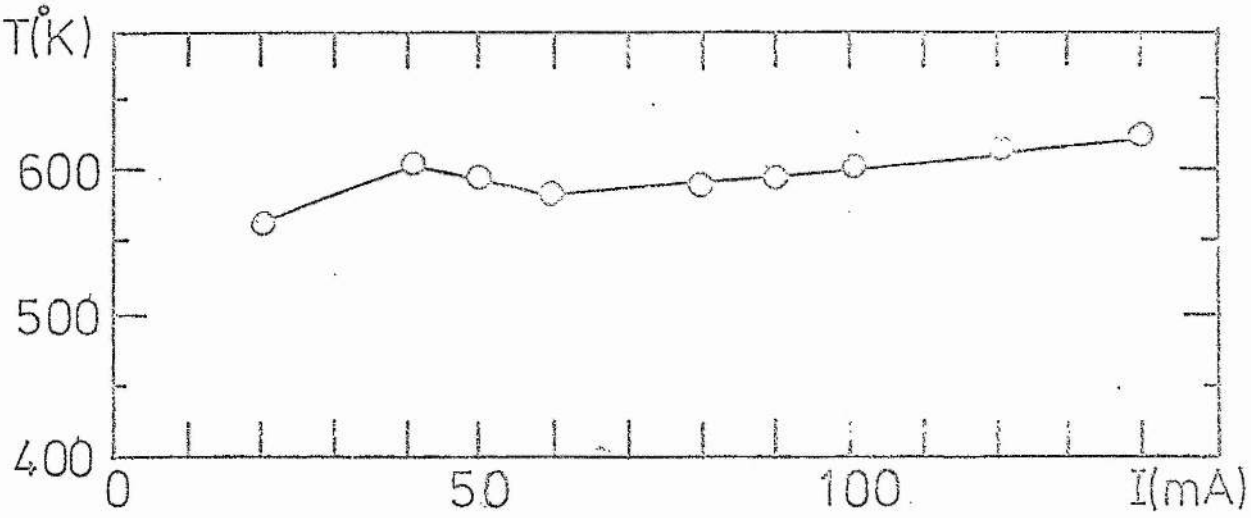

Figure 2.8a. The neutral gas temperature at the tube centre as a function of the discharge current at a constant helium filling pressure of 4.5 Torr.

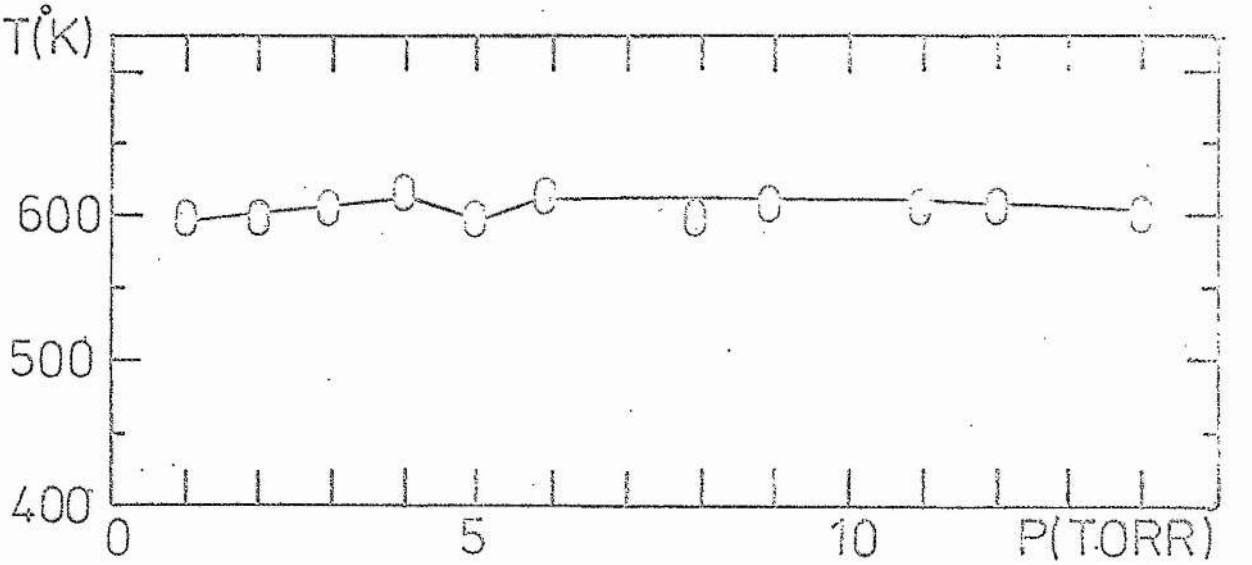

Figure 2.8b. The neutral gas temperature at the tube centre as a function of the helium filling pressure at a constant current of 100 mA.

CHAPTER III

ELECTRON DENSITY IN THE NEGATIVE GLOW MEASUREMENTS USING STARK BROADENING TECHNIQUE

3.1 Introduction

The negative glow receives a flux of electrons from the cathode dark space. These electrons move in the discharge creating more secondary electrons. Ion (and hence electron) density in the negative glow is an important parameter in assessing the Duffendack process as a population inversion mechanism.

In the following two chapters the two methods used to measure the electron density will be described. In this chapter the measurement of electron density at the tube centre by a Stark profile method is discussed. In the next chapter the laser heterodyne technique will be considered. The pure helium discharge only will be treated.

The presence of charged particles in a gas leads to local electric fields which produce Stark effects on the transitions of excited atoms. When averaged over the collection of excited atoms, this leads to a line broadening. Other broadening processes such as the Doppler effect, etc, are also present. Stark effects become increasingly significant with increasing electron (and ion) density and temperature. It will be shown in this chapter that the general theory of Stark broadening can be extended to the low electron densities and temperatures encountered in the hollow cathode laser. It was found experimentally that the Stark effect could be extracted from the measured line profiles and so was used to calculate the electron density.

Electron density calculated by this technique shows a linear increase with the discharge current (see figure 3.4a) and follows the triplet metastable number density as a function of the pressure (see figure A2.2b). Therefore the number density of electrons follows the cathode fall potential as a function of the helium filling pressure (see figures 2.1b and 3.4b).

3.2 The validity of the general Stark broadening theory in the hollow cathode

The Stark effect in a partially ionized plasma arises as a result of the interaction between the emitting atoms and the plasma local electric field. This field may result from four different but not independent phenomena.

(1) The slowly varying field of the ions (Holtsmark effect).

(2) The rapidly varying field of the electrons (electron effect).

(3) The electrons and ions provide a background which has a shielding effect on the ion field (shielding effect).

(4) The interaction of ions with each other causes a modification in their electric field (correlation effect).

In general all the above mentioned fields cause line broadening with varying degrees of importance. Their combination gives the general Stark broadening. Hence the relative contribution of ions and electrons to the Stark broadening of the line profile must be estimated.

Charge particle densities (ions and electrons) in the negative glow of the hollow cathode discharge are expected to be less than 10^{14} cm^{-3}, and as well as this a considerable proportion of the electrons are likely to be cold electrons[20] (600 ^{o}K or 0.078 eV). Theoretical treatments of Stark broadening by ions and electrons are not usually extended to such low densities and temperatures[19,21]. Accordingly the validity of the general theory of the Stark broadening in the present hollow cathode discharge must be examined. In the following the aforementioned phenomena will be considered explicitly for the case of the $H\beta$ transition.

We first of all discuss the ion broadening (effects 1, 3 and 4). Consider an emitting atom at point O (the origin). This atom (emitter) is surrounded by a large number of disturbing ions (N_i),

each of which produces an electric field at point O. If the ions were at rest, a constant electric field at O would result. Since the ions are moving then we have a time-varying electric field distribution F at O. However, the atom emits radiation in a very short time compared with the ion field variation, hence this field (unlike the electron field which is a sudden perturbation) will be static as viewed by the emitting atom. If the field due to a single ion follows a Coulomb potential, then the field distribution due to the distribution of distances between the ion and the radiating atom can be shown to be[22]

$$\Delta P(F) = \frac{3}{2F}\left(\frac{F_o}{F}\right) \exp\left[-\left(\frac{F_o}{F}\right)^{3/2}\right] dF \qquad (3.2.1)$$

where F is the electric field strength at O and F_o is a mean electric field strength which is equal to $\frac{Ze}{r_o^2}$ (Z is the number of charges on the ion and r_o is the radius of a sphere whose volume is equal to the mean volume per ion and can be taken as $(\frac{4\pi}{3})^{-\frac{1}{3}} N_i^{-\frac{1}{3}}$). Replacing the above value of r_o in F_o we get

$$F_o = 2.60\, Ze\, N_i^{\frac{2}{3}} \quad \text{(dyne)} \qquad (3.2.2)$$

Values of F_o for ion (electron) densities in the range of 10^{10} to 10^{14} cm^{-3} can be seen in table (3.1a).

The above treatment assumes that the ion density is low enough so that only one ion is responsible for the field at the radiating atom. There are two modifications that must be investigated in relation to this simple theory. Firstly, as the distance between the perturbing ion and the radiating atom increases, there is an increasing probability that the ion field will be screened by other charged particles (shielding effects). Secondly, with increasing ion density more than one ion may contribute significantly to the field at the radiating atom (correlation effect).

The field produced by an individual ion is shielded by the presence of surrounding electrons and hence the field of a given ion penetrates only a limited distance into the surrounding plasma. If there is no

emitter in the penetration range, the ion's effect is completely shielded out.

Baranger and Mozer[23,24] found that the shielding effect due to the electrons can be taken into consideration if the Debye Hückel field (or its potential) instead of the Coulomb field is used[25]

$$\underset{\sim}{F} = \frac{Ze\underset{\sim}{r}}{r^2} \left\{ \frac{1}{r} + \frac{1}{\rho_D} \right\} e^{-\frac{r}{\rho_D}} \qquad (3.2.3)$$

where ρ_D is the Debye radius and is given by the relation

$$\rho_D = \left(\frac{kT_e}{4\pi N_e e^2} \right)^{\frac{1}{2}} \quad \text{(cm)} \qquad (3.2.4)$$

They also investigated two body correlation between ions using a cluster expansion. High order correlations were neglected. The resulting electric field distribution can be seen in figures (3.1a,b). (In figures (3.1a,b,c) $H(\beta)\, d\beta$ is the probability of the electric field lying in the range β to $\beta + d\beta$). The Baranger and Mozer electric field distribution (figure 3.1a) can be looked at as two parts; the original Holtsmark field distribution and a correction term due to the electron shielding effects and ion-ion correlation effect (figure 3.1b). The Baranger and Mozer electric field distribution deviates from that of Holtsmark. The magnitude of the deviation depends on $\beta (= F/F_o)$ and $\frac{r_o}{\rho_D}$ $(0.0898\, N_i^{\frac{1}{6}}\, T_e^{-\frac{1}{2}})$. Furthermore the deviation is mainly due to the shielding of ions by electrons (see figure 3.1b). For small values of β and at constant value of $\frac{r_o}{\rho_D}$, the deviation is large (for example at $\frac{r_o}{\rho_D}$ equal to 0.8 and β equal to 0.1, the correction term is about 8 times larger than thatof Holtsmark (see figure 3.1a)) while at large values of β the correction term is small (for example for $\frac{r_o}{\rho_D}$ equal to 0.8 and β equal to 10, the correction term is about 15% of the original Holtsmark distribution (see figure 3.1b)). As β increases the deviation decreases and the Baranger and Mozer distribution approaches that of Holtsmark. The pair correlation

theory of Baranger and Mozer is valid only for values of $(\frac{r_o}{\rho_D}) < 1$. For higher values higher order terms in the cluster expansion have to be incorporated[26]. Calculations in table (3.2) show that for electron densities of 10^{10} to 10^{14} cm^{-3} and electron temperatures of 600 ^{o}K to 40000 ^{o}K, $\frac{r_o}{\rho_D}$ does not exceed 0.79 (ie on average there is at least an ion within the Debye radius of the emitting atom). This shows that in a hollow cathode discharge the Baranger and Mozer treatment of the field distribution can be used. As $\frac{r_o}{\rho_D}$ varies the full width at half maximum of the electric field distribution in comparison to that of Holtsmark varies (see figure 3.1c). For the present case, for an electron temperature of 600 ^{o}K, and an electron density of 10^{14} cm^{-3}, the variation of $\frac{r_o}{\rho_D}$ introduces 40% variation on the full width at half maximum of Baranger and Mozer distribution in comparison to that of Holtsmark. This variation must be taken into consideration when we calculate the electron density from the full width at half maximum of the measured Hβ transition.

For a transition between two levels A and B, the ion field leads to a perturbation of the Hamiltonian $(H_A(F) - H_B(F)$ which leads to a shift in the frequency[27] $\Delta \nu$

$$\Delta \nu = \frac{H_A(F) - H_B(F)}{h} = 7 \times 10^9 F, \quad \text{(Hz)} \qquad (3.2.5)$$

for the case of the Hβ transition. When this shift is averaged over all the atoms, it results in a line broadening. For electron densities between 10^{10} and 10^{14} cm^{-3}, the mean field value F_o varies between 0.006 (cgs) and 2.7 (cgs) respectively, resulting in shifts $\Delta \nu$ calculated according to (3.2.5) between 0.4 and 19 GHz respectively (see table 3.1a). The parameter β has been defined as F/F_o. From figure (3.1a) it can be seen that for $\beta < 0.1$, the probability distribution of the electric field has fallen to 1% of its maximum value, while for $\beta > 10$, it has fallen to less than 2% of its maximum value. In particular this indicates that the ion contribution at the

line centre is very small and hence the influence of electrons on the line broadening will be more pronounced here.

The effect of electrons on the line broadening depends on the nature of their collision with the emitting atoms. The type of collision depends on the magnitude of the impact parameter for the collision ρ, compared with the Debye radius ρ_D and a limiting parameter ρ_w given by[21]

$$\rho_w = (\frac{2}{3})^{\frac{1}{2}} (\frac{\hbar}{mv_e}) a^2 \qquad \text{(cm)} \qquad (3.2.6)$$

where m and v_e are the electron mass and velocity respectively and a is the principle quantum number of the studied level. Collisions may be divided into three classes: (i) strong collision, which completely disrupt the radiation process, and occur when $\rho < \rho_w$; (ii) weak collisions when $\rho_w < \rho < \rho_D$; and (iii) screened collisions when $\rho > \rho_D$, which have no effect on the emitting system.

The relative contribution to the Stark broadening of weak (ϕ_w) and strong (ϕ_s) collision is given by[21]

$$\frac{\phi_w}{\phi_s} = 2 \ln (\frac{\rho_D}{\rho_w}) \qquad (3.2.7)$$

Evaluating equation (3.2.7) using equations (3.2.4) and (3.2.6) we obtain

$$\frac{\phi_w}{\phi_s} = 2 \ln (0.46\ T_e^{\frac{1}{2}} N_e^{-\frac{1}{2}} V_e) \qquad (3.2.8)$$

In equation (3.2.8) both V_e and T_e occur; the former is introduced through the impact parameter ρ_w which refers to individual electrons, the latter comes from the expression for the Debye radius ρ_D which is based on co-operative effects and we have assumed that the average electron energy can be related to an electron temperature.

Calculations based on equation (3.2.8) for N_e in the range 10^{10} to 10^{14} cm^{-3}, T_e in the range 600 to 10^5 ^{o}K and electron velocity

V_e in the range 1.7×10^7 (0.078 eV) to 10^8 (200 eV) cm sec^{-1} showed that the ratio of strong to weak collision does not exceed 17%. The usual procedure of neglecting the influence of strong collision is therefore still valid for the expected conditions in the hollow cathode.

For very small electron velocities the limiting impact parameter ρ_w becomes comparable to the Debye radius ρ_D. The contribution of such electrons is usually neglected by terminating the electron effect on the line broadening for electron velocities less than a minimum velocity, given by equating (3.2.4) and (3.2.6) which gives

$$v_{min} = (8\pi N_e^2/3kT_e)^{\frac{1}{2}} (\hbar a^2/m). \quad (cm \ sec^{-1}) \qquad (3.2.9)$$

For an electron density of 10^{13} cm^{-3} and an electron temperature of 600 ^{o}K, v_{min} does not exceed 10^6 cm s^{-1}, which is smaller than the mean velocity of 1.7×10^7 cm s^{-1} corresponding to an electron energy of 600 ^{o}K.

Hence in the negative glow we can conclude that almost all the electrons will contribute to the line broadening, and that their contribution can be treated in terms of weak collisions as is the usual procedure.

In the negative glow of a hollow cathode discharge, the electron energy distribution differs significantly from Maxwellian, particularly for high energy electrons[28]. In the case when the broadening due to electrons results from weak electron collision then the electron contribution to the line profile[19,29] can be written as

$$\phi_{ab} = \frac{4}{3} \left(\frac{\hbar}{m} \right)^2 a^2 \frac{N_e}{V_e} \ln (0.46 \ T_e^{\frac{1}{2}} N_e^{-\frac{1}{2}} V_e) \quad (Hz) \qquad (3.2.10)$$

where the symbols assume their usual meaning. From equation (3.2.10) we can see that at constant electron temperature of 600 ^{o}K and density of 10^{14} cm^{-3} changing the electron velocity from 1.7×10^7 cm sec^{-1}

(600^{o}K or 0.078 eV) to 8.4×10^{8} cm sec^{-1} (about 10^{6} ^{o}K or 200 eV) decreases ϕ_{ab} by a factor of about 25. Also it is clear that as the energy of the electrons increases their contribution to the weak collision decreases. Also since the density of the energetic electrons is 10^{-3} less than the total density of the electrons[20] then their total contribution to the weak collisions when averaged over the electron energy distribution is negligible. The presence of non-Maxwellian electrons does not significantly distort the electronic contribution to Stark broadening.

From equation (3.2.10) we can see that for N_e in the range 10^{14} to 10^{10} cm^{-3} an electron temperature of 600 to 10^{6} ^{o}K and velocity of 1.4×10^{7} to 8.75×10^{8} cm sec^{-1}, the total electron contribution to the linewidth is about 1 GHz (see table 3.1b).

The above analysis shows that the general theory of Stark broadening can be applied to the case of low electron densities and temperature. The relative contribution of the ions and electrons to the broadening of the line profile depends on the strength of the ion electric field.

(1) $\beta < 1$ (or $F < F_o$): In this case we can say that as β decreases the electron contribution increases and it becomes comparable to the ion contribution for β equal to 0.06 or ($F = 0.06\ F_o$) at an electron density of 10^{14} cm^{-3}.

(2) $\beta \geq 1$ (or $F \geq F_o$): In this case the electron contribution assumes a maximum value of 6% of the ion contribution at an electron density of 10^{14} cm^{-3} (see tables 3.1a,b).

Since we are concerned with the overall linewidth we can say generally that the ion Stark broadening is dominant and in this case the ion density N_i is related to the full width at half maximum due to the Stark broadening $\Delta \lambda_s$ (FWHM) by the relation[19]

$$N_i = C\ (\Delta \lambda_s)^{3/2} \qquad (cm^{-3}) \qquad (3.2.11)$$

The proportionality factor C can be deduced from the above discussion as follows: we have defined earlier F_o as a normal field equal to $2.60e \times N_i^{\frac{2}{3}}$ (or $1.25 \times 10^{-9} N_i^{\frac{2}{3}}$). The two third power relation between F_o and N_i is almost true after Debye shielding and ion-ion correlation effects. The broadening of the Hβ transition can be derived from equation (3.2.5) and has a full width at half maximum $\Delta \lambda_s$ (FWHM) which is proportional to F_o, ie

$$\Delta \lambda_s = B F_o \quad (\mathring{A}) \qquad (3.2.12)$$

where B is the proportionality factor.

Introducing the value of F_o in equation (3.2.12) we get

$$\Delta \lambda_s = B \times 1.25 \times 10^{-9} N_i^{\frac{2}{3}} \quad (\mathring{A}) \qquad (3.2.13)$$

$$N_i = 2.26 \times 10^{13} B^{-\frac{3}{2}} (\Delta \lambda_s)^{3/2} \quad (cm^{-3}) \qquad (3.2.14)$$

Equation (3.2.14) is similar to equation (3.2.11) except that the proportionality constant C is replaced by $2.26 \times 10^{13} B^{-\frac{3}{2}}$. Griem[19] has calculated C for an electron density of 10^{14} cm^{-3} and an electron temperature of 5000 K ($\frac{r_o}{\rho_D} = 0.274$) assuming the Baranger and Mozer electric field distribution. The associated value of B for this case when $\Delta \lambda_s$ in (3.2.13) is defined as the full width at half maximum intensity is 0.15 $\mathring{A}$ $(cgs)^{-1}$. We have assumed in the present discharge that the expected electron density is less than 10^{14} cm^{-3}, furthermore we have assumed that most of the electrons are cool electrons with an electron temperature of 600 $\mathring{K}$. In this case $\frac{r_o}{\rho_D}$ assumes a value of 0.79. At $\frac{r_o}{\rho_D}$ of 0.79 the Baranger and Mozer electric field distribution has a full width at half maximum smaller than that at $\frac{r_o}{\rho_D}$ of 0.27 by about 25% (see figure 3.1c). This means that the factor B in our case is at most 25% smaller than that deduced by Griem[19], or in other words, in our case B is 0.113 $\mathring{A}$ $(cgs)^{-1}$.

In this case equation (3.2.14) can be written as

$$N_i = 5.9 \times 10^{14} \ (\Delta \lambda_s)^{3/2} \qquad (cm^{-3}) \qquad (3.2.15)$$

Equation (3.2.15) will be used later to calculate the electron density from the measured full width at half maximum of the Hβ profile. It must be emphasised that the calculated electron density from (3.2.15) is underestimated because of the overestimated value of B.

The previous discussion showed that the ion Stark broadening is dominant. However, since we have in the discharge, He^+, He^{++}, He_2^+ and H^+ (a small quantity of H_2 of the order of 1 m Torr was introduced and this will produce H^+ by dissociation; also some H^+ comes from the tube walls), it is necessary to estimate the contribution of each type of ion to the total ion Stark broadening. This involves knowing the respective relative number densities of H^+ and He^+, He^{++} and He^+ and He_2^+ and He^+ in the discharge. As soon as the hydrogen molecules enter the discharge they will be dissociated to H atoms (see the following paragraph). This suggests that ionization collisions between H_2 molecules and electrons which produce H^+ are negligible. (see process III in the following paragraph). Therefore the ionization collisions between H atoms and electrons are dominant. In fact this is true even if the hydrogen molecule density is larger than the hydrogen atom density. This is because the cross-section for collisions between H and electrons is more than an order of magnitude larger than the cross-section for collisions of H_2 with electrons[30] (see process III in section § 3.3).

The number density of H^+, N_{H^+} due to ionization of atomic hydrogen by electrons can be compared with the number density of He^+, N_{He^+} due to the ionization of helium by electrons using

$$\frac{N_{H^+}}{N_{He^+}} = \frac{N_e \ (E \geq 18 \text{ eV}) \ N_H \ \sigma_{e\text{-}H}}{N_e \ (E \geq 24.5 \text{ eV}) \ N_{He} \ \sigma_{e\text{-}He}} \qquad (3.2.16)$$

where N_H, N_{He} are hydrogen and helium number densities and σ's are

the ionization cross-sections for hydrogen and helium respectively. Since $(\sigma_{e-H}/\sigma_{e-He})$ is at most equal[30, 31] to 3, and since the number density of electrons which can make either ionization is almost equal, then N_{H^+}/N_{He^+} is determined by N_H/N_{He}. The operating helium pressure in the present discharge varies between 1 and 20 Torr, while the hydrogen pressure is in the range of 1 m Torr, therefore N_H/N_{He} is less than 10^{-3} and hence N_{H^+}/N_{He^+} is not more than 10^{-2}. Because of the high electron energy ($\sim$ 55 eV) required to produce He^{++}, using a similar relation to (3.2.16) we find that $N_{He^{++}}/N_{He^+}$ is about 10^{-2}, Moreover the study of the decaying plasma (Chapter IV § 4.8.2) showed that $N_{H_2^+}$ in the present discharge is negligible in the steady state situation. Therefore the only ion which contributes significantly to the ion broadening is He^+. Hence N_{He^+} can be deduced from the measured (FWHM) using equation (3.2.15).

3.3 The Doppler broadening of Hβ transition

The ion (electron) densities in the hollow cathode discharge were determined by measuring the Stark full width at half maximum of the intensity of the Hβ transition 4683 Å (n = 4 - 2). Since Hβ is broadened by Dopper effect as well as Stark effect, Stark width has to be extracted from a composite profile.

It was not possible to measure the profile of Hα transition, because it is masked by an intense neighbouring helium transition. It is therefore important to know the temperature of the hydrogen atoms in the upper state (n = 4) of the Hβ transition, so that Doppler contribution can be estimated. This estimate is complicated by the mechanism leading to the hydrogen atom production in the discharge.

The hydrogen molecules can dissociate as a result of collision with helium atoms (thermal dissociation) or electrons (collisional dissociation)[16].

The thermal dissociation of hydrogen molecules requires 4.5 eV. The helium atom average energy is equal to 0.078 eV(T_g = 600 °K). If we assume a Maxwellian distribution for the helium atoms, then the fraction of helium atoms which have energy in the range of 4.5 eV is negligible (10^{-24}), and so the thermal dissociation is negligible also.

The collisional dissociation occurs as a result of the following processes.

(I) Collision with electrons[16] which results in two hydrogen atoms in the ground state. This process occurs via the two following ways:

(a) The colliding electron with energy of 8.8 eV (at least) excites the hydrogen molecule to $1^3\Sigma_u$ state which has no potential minimum and is repulsive, then the two atoms fly apart each carrying 2.1 eV. This process has a maximum cross-section of 0.62×10^{-16} cm^2[16] for an electron energy of 12 eV.

(b) The hydrogen molecule may be excited to higher triplet levels, then cascade down to the triplet $1^3\Sigma_u$ state giving rise to UV emission eg $2^3\Sigma_g \rightarrow 1^3\Sigma_u$ (no singlet-triplet transitions are observed in hydrogen[32]). The two hydrogen atoms then fly apart as above each with 2.1 eV. This process has a cross-section much less than 0.2×10^{-16} cm^2[16].

(II) Collision between electron and hydrogen molecule which may lead to excitation in a single step to higher levels (higher than $1^3\Sigma_u$ or $2^3\Sigma_g$) as follows

$$\begin{aligned} &\text{(a)} \quad e + H_2 \rightarrow H^* + H + e \\ &\text{(b)} \quad e + H_2 \rightarrow H(n_1, \ell_1) + H(n_2, \ell_2) + e \end{aligned} \qquad (3.3.1)$$

Processes (IIa,b) are negligible in comparison to (I) since the excitation cross-sections are smaller[16] and require a high energy for excitation. Furthermore, all the excitations according to (3.3.1) cascade to the $1^3\Sigma_u$ state[32]. Hence excitation to higher levels only adds a small amount to the excitation of process (I).

III)

$$H_2 + e \rightarrow H^- + H + e \qquad (3.3.2)$$

This process has a cross-section of (0.4 - 3.2) x 10^{-18} cm^2 for electron energy in the range (22 - 50eV), so it is negligible in comparison to (I).

(IV) Collision between slow H_2^+ and H_2 by the process

$$H_2^+ + H_2 \rightarrow H_3^+ + H \qquad (3.3.3)$$

This process has a cross-section[16] equal to 1.7 x 10^{-14} cm^2, but it was found that it is small due to the low concentration of H_2^+.

From the above we see that most hydrogen molecules are likely to dissociate by collision with electrons giving two hydrogen atoms in the ground state each with kinetic energy of 2.1 eV.

Thus, as initially created the ground state hydrogen atom is 'hot'. It is important to study the dissipation of this kinetic energy, since it determines the Doppler profile of the hydrogen atom. In particular we wish to show that the atomic hydrogen, on average, thermalizes with the helium gas before it is excited to the upper level of the Hβ transition. If this is the case then a Doppler width determined by the gas temperature can be assumed for the Hβ transition.

The energy of the hydrogen atom will be lost by collisions with electrons and helium atoms. The fractional loss of energy f resulting from the elastic collision of two particles[33] with masses m_1, m_2 and energies E_1, E_2 is

$$f = \frac{2\, m_1\, m_2}{(m_1 + m_2)^2} \quad \left(1 - \frac{E_1}{E_2}\right) \qquad (3.3.4)$$

Applying this equation to the H atom we find that it loses in each collision with helium atom at least 0.4 of its energy, while it loses less than 10^{-3} of its energy in collision with electrons. From here we see that the hydrogen atom has to make at most a few collisions to thermalize with the helium atoms.

The elastic collision cross-section between hydrogen and helium atoms can be written as[34]

$$\frac{1}{\sigma_{H\text{-}He}} = \frac{1}{\pi\, r_H\, r_{He}\, (1 + \frac{V^2_{He}}{V^2_H})} \qquad (3.3.5)$$

where the r's are the radii and V's are the velocities of the particles respectively. Using this equation (the helium atom radius was taken from reference 8 and is equal to 1.85×10^{-8} cm), we find that $\sigma_{H\text{-}He}$ is 3.2×10^{-16} cm^2, which gives a collision frequency equal to 2.2×10^7 sec^{-1} at a helium pressure of 1 Torr. Excitation from the hydrogen ground state to the upper level of the Hβ transition has a maximum cross-section[35] of 2.22×10^{-18} cm^2 at an electron energy of 20 eV. Assuming that the maximum number of electrons which can excite to the upper level of Hβ transition is 10^{11} cm^{-3}, we get a collision frequency less than 10^2 sec^{-1}. This shows that the hydrogen atom makes at least 10^5 collisions with helium atom before it makes any collisions with electrons. This suggests that the hydrogen atoms thermalize and assume a temperature equal to the helium temperature before the hydrogen atom is excited by electrons and radiates on the Hβ transition.

The diffusion coefficient D_{12} for hydrogen atoms in a helium gas at NTP can be calculated from Chapman and Cowling formula[36]

$$D_{12} = \frac{3}{8\pi N_a \sigma_{12}^2} \left(\frac{kT\,(M_1 + M_2)}{\pi\, M_1\, M_2}\right)^{\frac{1}{2}} \quad (\text{cm}^2\ \text{sec}^{-1}) \qquad (3.3.6)$$

where N is the total number of atoms (helium in this case), k is Boltzman's constant, M_1, M_2 are the masses of hydrogen and helium atoms respectively and σ_{12} is the average sums of the hydrogen atom radius (0.53×10^{-8} cm) and helium atom radius (1.85×10^{-8} cm). The diffusion coefficient calculated from the above is 4.3 cm^2 sec^{-1}. Its dependence on the particle's temperature can be calculated from the simple gas kinetic theory[36]. For a gas temperature of 600 $^{\circ}$K and 1 Torr this coefficient

is 1.2×10^4 cm^2 sec^{-1}, which gives a diffusion time of about 10^{-5} sec for a discharge radius of 3 mm.

This diffusion time is at least an order of magnitude larger than the collision time between hydrogen and helium atoms and at least two orders of magnitude smaller than the collision time between electrons and hydrogen atoms which indicates that about 1% of the hydrogen atoms are excited before they diffuse. Moreover comparing the diffusion time with the radiative lifetime[37] of Hβ (3.4×10^{-8} sec) we find that Hβ radiates before it diffuses.

From the above we can say that the hydrogen atoms assume a temperature equal to the helium temperature before they are excited by electrons. So their Doppler profiles will be determined by the helium atom temperature (600 $\overset{\circ}{K}$), which gives a FWHM of 7.7 GHz for hydrogen atom.

3.4 Extraction of the Stark full width at half maximum from the measured Hβ profile

The measured line profile of Hβ is a composite profile of Stark (S_α), Doppler (D), Lorentzian (instrumental profile), natural and hyperfine splitting (HS) profiles. All these effects must be considered, before the Stark profile (full width at half maximum) can be deduced. The Hβ profile was measured using the previously described scanning Fabry-Perot interferometer which had a free spectral range of 110 GHz. The instrumental profile of the interferometer was estimated by assuming that it is equal to the measured full width at half maximum of the 4880 $\overset{\circ}{A}$ argon transition (2 GHz) which was taken as the minimum measurable linewidth (see Chapter II).

The Hβ transition has a natural line[38] width of 0.3 GHz. In addition it is split into two strong components (their ratio is 7.8:9) separated by 10.2 GHz[39], hence allowance must be made in the calculation for these effects.

As we have seen, the Stark broadening of the Hβ transition is predominantly due to He^+. The line profile due to this effect is characterized by a Holtsmark dip at its centre due to the electric field distribution (this is true even after considering the effect of shielding and correlation see figure 3.1c). For a small ion field (β in the range of 0.05) the electron effect becomes comparable to the ion effect, hence at small electric fields the depth of the dip is reduced by the electron effect. When the broadened transition due to ions and electrons is convoluted with the above effects especially Doppler and hyperfine structure the Hβ profile results.

A computer programme (IBM 360/144) was developed to generate the composite profile due to Doppler, Stark and hyperfine splitting effects (Appendix III). A typical profile is illustrated in figure (3.2). A collection of profiles were generated to investigate the influence of the various broadening processes. From these it was found that the Stark contribution (FWHM) could be extracted from the measured profile (FWHM) by subtracting a constant width due to the other effects; this having a value of 20.2 GHz for a gas temperature of 600 ^{o}K.

Typical experimental profiles are shown in figure(3.3).

3.5 The experimental set-up and the results

The experimental arrangement is similar to that used for gas temperature measurements which was described in Chapter II. Scanning of the interferometer was achieved by using the ramp output of a box car which gives scanning times in the range of 1 sec to 10 minutes. The measured profiles were taken in a scanning time of two seconds. The scanning time was chosen short to ensure that the thermal drift of the interferometer was negligible. The output signal was small due

to the small excitation rate of hydrogen in our conditions. This signal was amplified by an IC amplifier with an amplification factor of 100, and then it was displayed on the Y axis of an X-Y recorder. The X-axis of the X-Y recorder was connected to the ramp output to plot the profiles automatically. The monochromator was set up initially on the Hβ transition by using a hydrogen lamp. Following this, the Hβ signal was located precisely by bleeding H_2 into the discharge and observing the variation of Hβ as a function of H_2 pressure. A typical scan of Hβ can be seen in figure(3.3). The line profiles were measured as a function of the discharge current and pressure at the tube centre.

The ion density was then computed from the Stark width using equation (3.2.15). The extracted electron densities can be seen in figures (3.4a,b); the displayed points being averages taken over three separate measurements.

At a constant pressure the electron density increases linearly with current. At a constant current it follows the cathode fall in potential and the (2^3S)metastables in their dependence on the helium filling pressure (Appendix II).

Table (3.1a)

N_i (cm^{-3})	F_o (cgs)	ion broadening (GHz)
10^{10}	0.0058	0.04
10^{11}	0.027	0.19
10^{12}	0.125	0.88
10^{13}	0.58	4.06
10^{14}	2.7	19.00

Table (3.1b)

T_e (°K)	N_e (cm^{-3})	ϕ_{ab} (GHz)	
		V_e = 1.7×10^7 cm sec^{-1}	V_e = 8.4×10^8. cm sec^{-1}
600	10^{10}	0.00014	0.000004
	10^{11}	0.0012	0.00004
	10^{12}	0.0096	0.0003
	10^{13}	0.075	0.003
	10^{14}	0.54	0.025
10^4	10^{10}	0.00016	0.0000043
	10^{11}	0.0014	0.000040
	10^{12}	0.012	0.00040
	10^{13}	0.10	0.0031
	10^{14}	0.80	0.030
10^6	10^{10}	0.0002	0.000005
	10^{11}	0.002	0.00005
	10^{12}	0.015	0.0004
	10^{13}	0.14	0.004
	10^{14}	1.22	0.04

Table (3.2)

T_e(°K)	600	2000	10000	40000
$N_e(cm^{-3})$	$\frac{r_o}{\rho_D}$	$\frac{r_o}{\rho_D}$	$\frac{r_o}{\rho_D}$	$\frac{r_o}{\rho_D}$
10^{10}	0.17	0.09	0.04	0.023
10^{11}	0.25	0.14	0.06	0.033
10^{12}	0.37	0.20	0.09	0.044
10^{13}	0.54	0.29	0.13	0.0730
10^{14}	0.79	0.43	0.19	0.110

Table (3.3)

T_e (°K)	N_e (cm^{-3})	Weak to Strong Collision Ratio	
		$v_e = 1.7 \times 10^7$ cm sec^{-1}	ve = 8.4×10^8 cm sec^{-1}
600	10^{10}	15	22.9
	10^{11}	13	20.6
	10^{12}	10.5	18.3
	10^{13}	8.2	16.0
	10^{14}	5.9	13.7
10^4	10^{10}	17.9	25.7
	10^{11}	15.6	23.4
	10^{12}	13.3	21.1
	10^{13}	11.0	18.8
	10^{14}	8.7	16.5
10^6	10^{10}	22.5	30.3
	10^{11}	20.2	28.0
	10^{12}	17.9	25.7
	10^{13}	15.6	23.4
	10^{14}	13.3	21.1

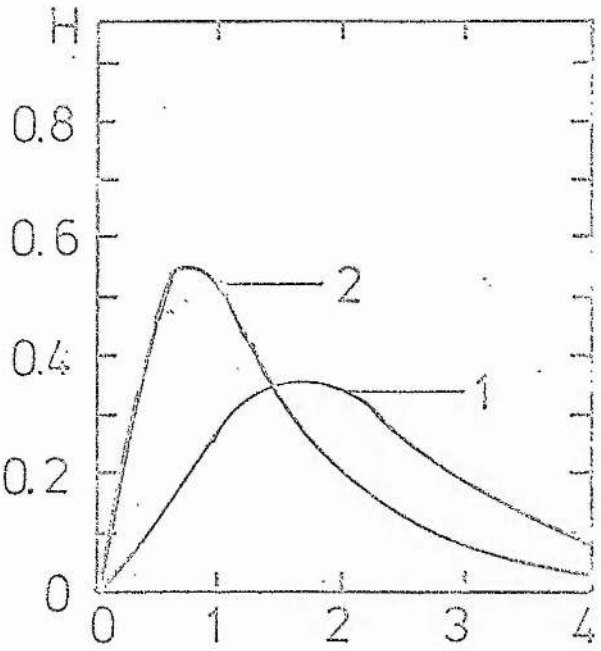

Figure 3.1a. The electric field distribution H as a function of β ($=F/F_0$), (1) Holtsmark ($r_o/\rho_D = 0$) and (2) Baranger and Mozer[23,24] distribution for $r_o/\rho_D = 0.8$.

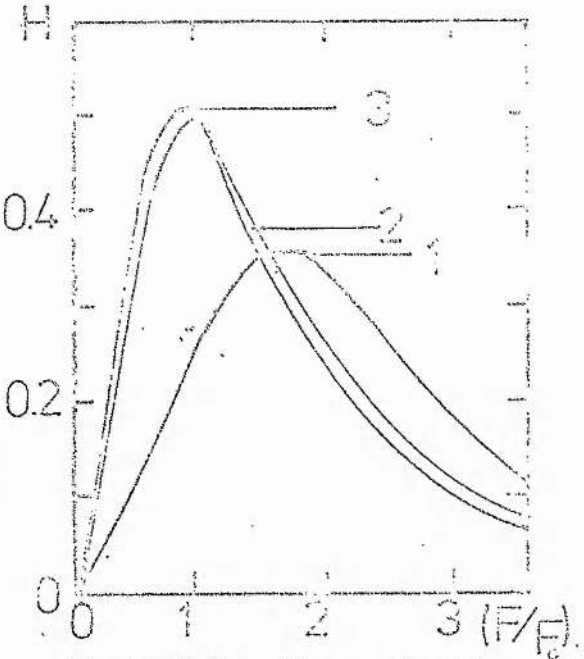

Figure 3.1b. H as a function of β (1) Holtsmark, (2 and 3 are taken from Baranger and Mozer for $r_o/\rho_D = 0.6$.) (2) H without pair correlation, (3) Baranger and Mozer distribution taking into consideration electron shielding and ion correlation.

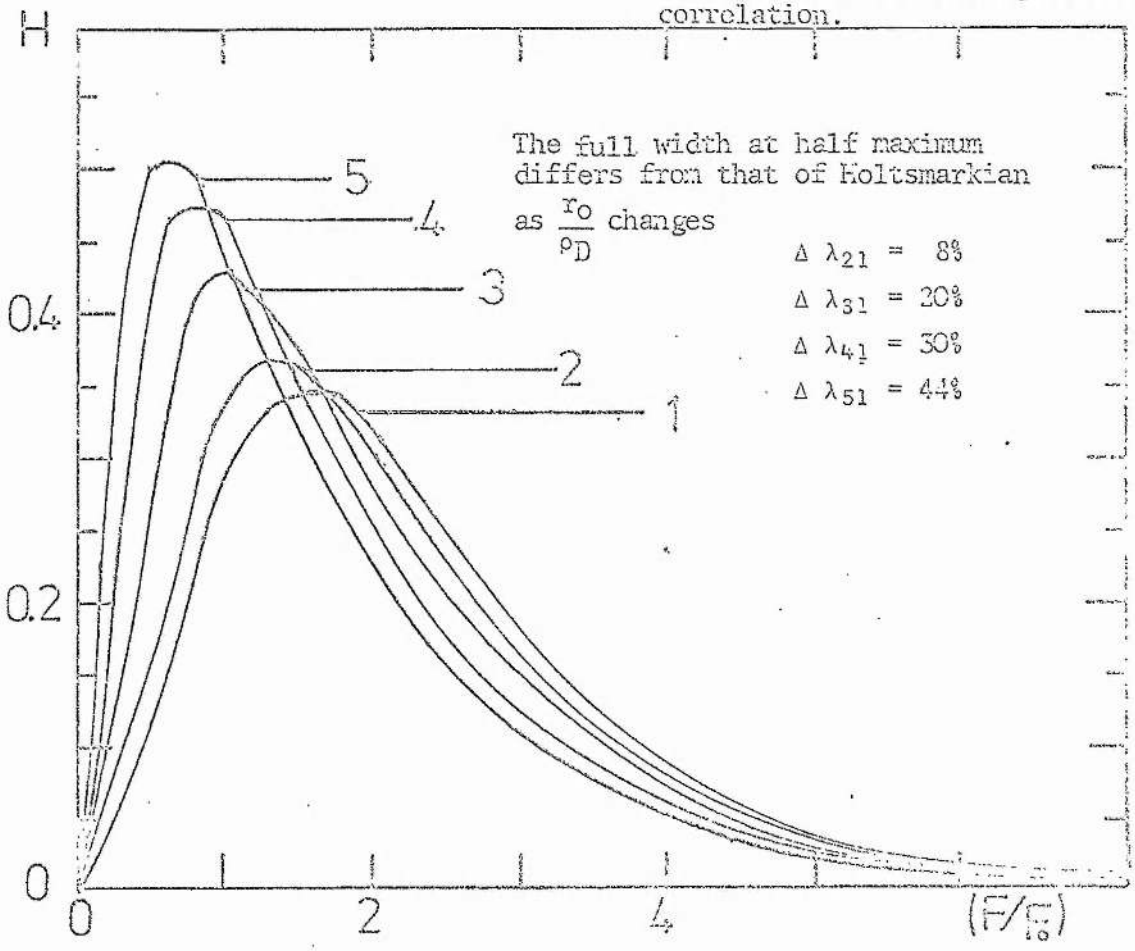

Figure 3.1c. The electric field distribution plotted as a function of β, from different values of r_o/ρ_D, (1) 0, (2) 0.2, (3) 0.4, (4) 0.6 and (5) 0.8. (These are taken from Baranger and Mozer.)

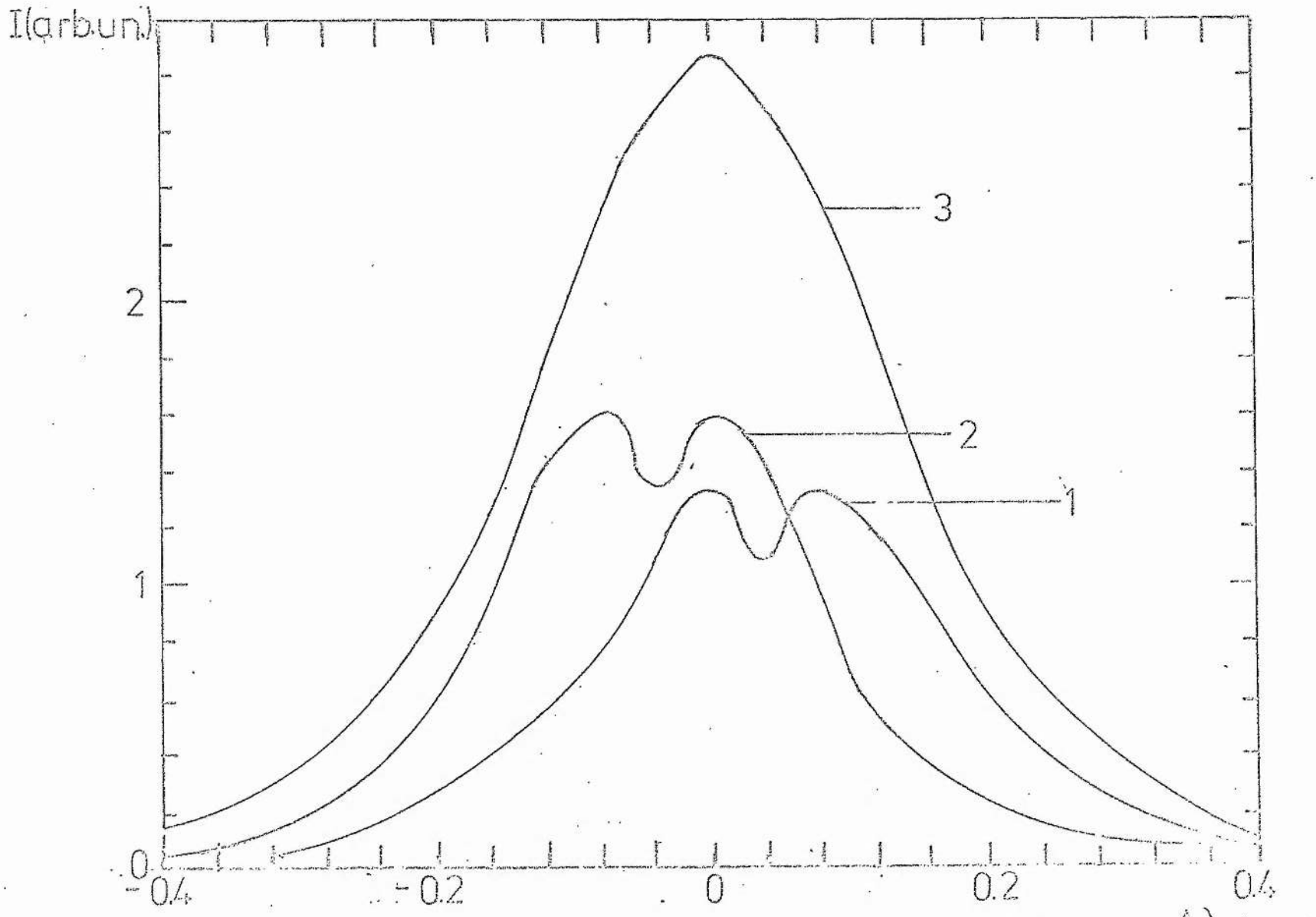

Figure 3.2. An illustration of the computer convolution of Stark and Doppler on each of the splitting components of H_β (1,2) and their combination (3). Notice the disappearance of the dip on (3). ($\Delta\lambda/F_o$ is the reduced wavelength, see Griem[19] and Appendix 3).

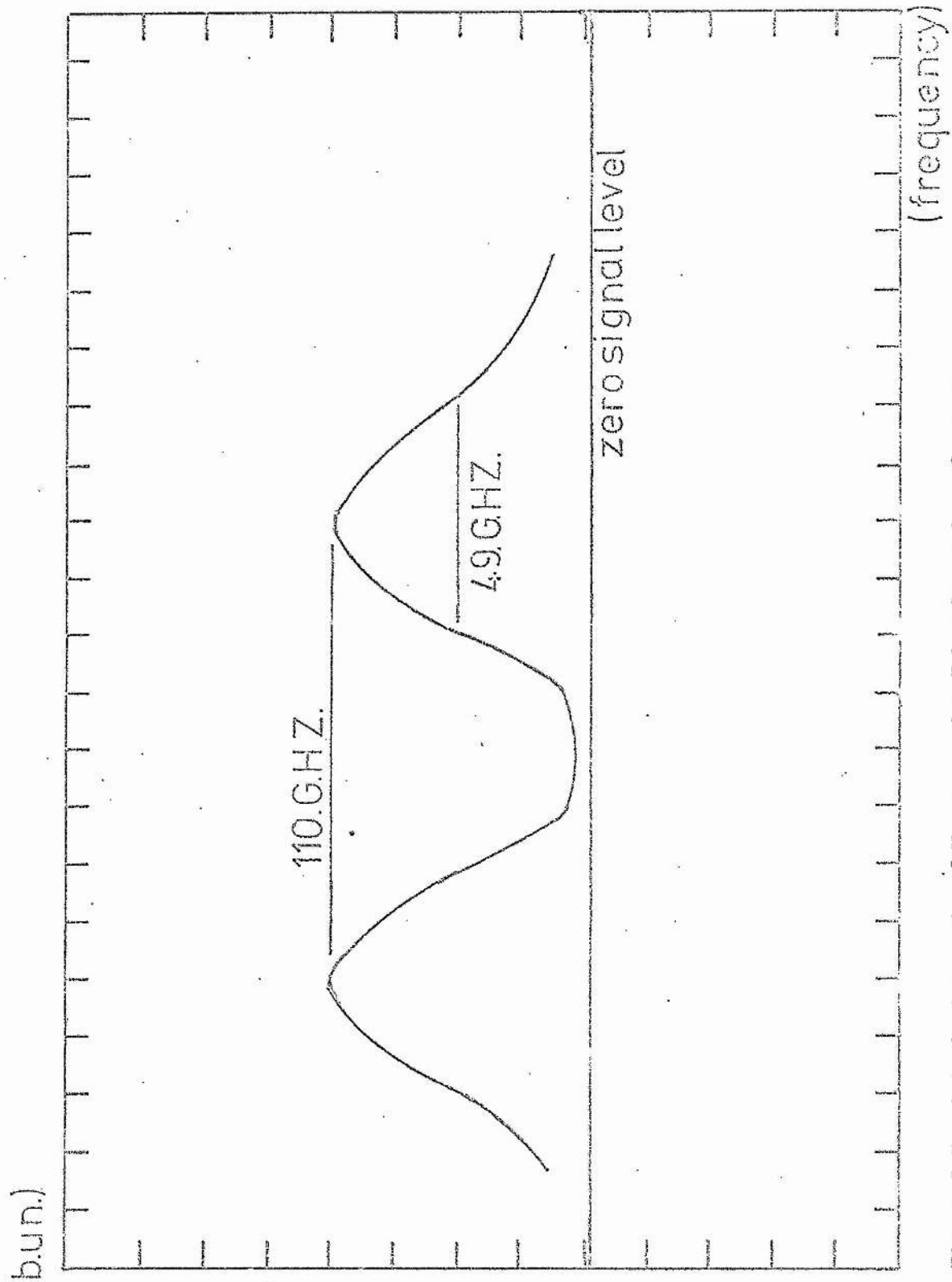

Figure 3.3. A typical example of Hβ scan using Fabry-Perot interferometer.

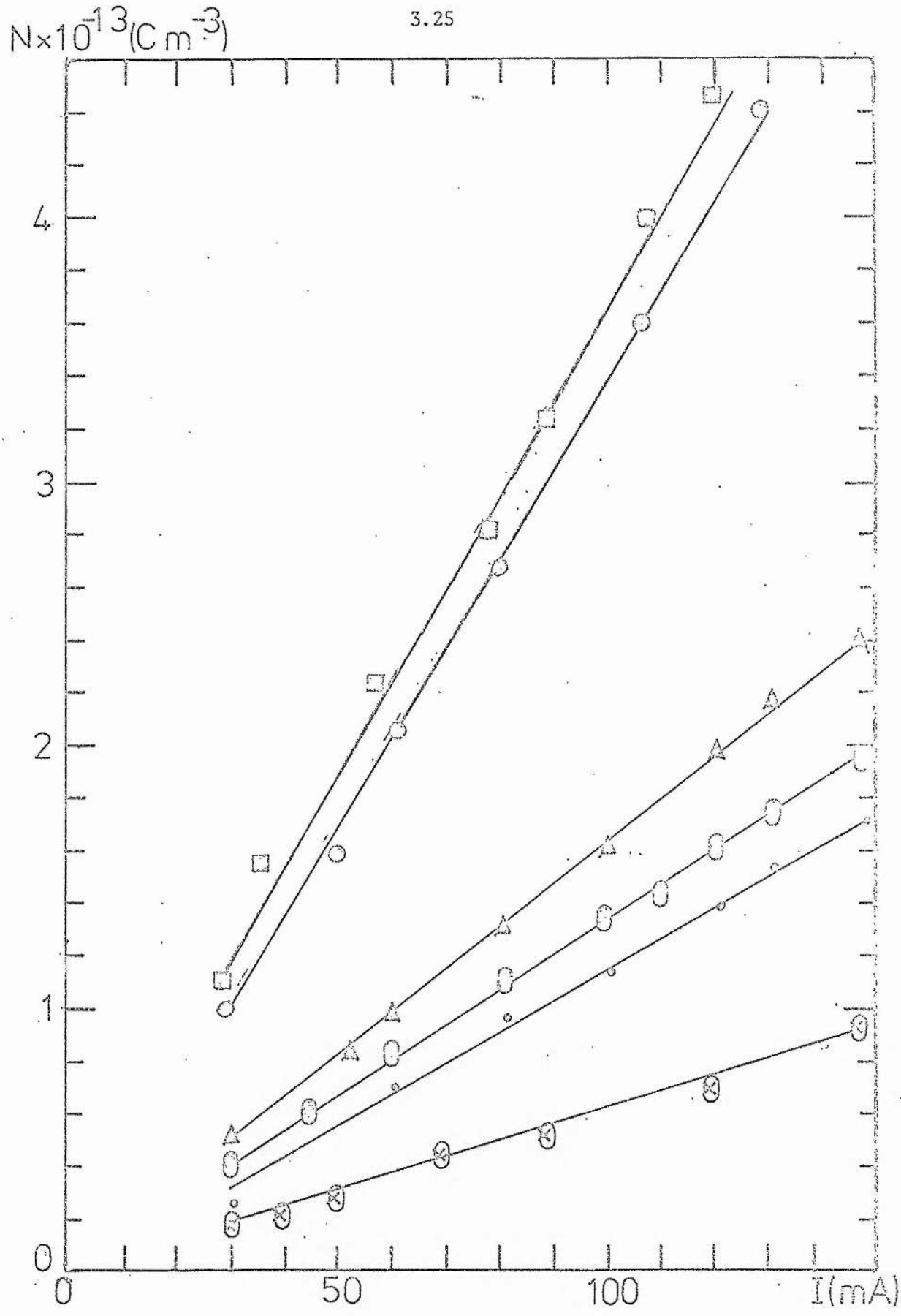

Figure 3.4a. The electron number density measured at the tube centre as a function of the discharge current for different helium filling pressures ○ 1 Torr, ⊗ 2.5 Torr, ⌀ 5 Torr, □ 10 Torr, △ 13 Torr, and ∘ 15 Torr.

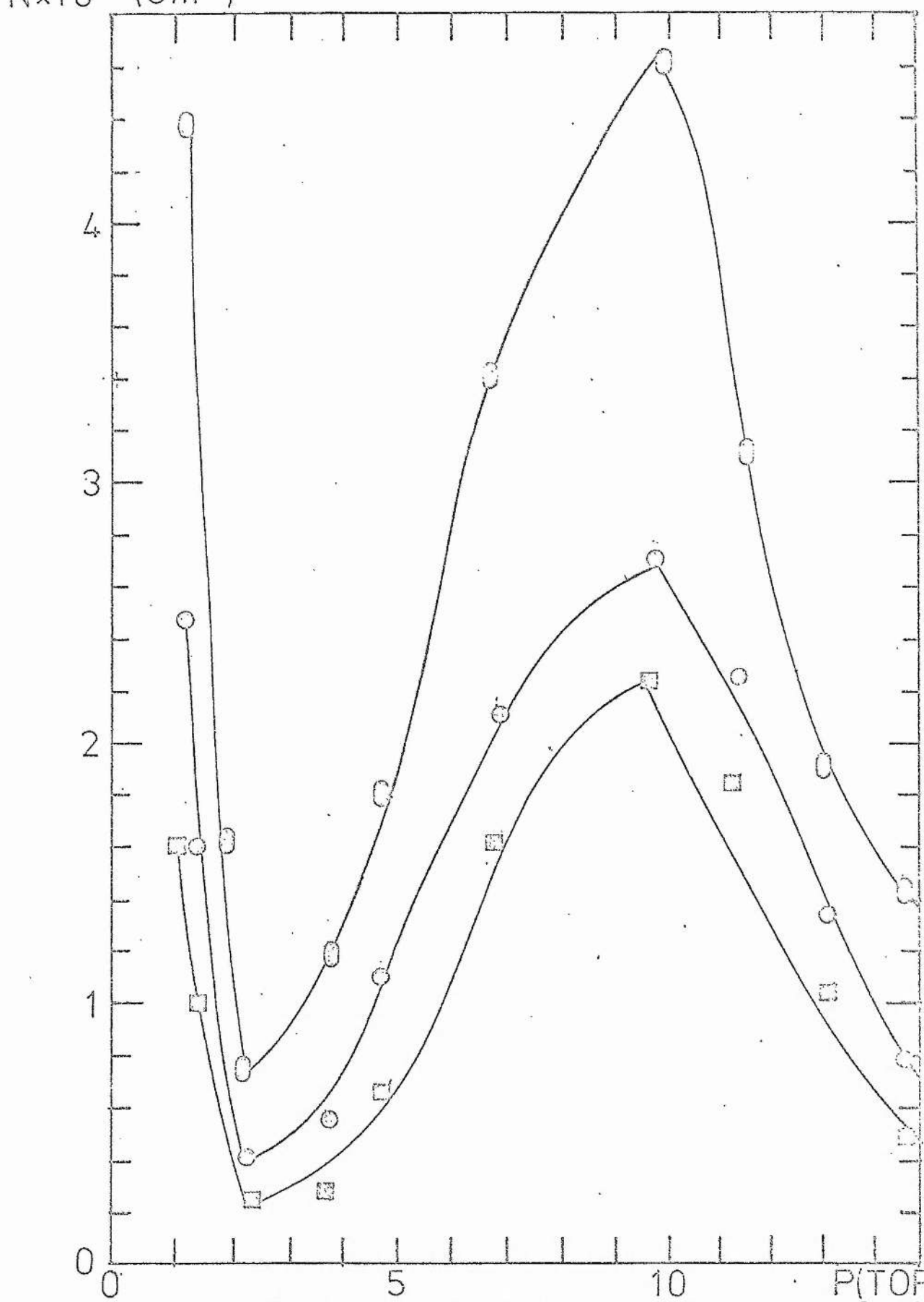

Figure 3.4b. The electron number density at the tube centre as a function of filling helium pressure, for different discharge currents, □ 50 mA, ○ 80 mA and ⬯ 130 mA.

CHAPTER IV

ELECTRON DENSITY MEASUREMENTS USING LASER HETERODYNE TECHNIQUE

4.1 Introduction

In Chapter III electron number densities were measured using line broadening due to the Stark effect. However, it was found that the Doppler width was comparable to the Stark width under the conditions of electron density in the hollow cathode discharge. Hence the method was not particularly sensitive. It was therefore decided to measure the electron number density by an alternative technique using laser heterodyne.

The laser heterodyne technique described in this chapter can be used to measure the spatial variation of electron density as well as electron density at the tube centre. This is useful in understanding the Penning and Duffendack reactions in the hollow cathode (see Chapter VI). Information about the decay and loss mechanisms can also be obtained by comparing the measured electron density and the spontaneous emission.

The technique is to locate the discharge under investigation within the cavity of a laser. The refractive index of the discharge depends on, among other things, the electron density. Hence the presence of electrons within the cavity alters the effective length of the cavity and so shifts the mode frequencies of the laser. This shift can be detected by mixing (Heterodyning) the laser output with that from a reference laser and monitoring the shift in beat frequencies between the two lasers resulting from the presence of electrons. The signal from the reference (passive laser) and the signal from the signal laser (laser with discharge) are mixed by superimposing them on a photodiode or photomultiplier. Typically, the area of mixing is greater than 1000λ (λ is the wavelength) usually around 1 mm^2. Each element of the photodiode gives rise to a small current which must be in phase with other currents to get maximum response. This means that the two lasers must have the same phase relation over the photodiode area.

The heterodyne method is much more sensitive for detecting refractive index changes than interferometric procedures. For example, as will be shown in (§ 4.2), with a typical laser cavity length a beat frequency change of 1MHz (which is easily measurable) is equivalent to shift of 1/300th of a fringe.

Measurement of the electron densities by interferometric methods was studied by Ashby et al[40]. In this technique the discharge cell is located outside the cavity where it modulates the output power of the laser. This modulation is proportional to the species densities which can be measured from the interference fringes. Electron densities in the range of 10^{15} cm^{-3} corresponding to 15 fringes were measured. This technique was improved by Gerardo and Verdeyen[41] and Baker et al[42] who were able to measure electron densities of 10^{14} cm^{-3}. The greatest improvement for interferometric techniques was brought about by Gerardo and Verdeyen[43] who suggested locating the discharge cell inside the laser cavity and hence increasing the technique sensitivity. It was possible to measure electron densities[44-46] in the range of 10^{13} cm^{-3}. In all of the above techniques the interference fringe pattern is measured.

The aforementioned beat frequency shift technique was suggested by Malamud[47] and it was studied experimentally by Verdeyen et al[48]. Due to its high sensitivity this technique is used instead of the interferometric method for low electron density plasmas ie densities[49,50] in the range of 10^{11} cm^{-3} and less (see 4.5).

4.2 Heterodyne techniques as plasma diagnostic methods

The beat frequency obtained on mixing light from two lasers depends on the effective (optical) cavity length of the lasers. If one or other of the optical lengths changes by some means then the beat frequencies shift by an amount which is proportional to that change. The change in the optical cavity length can be brought about by operating a discharge

cell within one of the cavities. Refractive index changes associated with the discharge then change the effective length and hence the beat frequency. By measuring beat frequency shift, refractive index changes can be measured. The refractive index n is related to the gas species by the following relation[51]

$$n - 1 = -\tfrac{1}{2} \left(\frac{\omega_p}{\omega}\right)^2 + 2\pi \sum_a \alpha_a (\omega) N_a + 2\pi \sum_i \alpha_i (\omega) N_i, \qquad (4.2.1)$$

where ω_p is the plasma oscillation angular frequency which depends on the electron density N_e and is equal[46] to $(5.6 \times 10^4 N_e^{\frac{1}{2}})$, ω is the angular frequency of the laser used, N_a is the number density of atoms in the neutral state of polarizability $\alpha_a(\omega)$, and N_i is the number density of ions in the ion state i of polarizability $\alpha_i(\omega)$[52]. The sums are over all atomic and ionic states, respectively. From equation (4.2.1) we can see that measuring the change in the refractive index can be used to measure electron, atom, ion and excited state densities depending on their relative contributions.

The beat technique can be summarized in the following: if we have two cavities with length L_1 and L_2 these cavities oscillate on two frequencies ν_1 and ν_2, when they are mixed they give a beat frequency ν_{sig} equal to[47]

$$\nu_{sig} = \frac{c}{L_1 L_2} (P_1 L_2 - P_2 L_1) \qquad (4.2.2)$$

where P_1, P_2 are integers and c is the velocity of light. When a cell of length t is introduced into the cavity of one of the lasers the optical path of that laser becomes $L_1 + (n - 1)t$, (see figure 4.1) and hence the beat frequency changes by

$$\delta \nu_{sig} = -\frac{c}{\lambda} \left[\frac{t(n - 1)}{L_1 + t(n - 1)}\right] \quad \text{(Hz)} \qquad (4.2.3)$$

Equations (4.2.3) and (4.2.1) show the dependence of the beat shift on the plasma species number densities.

Generally the effect of the excited states and ions is small in comparison to electron and ground state atom effects (see § 4.3). This leaves us with three possibilities.

1. Electron and ground state atoms effects are comparable; in this case to determine both we require beat frequency shifts at two different frequencies ω_1 and ω_2. Equation (4.2.3) is replaced by two equations solvable in N_e and N_a.

2. If we have a low electron density plasma, so that $\omega_p << \omega$ then equation (4.2.3) can be used to deduce neutral atom number densities.

3. If the electron density is high enough and the change in N_a is small equation (4.2.3) can be used to deduce the electron densities.

Generally δn (= n - 1) is very much less than unity and $\frac{t}{L_1}$ is in the range of 0.1. In this situation we can see from equation(4.2.3)that the shift in frequency due to the plasma cell is

$$\delta \nu_{sig} = - \nu \frac{t}{L_1} \delta n \qquad \text{(Hz)} \qquad (4.2.4)$$

In the previous treatment it was assumed that there is only a single longitudinal mode oscillating in each laser. When there are m longitudinal modesoscillating in each laser simultaneously, similar analysis shows that $\delta\nu_{sig}$will be given also by equation (4.2.4). The difference is that we have numerous[53] beat frequencies in this case (see table 4.1).

This technique is more sensitive in plasma diagnostics than interferometric methods. Taking a He-Ne laser at 0.6328 μm, and $\frac{t}{L_1} \simeq 0.1$ with refractive index changes of $\delta n \simeq 10^{-6}$ we can see that the beat shift is around 1 MHz and this is easy to measure. If an interferometric technique was used the corresponding fringe shift would be

$$N = -\frac{\nu}{c} \delta nt = -\frac{L_1}{c} \delta \nu_{sig} \qquad (4.2.5)$$

Taking L_1 equal to 100 cm, $\delta\nu_{sig}$ equal to 1 MHz we find N is $\frac{1}{300}$th of a fringe.

The minimum detectable frequency in the heterodyne technique is limited by the laser stability and the duration of the discharge. These aspects will be discussed in § 4.5.

In practice, the beat frequencies are first monitored in the frequency mode using a spectrum analyser which can detect frequencies in the range of 0.1 - 1500 MHz. The chosen beat is then shifted to low frequencies (< 1 MHz) by piezoceramic tuning elements on the cavities and is then monitored in real time by displaying it on an oscilloscope. In this way the change in beat frequency on a time scale comparable to one cycle of the beat frequency can be monitored.

4.3 Laser heterodyne technique for species measurement in the hollow cathode discharge

We have seen that the change in the refractive index is due to electrons, atoms, ions and excited states. This change is represented by equation (4.2.3). This equation shows the potentiality of the technique for plasma diagnostics where it is evident that electrons, atoms, ions and excited states number densities can be measured.

The technique can be used to measure changes in several number densities simultaneously provided beat shifts are measured on the appropriate number of frequencies (ω_1, ω_2, ...), namely the same number as the number of unknowns. In this case a set of simultaneous equations of the form of (4.2.3) must be used. Alternatively, it may be that a particular species is predominant in affecting the beat shift when the number density of that species can be deduced directly from a single beat shift measurement. The technique can be generalized to measure number densities of impurities (such as air, H, N, in a helium plasma), mixtures (such as He-Ne, He-Ar ...) and additives (such as Cd, Zn, Sr, Na ...), by following similar procedures.

In this present work, the relative contribution of electrons, atoms,

ions and excited states of helium will be presented for discharge conditions appropriate to a He-Cd hollow cathode laser where the helium pressure is 1 to 20 Torr and the discharge current is 10 to 150 mA.

(I) The effect of electrons: This effect depends on the electron number density and the laser wavelength and is represented by $\frac{1}{2}(\omega_p/\omega)^2$ in equation (4.2.1). In table (4.2a), the electron effect on the refractive index for electron densities of 10^{13} and 10^{15} cm^{-3} and for various laser transitions from 0.488 to 10.6 μm is presented. In table (4.2b) the electron effect for electron number densities of 10^{10} to 10^{15} cm^{-3} and laser transitions at 0.6328, 1.15 and 3.39 μm is presented. It is worth noticing that at an electron number density of 10^{13} cm^{-3} the electron effect is 1.77×10^{-9}, at 0.6328 μm, 5.84×10^{-9} at 1.15 μm and 50.7×10^{-9} at 3.39 μm.

(II) The effect of neutral helium atoms: This depends on the polarizability and number density of the helium atoms in the ground state. The polarizability of helium atoms in the ground state was measured by Dalgarno and Kingston[52] and is equal to 2.05×10^{-25} cm^3. This gives a contribution to the refractive index ($2\pi \alpha N_a$) equal to 4.5×10^{-8} for a pressure change of 1 Torr at 300 °K. However the gas density decreases as the neutral gas temperature increases, so the above effect is equal to 2.25×10^{-8} at 600 °K. From here we see that for a pressure change of 1 Torr the atom effect on the refractive index is about an order of magnitude larger than the electron effect at 0.6328 μm due to an electron density of 10^{13} cm^{-3}.

(III) The effect of the ions: The effect of He^+ is proportional to the number density of He^+ and the polarizability of He^+ ion (which is equal[54] to 5.95×10^{-25} cm^3). At a number density of 10^{13} cm^{-3} the

He^+ effect is equal to 5.95×10^{-12}. This is at least two orders of magnitude smaller than the electron effect at an electron number density of 10^{13} cm^{-3} and at the laser transition 0.6328 μm.

Other ions such as He^{++}, H^+ and He_2^+ may be present in the discharge. However the number density of each of the above species is at least an order of magnitude smaller than the number density of He^+ (see § 3.2 and §4.8.2.).Hence their effect on the refractive index change can be neglected.

(IV) The excited states effect: The effect of the excited states of atomic helium can be estimated from the polarizability due to the transitions adjacent to the laser transitions at 0.6328 μm, 1.15 μm and 3.39 μm. This polarizability (α) and hence the excited states effect ($2\pi\ \alpha\ N^*$) (N^* is $N_m(1 - \frac{N_n}{N_m}\ \frac{g_m}{g_n})$, where N_m and N_n are lower and upper levels of the transition and g_m and g_n are their statistical weights) can be written (in the absence of damping, which is small for off resonance transitions) as follows[55]

$$2\pi\ \alpha\ N^* = f_{nm}\ \frac{e^2}{2\pi\ mc^2}\ \ \frac{\lambda_{nm}^2\ \lambda^2}{\lambda^2 - \lambda_{nm}^2}\ \ N^* \qquad (4.3.1)$$

where f_{nm} is the oscillator strength of the transition λ_{nm}, e, m are the electron charge and mass and λ is the wave length referring to the laser transition.

We now require to estimate helium excited state populations in the discharge. The measured value of the (2^3S) metastable density is typically 5×10^{11} cm^{-3} (see Appendix II). Pumping rates to more highly excited states will be smaller because more energetic electrons are required. This, combined with the rapid radiative decay of these states, implies that their number densities are smaller than the metastable number density under comparable discharge conditions. Browne and Dunn[7] have shown experimentally that the populations of excited helium states in the positive column do not exceed 30% of the metastable

populations. In table (4.2c) the effects of the transitions adjacent to the laser transitions at 0.6328 μm, 1.15 μm and 3.39 μm have been estimated assuming N* values of 5×10^{11} cm^{-3}. The maximum contribution to the refractive index is around 35% of that due to an electron density of 10^{13} cm^{-3}. Excited states are therefore unlikely to contribute more than 10% of the refractive index changes even when the lowest electron densities are being measured.

The effect of other excited atoms such as H* (especially from the H_α transition at 0.6563 μm) and H_2^* can be neglected since H* number density is expected to be less than 10^{10} cm^{-3} and also He_2^* number density is at least one order of magnitude smaller than (2^3S) (see § 3.3, table 4.2c and § 4.8.2). Generally we can say that the effect of excited states on the refractive index change is at least two orders of magnitude less than that due to an electron density of 10^{13} cm^{-3}.

(V) The effect of impurities: Impurities such as H and N may be present in the discharge due to desorption from the discharge tube walls. The number density of the atoms resulting from this effect is in the range of 10^{14} cm^{-3}. The effect of say the H atom (its polarizability is 5.93×10^{-25} cm^3) at this pressur does not exceed 10^{-12} which is three orders of magnitude smaller than that of an electron density of 10^{13} cm^{-3} at 0.6328 μm. Similar analysis applies for N atoms Therefore the relative contribution of the impurities under our discharge conditions to the change in the refractive index can be neglected.

The above discussion shows that in the present discharge conditions and for an electron number density of 10^{13} cm^{-3}, the relative contribution of the helium ion number density and the excited state number density to the change in the refractive index is at least one order of magnitude smaller than that of the electron contribution at 0.6328 μm, so their effect can be neglected. The effect of He atoms in the ground state depends on the change in the gas pressure during the actual operation of the discharge, and this effect may be comparable to that of the electrons. Therefore it is necessary to estimate the effect of the atoms experimentally. This will be considered in

(§ 4.5.2) and (§ 4.8.1) by measuring the beat shift at 0.6328 μm and 1.15 μm.

We now consider the theoretical aspects of the laser heterodyne and the required conditions for stable operation.

4.4 The theoretical aspects of laser heterodyning

In the following paragraph the theory of laser heterodyning will be developed. From this theory conditions for optimum signal will be deduced.

4.4.1 The general theory of laser heterodyning

The essence of laser heterodyning is the photomixing of two different modes from two different lasers. Each laser generally oscillates in n longitudinal modes. These modes propagate outside the cavity in the Z direction (along the cavity axis) and each has an electric field amplitude equal to E_n. The total electric field E(z,t) is the superposition of all the individual electric fields of the longitudinal modes.

Assuming that the electric fields are constant over the beam cross-section and ignoring the beam divergence (ie the wave front curvature of the individual electric fields is effectively infinite) the total electric field can be written as[56]

$$\underset{\sim}{E}(z,t) = \sum_n \underset{\sim}{U}_n E_n \sin(K_n z - \omega_n t - \theta_n) \qquad (4.4.1.1)$$

where $\underset{\sim}{U}_n$ is a unit vector defining the polarization of the modes, θ_n is an arbitary phase factor, K_n is defined as the wave number and ω_n is the angular frequency of the mode. Generally the polarization of the modes is defined solely by the orientation of the Brewster windows of the laser tube and this determines the direction of $\underset{\sim}{U}_n$. It is now assumed that both the signal and the reference lasers are polarized in the same way (ie the same $\underset{\sim}{U}_n$). In this case, the field can now be treated as a scalar rather than a vector quantity. Using equation (4.4.1.1) the electric field E_R of the reference laser (Laser 1

in fig 4.1) can hence be written as

$$E_R = \sum_n E_n^R \sin (K_n^R S_R - \omega_n^R t + \theta_n^R) \qquad (4.4.1.2)$$

where S_R is an equivalent optical path length traversed through the air by the reference laser beam.

Assuming that the angular frequency of the signal laser (laser 2 in fig 4.1), differs from the angular frequency of the reference laser by ω_s, then the electric field of the signal laser can be written as

$$E_M = \sum_n E_n^M \sin [K_n^M S_M - (\omega_n^R + \omega_s)t + \theta_n^M] \qquad (4.4.1.3)$$

where S_M is defined similarly to S_R. The total electric field E at the photodetector surface is the sum of the above two electric fields.

The photodetector responds to the intensity of the heterodyning signal averaged over many cycles (ie $\overline{E^2}$). So we can write the current at the photodetector[57] I(t) as

$$I(t) = \frac{e}{h\nu} \iint \eta (x,y) \overline{E^2} \, dA \qquad (4.4.1.4)$$

where η is the quantum efficiency of the photodetector which varies very little over the photodiode surface and is constant for most practical photodiodes and dA is a surface element of the photodiode. The total electric field at the photodiode surface is

$$E^2 = (E_R + E_M)^2 \qquad (4.4.1.5)$$

If we assume that each laser oscillates in one longitudinal mode then the above equation can be written in terms of E_1^R, E_1^M, ω_1^R, ω_s and ω_1^M by substituting equations (4.4.1.2) and (4.4.1.3) in equation (4.4.1.5) to get

$$E^2 = (E_1^M)^2 \sin^2 (K_1^M S_M - (\omega_1^R + \omega_s)t + \theta_1^M) + (E_1^R)^2 \sin^2 (K_1^R - \omega_1^R t + \theta_1^R) + 2 E_1^R E_1^M \sin (K_1^M S_M - (\omega_1^R + \omega_s) t + \theta_1^M) \sin (K_1^R S_R - \omega_1^R t + \theta_1^R) \qquad (4.4.1.6)$$

On averaging over many cycles of the field, the first two terms of equation (4.4.1.6) give a dc signal which is proportional to

$$\tfrac{1}{2}(E_1^M)^2 + \tfrac{1}{2}(E_1^R)^2, \qquad (4.4.1.7)$$

The components at the double frequency being eliminated by the photodetector because of the averaging. The third term of equation (4.4.1.6) gives the sum and difference frequencies. The sum term will be eliminated as above by averaging and hence we will be left with the difference term which is the desired intermediate frequency where its power is proportional to

$$E_1^R E_1^M \cos [K_1^M S_M - K_1^R S_R) + \omega_s t + (\theta_1^M - \theta_1^R)] \qquad (4.4.1.8)$$

If we assume the power of the reference laser is P_R, the power of the signal laser is P_S and the power of the background radiation is P_B, then the generated dc and intermediate frequency currents are

$$< I_{dc} > = (\frac{ne}{h\nu}) (P_R + P_S + P_B), \qquad (A) \qquad (4.4.1.9a)$$

and

$$< (I_F)^2 > = 2 \alpha^2 P_S P_R = 2(\frac{ne}{h\nu})^2 P_S P_R \ (A) \qquad (4.4.1.9b)$$

respectively. On the latter average we have assumed that the terms $(K_1^M S_M - K_1^R S_R)$ and $(\theta_1^M - \theta_1^R)$ do not change in value in moving across the detectors surface. The conditions necessary for this to be the case are discussed in (§ 4.4.2).

The shot noise accompanying the direct current[58,59] is given by

$$< (I_{noise})^2 > = \frac{2\eta e^2 b}{h\nu} (P_R + P_S + P_B) \ (A) \qquad (4.4.1.10)$$

where b is the bandwidth of the photodetector. From here we can see that the dc current determines the S/N ratio according to

$$(\frac{S}{N}) = \frac{<(I_F)^2>}{<(I_{noise})^2>} = \frac{P_R P_S \eta}{(P_R + P_S + P_B) bh\nu} \qquad (4.4.1.11)$$

The bandwidth of the photodiode limits the beat frequencies to those of low frequencies ($\sim$ few MHz). If we consider the case where the bandwidth of the photodetector is of the order of 10 MHz and reference signal beam powers are around 1 mW, then the signal to noise ratio

given by (4.4.1.11) is about 10^7.

4.4.2 Conditions for optimum laser heterodyne signal

There are two basic requirements for optimum beat signal which can be concluded from the general theory.

Firstly, the signal to noise ratio (S/N) must not be degraded by redundant dc signals from the photodiode. This means that the interfering beams from the two lasers must overlap as closely as possible and be of equal intensity. Radiation outside the overlapping region leads only to dc signals (with its accompanying noise) and no beat signal. Hence the two beams must have the same spot size on the photodetector. Also it is preferable that the beams are in single transverse modes (and preferably TEM_{00q} for ease of alignment) since the different transverse modes are generally not frequency degenerate and hence a mixture of modes could contribute a range of beat signals.

The second requirement is that phase match between the interfering beams is preserved across the photodetector. This ensures that the beat signals from different parts of the detector are in phase and add together constructively. The requirement for phase match are:

1. Co-linearity of the beams
2. Equal radius of curvature of the beams.

The limit on these requirements for good phase match is discussed in (§ 4.6.4). Obviously alignment and stability are important in this context and this will be discussed in (§ 4.5 and 4.6).

4.5 Factors affecting the stability of a laser

Fluctuations in the frequencies of the individual lasers lead to fluctuations in the beat frequency when the two are mixed. We therefore require to consider processes giving rise to fluctuations in the individual lasers.

A laser operating in ideal environmental conditions will be affected

by fluctuation created by the random walk of the laser phase due to the spontaneous emission or the quantum noise. This factor puts an upper limit on the frequency stability, which can be found from the relation[60]

$$\Delta \nu_1' = \frac{\pi h \nu}{p} (\Delta \nu_{cavity})^2 \quad \text{(Hz)} \qquad (4.5.1)$$

where h is Planck's constant, ν is the laser frequency, p the laser output power and $\Delta \nu_{cavity}$ is the width of the cavity oscillation. Taking the He-Ne laser transition 0.6328 μm, which has a laser output power of a few mw in a cavity of 70 cm, we find that the upper limit of the laser stability is less than a mHz.

However there is another factor which affects the stability of the laser, namely the Brownian motion of the cavity mounts. Taking a cavity mount of height (h_1) and a cross-section (a), then the potential energy involved in the Brownian motion creates a change in the laser cavity length ΔL, which results in a change $\Delta \nu_2'$ in the laser frequency given by

$$\Delta \nu_2' = \nu \left[\frac{k T h_1}{a L^2 Y}\right]^{\frac{1}{2}} \quad \text{(Hz)} \qquad (4.5.2)$$

where Y is Young's modulus, which assumes a value of 7×10^{11} g cm^{-2}. For (L) of 70 cm, (a) of 100 cm^2, and an aluminium mount height (h_1) of 10 cm we find $\Delta \nu_2'$ is about 0.1 Hz or $\frac{\Delta \nu_2'}{\nu}$ is about 10^{-15} at 0.6328 μm. This value represents the ultimate achievable He-Ne laser stability in ideal conditions. However, in normal laboratory conditions due to environment, heat, pressure, humidity, draught, etc, we do not expect to achieve this stability. We now consider these factors explicitly.

They are contributed by the laser cavity, the laser tubes, the studied discharge and the remaining space in the two cavities. If we consider the lasers operating in the TEM_{00q} modes, then the cavity resonant frequency ν_q for each laser can be written as

$$\nu_q = q \frac{C}{2nL} \quad \text{(Hz)} \qquad (4.5.3)$$

where q is an integer which assumes a large value, n is the refractive index of the medium and L is the cavity length. The optical path nL (in laser 2 in figure 4.1) can be written as follows

$$nL = \ell_1 n_D + n_t t + n_a (L - \ell_1 - t) \quad \text{(cm)} \qquad (4.5.4)$$

where ℓ_1, t, $(L - \ell_1 - t)$ are the discharge laser, the plasma discharge and the remaining space lengths and n_D, n_t and n_a are their respective refractive indices respectively. Since we will be studying the changes in n_t, then changes in all other parts of equation (4.5.4) need to be eliminated. In this paragraph factors affecting the changes in ℓ_1, n_D, n_a and $(L - \ell_1 - t)$ will be presented. The magnitude of these changes and hence the changes in the beat frequency when the output from two similar lasers are mixed will be considered for two He-Ne lasers each operating at 0.6328 μm and 1.15 μm and oscillating in two separate cavities which have mirror separations of 42 cm and 72 cm respectively. They will be compared with the expected change in the beat frequency due to the electron number density which was considered in (§ 4.3).

The laser frequency ν_q at 0.6328 μm is 4.47×10^{14} Hz while it is 2.61×10^{14} Hz at 1.15 μm. Since we expect the beat shift to be in the range of 10^5 - 10^6 Hz (see § 4.8.2) then the experiment should be sensitive enough to measure changes in the resonant frequency equivalent to a $(\Delta \nu_q/\nu_q)$ ratio of about 10^{-9}. Since $\Delta \nu_q/\nu_q$ is equal to $\frac{\Delta L}{L}$ then we should be able to measure change in the cavity length L equivalent to 4.2 Å at least.

4.5.1 Factors contributed by the lasers and their cavities

(I) Internal factors: We have seen in (§ 4.2 and § 4.3) that changes in the number density of electrons, atoms, ions and excited states lead to changes in the refractive index and hence to change in the optical path. These changes can occur in the laser discharge itself. Since the

laser is a sealed off laser, then changes in the neutral density are negligible. The changes in electrons, ions and excited state densities depend on the changes in the discharge current. Assuming this is stabilized to be better than 1% and that the He-Ne discharge has an electron density of 10^{12} cm^{-3}, then ΔN_e is 10^{10} cm^{-3}, which gives a frequency shift less than 1 K Hz (see § 4.2 and table 4.3a). Consequently $\frac{\Delta\nu_q}{\nu_q}$ is in the range of 5×10^{-12}. From here we can see that the effect of the electron density fluctuation in the laser medium is negligible.

Similarly because of their small polarizabilities the effects of ions and excited states can be ignored. Generally the aforementioned effect is negligible, but it puts an upper limit on the stability of a laser.

(II) External factors:

i) Atmospheric effects such as temperature, pressure and humidity. These changes, especially the temperature which may change rapidly with time due to the heat dissipation of the lasers and the discharge, lead to beat drift and instability. However measurements of the room temperature and pressure for four hours by a thermometer and a barometer showed that the temperature changes by $0.2^{o}C$ per hour or 5.5×10^{-5} degree per second while the pressure changes by 0.1 Torr per hour or 2.8×10^{-4} Torr/sec.

The change $\frac{\Delta\nu_q}{\nu_q}$ due to changes ΔT and ΔP in the atmospheric temperature and pressure respectively is given by[61]

$$\left(\frac{\Delta \nu_q}{\nu_q}\right)_T = \rho\ \beta_T\ \Delta T,\ \beta_T = 9.3 \times 10^{-7}/^{o}C, \qquad (4.5.1.1)$$

$$\left(\frac{\Delta \nu_q}{\nu_q}\right)_P = \rho\ \beta_P\ \Delta P,\ \beta_P = -3.6 \times 10^{-7}/\text{Torr} \qquad (4.5.1.2)$$

where ρ is the fraction of the cavity length open to the air. In the present system the open parts of the laser cavities do not exceed 10 cm in each cavity which gives a maximum value of ρ equal to 0.24. Taking the measured values of ΔT (5.5×10^{-5} ^{o}C sec^{-1}) and ΔP (2.8×10^{-4} Torr sec^{-1}) we find that $(\frac{\Delta \nu_q}{\nu_q})_T$ is 1.2×10^{-10} sec^{-1} and $(\frac{\Delta \nu_q}{\nu_q})_p$ is $- 2.4 \times 10^{-10}$ sec^{-1}.

The rise in temperature also leads to expansion of the granite block (see § 4.7). The resulting shift in beat frequency is given by.

$$\frac{\Delta \nu_q}{\nu_q} = \frac{\Delta L}{L} = \beta \Delta T \qquad (4.5.1.3)$$

If we take β equal to 10^{-6} $(^{o}C)^{-1}$ and underline a rate of $5.5 \times 10^{-5}{}^{o}C$ sec^{-1} in the temperature we find that $\frac{\Delta \nu_q}{\nu_q}$ is about 5.5×10^{-11} sec^{-1}. A comparable expansion effect also occurs in the mirror mounts. From here we can see that in a steady state case these effects may become a serious problem since temperature and pressure changes are expected to increase as the time increases.

(ii) Vibrations effects: Vibrations can be communicated to the apparatus through the mounting arrangement or through the air. The precautions taken to minimize the former by a suitably designed anti-vibration mounting are described in (§ 4.7). In a typical laboratory environment the residual jitter due to airborne vibrations was of the order of 0.1 MHz in the frequency range 300 - 1200 Hz (see table 4.3b).

(iii) Change in the optical path: Rotation of the Brewster angle windows within the cavity alters the effective optical path length of the cavity. Assuming that the incident angle on a Brewster window of thickness (b) and refractive index n is θ and the refraction angle is θ', then the net contribution of the window to the optical path is

$$S = \frac{b}{\cos \theta'} \left[n - \cos(\theta - \theta') \right] \qquad (4.5.1.4)$$

A change in this contribution creates a shift in the beat frequency $\Delta\nu_q$, which can be written for the case of $(\theta + \theta')$ equal $\frac{\pi}{2}$ and for $\theta = \theta_B$ (Brewster angle θ_B orientation) as

$$\frac{\Delta\nu_q}{\nu_q} = \frac{\Delta S}{L} = \frac{nb\delta\theta_B}{L} \quad \frac{\sin\theta_B\,[n - 2(\sin\theta_B)(1 - \sin^2\theta_B)^{\frac{1}{2}}]}{(n^2 - \sin^2\theta_B)^{3/2}} \qquad (4.5.1.5)$$

For (b) of 3 mm, $\delta\theta_B$ of 10^{-6} rad sec^{-1}, $\frac{\Delta\nu_q}{\nu_q}$ is 2.21×10^{-9} and 3.79×10^{-9} s^{-1}.

The above analysis suggests that this effect can be important in a steady state situation, where the Brewster windows may rotate due to the heat dissipation in the system.

(iv) The effect of air current: The open parts of the cavities suffer from exposure to draught due to the air turbulence in normal labatory conditions. This draught causes the beat frequency to jitter by about 0.1 MHz. Hence in the present system all the open parts are fitted with sliding nylon bushes which prevent the draught. (see figure 4.1 and § 4.7). These fittings proved to be successful, reducing the drift to less than 5KHz sec^{-1} (see tables 4.3a,b).

4.5.2 Factors contributed by the studied discharge

Basically the hollow cathode discharge tube is affected by the same mechanical and acoustical effects which affect the lasers. However there are other effects associated with the hollow cathode. These are the filling gas pressure changes and the effect of cooling the discharge tube. The drift in the beat frequency due to the above two effects was measured separately and will be described in the following.

I] The effect of the pressure change: In this case there is no discharge, hence equation (4.2.5) can be written as

$$\delta\nu_{sig} = -\frac{c}{\lambda}\,\frac{1}{(L_1/2\pi\,\alpha\,\tau\,N_a) + 1} \qquad (4.5.2.1)$$

This equation gives in a discharge length of 20 cm, 6.3 MHz/Torr for He,[52] 49 MHz/Torr for Ar[53] and 51 MHz/Torr for N_2[62]. The experimental values for He, Ar and N_2 were found to be 6 MHz/Torr, 50 MHz/Torr and 50 MHz/Torr respectively (see figure 4.2).

By measuring beat frequency shifts at two different wavelengths (0.6328 and 1.15 μ) the relative contributions of pressure and electron density changes can be estimated. This is discussed fully in (§ 4.8.1).

II.] The effect of cooling of the discharge tube: The influence of temperature changes associated with the discharge tube itself was estimated by heating the tube up with an external heater while pumping on the tube to keep the gas pressure low (< 1 m Torr). On switching off the heater a drift of about 1.5 KHz s^{-1} was observed. This is too large to be due to a number density change in the residual gas with cooling, and represents the influence of anisotropic changes in tube dimensions, with cooling which probably result in window rotation (§ 4.5.1 (iii)).

4.6 The study of the laser heterodyne in a decaying plasma

The expected drifts in beat frequency due to environmental effects and the cooling of the discharge tube after switch-off of the discharge are summarized in table (4.3a). For these not to exceed the shift due to an electron density of 10^{13} cm^{-3}, the measurement time must be less than 1 sec. Hence the discharge must be switched on/off in a time less than this. Jitter of the beat frequency also occurs for a variety of causes, these are summarized in table (4.3b). Again if shifts are to be measured without recourse to averaging to eliminate jitter, the measurement time must not exceed 1 sec.

In order to achieve a rapid switching of the discharge a crowbar system incorporating a thyratron was used. This is described in (§ 4.7.3). After crowbarring the current was found to decay over a time interval of 200 μ sec, being followed by the electron density. Over this time interval drifts and jitters due to the various causes are all individually less than 10^{-12} (table 4.3c), nearly three orders of magnitude smaller than the minimum shift due to the electrons.

Once the various drifts and jitters have been eliminated by rapid switching, there are two remaining effects that influence the beat shift during the decay of the plasma, namely the change in electron density, which it is required to determine, and changes in the ground state atom density resulting from pressure changes. The two effects can be separated experimentally by carrying out measurements at two wavelengths (0.6328 and 1.15 μm). Here we consider the likely magnitude of the latter effect.

The gas temperature and pressure changes, which may produce gas number density changes during the decay time of 200 μ sec, are now considered.

If we assume that the power dissipation after switching the discharge off is equal to the initial power input and that this power input is transferred to the gas atoms by elastic collisions (kinetic energy) then this energy leads to a change in the gas temperature ΔT given by the relation

$$VI\tau = {}^{3}/_{2}\, k\, N_a' \Delta T \qquad (4.6.1)$$

where V is the cathode fall potential, I the discharge current, τ the decay time, k is Boltzmann constant and N_a' is the total number of atoms initially supplied with the electrical energy.

For a plasma with I = 150 mA, V = 200 V and τ = 200 μ sec and of 0.3 cm radius and 10 cm long, ΔT is equal to 4.8×10^3 °K.

Since the initial gas temperature is about 600 ^{o}K (see Chapter II) and the final gas temperature cannot be less than the room temperature which is 300 ^{o}K, then we can see that the assumption of total energy transfer to helium atoms leads to an over estimate of ΔT by about one order of magnitude. Nevertheless the above value of ΔT indicates that the temperature change is significant. This change in the gas temperature (cooling in this case) takes less than 15 μ sec to occur at a pressure of 1 Torr assuming that the cooling happens via diffusion of the ground state atoms to the wall (see equation 3.3.6).

Hence we can see that during 200 μ s a significant gas temperature and accompanying pressure change may occur at the beginning of the decay. These in themselves will not lead to a number density change. However, if the flow of the gas can readjust the gas pressure on the time scale involved, the number density will change. The temperature and pressure change during the decay results in a gas number density change only if the pumping time t of the gas is short compared to the decay time.

The pumping time can be estimated by treating the discharge as a volume (V) connected via the pumping line to a pump of speed S_o. The time required to change the pressure in the volume from P_1 to P_2 is given by[63]

$$t = 2.3 \frac{V}{S_1} \log \left(\frac{P_1}{P_2}\right), \qquad (4.6.2)$$

where S_1 is the pumping speed of the system. This is given by

$$1/S_1 = 1/S_o + W, \qquad (4.6.3)$$

where W is the resistance of the connecting pipe. For the case of a pipe diameter comparable to a mean free path we have[64]

$$1/W = 2.36 \left(\frac{a'^3}{\ell}\right) \qquad (4.6.4)$$

where a' and ℓ are the tube radius and length respectively measured in mm, and W is in sec/litres. Although in the present case the mean free path is less than the tube diameter, equation (4.6.4) will suffice to enable an order of magnitude estimate to be made.

Taking a pipe of 5 mm radius and 120 cm long and a rotary pump of pumping speed 2 litre sec^{-1} (Leybold) we find that S_1 is about 0.2 litre sec^{-1}. This means that the time taken to pump the discharge tube (3 mm radius, 10 cm long) from 1.01 Torr to 1.00 Torr (ie a pressure change of 10 m Torr) is about 130 μ s. This time is more than one half of the decay time. A pressure change of 10 m Torr changes the beat frequency by about 60 KHz at 0.6328 μm, and this shift is about half the minimum expected beat shift (due to an electron density of 10^{13} cm^{-3}). Pressure changes could therefore become important at the lower densities. Beat shifts were measured at both 0.6328 and 1.15 μm so that the relative contribution of electrons and gas atoms could be estimated.

The above study showed that laser heterodyne can be used for plasma diagnostic measurements without the need of servo electronic stabilization. However, precautions must be taken to ensure that beat frequency drift and jitter are negligible during the plasma decay time. The precautions taken to ensure this will be described in the following section.

4.7 Description of experimental arrangement

We now consider the design of the experiment. In particular we are concerned with the construction of an anti-vibration mounting (§ 4.7.1) the laser system (§ 4.7.2), the discharge cell (§ 4.7.3), wave front matching for optimum heterodyne signal (§ 4.7.4) and the signal detection system (§ 4.7.5).

4.7.1 The anti-vibration mount

Four concrete pillars (9" x 9" x 36") were fixed to the floor by bolts and adhesive compound. On top of each pillar sits a pneumatic tyre (air mount insulator No 16, made by Firestone). These tyres are very effective in absorbing the high frequency vibration (frequencies higher than 25 Hz). At low frequencies they absorb 97% of the vibration for vibration frequency of 25 Hz while this decreases to about 50% at vibration frequency of 7 Hz.

A trough of steel is mounted on top of the rubber tyres. The steel trough was filled with dry fresh-water sand which has a very small thermal conductivity. In the central part of the steel trough a block of granite (4" x 15" x 46") was laid down so that its four corners were located over the concrete pillars (see figure 4.3). The granite was chosen because of its small thermal conductivity and its large mass (800 lb) so that the thermal and mechanical vibrations of the granite block are small.

This set-up proved to be very effective, vibrations being reduced at least by two orders of magnitude over the range 0.16 - 16 KHz. A stable beat frequency achieved with this arrangement can be seen in figure (4.4).

4.7.2 The set-up of the laser system

Two laser tubes (Scientifica and Cooke SL-H/3T and SL-H/5T) operating at both 0.6328 μm and 1.15 μm with output powers of 3 and 5 mw respectively were used. These lasers were mounted in Sandanio holders, fixed to aluminium blocks which provided good bedding onto the granite block.

The cavity mirrors were mounted on the piezoceramic cylinders to allow cavity tuning over a range of about 0 to 100 MHz.

The open spaces in the cavities were screened by sliding nylon bushes to prevent the acoustic vibration and draught. This arrangement proved to be very useful in reducing the acoustic noise. In fact experimental observation showed that applying 70 db from a calibrated loudspeaker causes air borne jitter of 0.1 Mhz. Under the normal laboratory conditions we have seen that the jitter is reduced to about 5 kHz.

The photomixing of the two lasers was achieved by combining the light of the local and the signal oscillators. The light from the local oscillator reflected by an adjustable mirror M and then combined with the other beam at an adjustable beam splitter BM. The two beams are mixed at the photo-diode D. The resulting beat frequency was displayed on a spectrum analyser. Full details of the detection system will be described in (§ 4.7.5).

4.7.3 The hollow cathode discharge

The hollow cathode discharge cell is basically similar to that used in the previous chapters (see Chapter I and Appendix I). However, minor adjustments in the length and discharge circuit were necessary, to fit it in the cavity of the laser (laser 2 in figure 4.1). The discharge was fixed onto a horizontal slide so it could be moved readily across the laser beam.

A thyratron was used to crowbar the discharge. The circuit diagram is given in Appendix I (figure A.1.1b). The plasma decay is about 200 μ sec (see figure 4.5).

4.7.4 The optical arrangement for optimum heterodyne signal

In this paragraph the conditions mentioned in (§ 4.4.2) will be discussed in detail. The conditions for wave curvature, spot size and intensity matches will be considered. This study will follow Maitland and Dunn[55] for a description of the Gaussian beam.

A Gaussian beam is characterized by the location Z_A and diameter W_o of its beam waist. The beam waist diameter W_o is given in terms of the radius of curvatures R_A and R_B of the cavity mirrors and their separation d by the relation

$$W_o^4 = \left(\frac{2}{K}\right)^2 \frac{d(R_A - d)(R_B - d)(R_A + R_B - d)}{(R_A + R_B - 2d)^2} \qquad (4.7.4.1)$$

The distance of the waist from the cavity mirror of radius of curvature R_A, Z_A is

$$Z_A = \frac{d(R_B - d)}{R_A + R_B - 2d}. \qquad (4.7.4.2)$$

Values of W_o and Z_A for the two laser cavities are tabulated in table (4.4).

The cavity mirrors have plane rear faces, and hence act as lenses to the Gaussian beams propagating through them. This transforms the size and position of the beam waists as seen from outside the cavity. Using the lens makers formula the effective focal lengths of the output coupling mirrors A_1 and B_1 (see figure 4.1) were calculated as $f_{A_1} = -200$ cm and $f_{A_2} = -400$ cm respectively.

The width and radius of curvature of a beam at the detector can be calculated using the complex beam parameter. After transformation by the lens effect of the mirror (focal length f_A) and propagation through free space from cavity to detector, the radius of curvature (R) and beam width (W) are respectively

$$R = \frac{k^2 W_o^4 (Z/f_A - 1)^2 + 4(Z + Z_A - Z Z_A/f_A)^2}{k^2 W_o^4 (Z/f_A - 1)/f_A + 4(1 - Z_A/f_A)(Z + Z_A - Z Z_A/f_A)} \qquad (4.7.4.3)$$

$$W^2 = W_o^2 \left[(Z/f_A - 1)^2 + (4/k^2 W_o^4)(Z + Z_A - Z Z_A/f_A)^2 \right] \qquad (4.7.4.4)$$

where Z_1 is the distance from output coupling mirror to detector and $|Z_A|$ and W_o are given by equations (4.7.4.1) and (4.7.4.2) respectively.

A cartesian sign convention relative to the output coupling mirror has been adopted.

Values of R and W for laser (1) (where Z = 65 cm) and laser (2) (where Z = 23 cm) are tabulated in table (4.4). The magnitude of the beat frequency depends on the coherence distance between the two wave fronts. If we call the wave front curvatures for laser (1) and laser (2) at the photo-diode R_1 and R_2 respectively then the coherence distance x across the photo-diode (ie distance over which a phase match is preserved) can be calculated from figure (4.6b) and is given by

$$x = \left(\frac{2 R_1 R_2 \lambda}{R_1 - R_2}\right)^{\frac{1}{2}}. \qquad (4.7.4.5)$$

For the present case the above relation gives a minimum coherence distance of 1.75 mm, which is comparable to the photo-diode dimensions (see table 4.4).

Although the beam curvatures are in the ratio 3:2 (see table 4.4) the above shows that they are closely enough matched to give an adequate coherence length at the detector. However, the beam diameters are also in roughly the same ratio, and this leads to a reduction in the signal to noise ratio. Hence, it is preferable to try to obtain complete matching of wave curvatures and beam diameters at the photodetector.

This was accomplished by inserting two lenses (L_1 and L_2) of focal lengths f_1 and f_2 respectively into one of the beams as shown in figures (4.3) and (4.6a). If the beam diameters at the photodetector with this new arrangement are W_{D_1} and W_{D_2} and the wave front curvatures are R_{D_1} and R_{D_2} respectively, then the wave match condition is

$$W_{D_1} = W_{D_2}$$
$$R_{D_1} = R_{D_2} \qquad (4.7.4.6)$$

These conditions can be found by using the complex beam parameter as indicated previously. The solution of equation (4.7.4.6) depends on $\gamma (=Z_{21}/Z_{31})$, $\alpha (= f_1/f_2)$ and the distance between the two focal points δ (see figure 4.6). For each value of γ there are values for α and δ which define the appropriate lens system for beam matching. In the present case γ is 5, α is 1.5, hence from equation (4.7.4.6) we find a value for δ of 1.15 cm at 0.6328 μm and 2.2 cm at 1.15 μm(see table 4.4).

The above arrangement has many degrees of freedom enabling complete co-linearity between the two laser beams to be achieved. Co-linearity is a necessary condition for a good beat signal. This can be shown as follows: We assume the two laser beams are being mixed at the surface of a photo-diode such that they are inclined at an angle of θ to one another. The optical path difference as a function of position y on the photo-diode, where y is measured in the plane containing the two beams, is $\frac{2\pi y}{\lambda} \sin \theta$. This optical path difference makes the beat frequency change across the photodiode according to the relation (see § 4.4.1).

$$\cos \left[\omega_s t + \frac{2\pi y}{\lambda} \sin \theta \right], \qquad (4.7.4.7)$$

The phase depends on y and hence changes with position across the photo-diode. These variations are equivalent to interference fringes being formed. If there is more than one fringe across the photo-diode, the average beat signal will tend to zero. This effect was observed when two He-Ne lasers were arranged in such a way that a 10° angle existed between their respective beams. It was impossible to detect a beat frequency with this arrangement because of the above mentioned effect.

The minimum allowable angle θ_1 between the two lasers for the appearance of a beat signal can be calculated by putting

$$\frac{2\pi y}{\lambda} \sin \theta_1 \leq 2\pi \qquad (4.7.4.8).$$

For a value of 1.75 mm, we can find that θ_1 must be less than 2.4×10^{-2}

and 4.4×10^{-2} for 0.6328 and 1.15 μm respectively.

The beam intensity matching can be achieved by using a beam splitter which has an appropriate reflectivity coefficient which can adjust the intensity mismatch of the lasers.

From the above we can see that this optical arrangement allows a complete match between the spot sizes, the wave curvatures and the beam intensities, and enables the beams to be brought into co-linearity.

4.7.5 The detection system

The chosen beat frequency was detected by a photodiode (silicon for 0.6328 μm and Ge for 1.15 μm) of bandwidth 10 MHz and gain of 100. This beat was displayed on the spectrum analyser.

Tuning of the cavities by the piezoceramic cylinders brings the beat frequency towards low frequencies so it can be displayed in real time on an oscilloscope (see figure 4.7). A pulse generator triggers the scope and the discharge with an adjustable delay time between them. This allows the beat frequency before and after the plasma decay to be displayed and hence the beat shift can be measured directly. The resulting beat signal was stored in a storage memory for later display on another scope or on a chart recorder (figure 4.8).

4.8 The experimental results

Electron number densities measured by the above discussed technique will be presented. Before these are considered the effect of ground state helium atoms will be deduced from the beat shift measurements at 0.6328 and 1.15 μm.

The electron number density measured at the tube centre can be compared with that measured using the Stark broadening technique. Besides these measurements, electron number density as a function of the plasma decay time will also be presented. This study will offer an insight into the electron loss mechanisms in the discharge.

The species densities were measured from the measured beat shifts. This was achieved by comparing the beat shift before the decay of the plasma and measuring how the beat frequency changes as a function of time. Effectively we are following the electron decay with time in the plasma.

4.8.1 Estimation of the ground state atoms effect on the beat shift

As we have calculated in (§ 4.3) and demonstrated experimentally in (§ 4.5.2) a change in the helium pressure of 1 Torr causes a beat shift of 6 MHz at 0.6328 μm. This is about one order of magnitude larger than that expected due to an electron number density of 10^{13} cm^{-3}, which is the minimum we require for detection.

In the decaying plasma of interest here we have seen in (§ 4.6) that the change in the helium pressure is expected to be far less than 1 Torr and hence the beat shift due to ground state atoms is expected to be less than that due to 10^{13} cm^{-3} electron at 0.6328 μm. However by comparing the beat shift on two transitions (0.6328 and 1.15 μm) where the relative beat shifts due to both effects are different, it is possible to deduce both the electron density and ground state helium density.

The beat shift on two transitions ω_1 or ν_1 (at 0.6328 μm) and ω_2 or ν_2 (at 1.15 μm) can be written respectively.

$$\delta \nu_{sig_1} = \nu_1 \frac{4\pi\alpha_a \Delta N_a - (\omega_p/\omega_1)^2}{(2L_1/t) + [\,4\pi\alpha_a \Delta N_a - (\omega_p/\omega_1)^2\,]} \qquad (4.8.1.1)$$

$$\delta \nu_{sig_2} = \nu_2 \frac{4\pi\alpha_a \Delta N_a - (\omega_p/\omega_2)^2}{(2L_1/t) + [\,4\pi\alpha_a \Delta N_a - (\omega_p/\omega_2)^2\,]} \qquad (4.8.1.2)$$

where ΔN_a and ΔN_e (implicit in ω_p) are the change in the atom and electron number densities respectively. The polarizability of He changes by less than 1% in going from 0.6328 to 1.15 μm[52] and so the same value has been used in both equations (4.8.1.1) and (4.8.1.2).

Evaluating the parameters in equations (4.8.1.1) and (4.8.1.2) taking ratios we obtain

$$\frac{\delta \nu_{sig_1}}{\delta \nu_{sig_2}} = \frac{\nu_1}{\nu_2} \frac{0.0129\ \Delta N_a - 1.76\ \Delta N_e}{0.0129\ \Delta N_a - 5.83\ \Delta N_e} \qquad (4.8.1.3)$$

This equation shows that for $\Delta N_a = 0$, $(\delta \nu_{sig_1}/\Delta \nu_{sig_2}) = 0.55$, while for $\Delta N_e = 0$, $(\delta \nu_{sig_1}/\delta \nu_{sig_2}) = 1.82$.

Assuming that $(\delta \nu_{sig_1}/\delta \nu_{sig_2})$ is Δ and with some algebraic operations we get

$$\frac{\Delta N_a}{\Delta N_e} = 452.62 \times \frac{0.55 - \Delta}{1.82 - \Delta} \qquad (4.8.1.4)$$

From equation (4.8.1.4) we can see that the ratio of atom to electron number density change can be estimated by measuring Δ, and hence the ratio of atoms to electrons effects at 0.6328 μm are estimated (see table 4.5a).

The measurement of Δ was performed by comparing the beat shift at 0.6328 μm and 1.15 μm under similar discharge conditions. For helium pressure of 1 to 20 Torr and current of 10 to 150 mA, Δ varies between 0.50 and 0.54 (see table 4.5b). Comparing the values of Δ in table (4.5a,b) we find that the atom effect does not exceed 12% of the electron effect at 0.6328 μm. Hence we can take the beat shift at 0.6328 μm to be as a result of the electron effect only.

At early decay time the minimum measured beat shift is about 200 KHz. This suggests that the atom effect does not exceed 24 KHz which is equivalent to a gas number density change of 4 m Torr (see § 4.5.2).

The fact that the beat shift depends predominantly on the electron number density was demonstrated again by comparing the decay of the discharge current with that of the deduced electron number density (see next paragraph). The decay of the electron number density follows that of the discharge current. There is no evidence of an atom effect, which

would lead to the beat shift increasing as the current decays.

4.8.2 The electron number density

Neglecting the ground state atom effect, which does not exceed 12% of the beat shift at 0.6328 μm, the electron number density N_e is related to the measured beat shift $\delta \nu_{sig}$ by equation (4.2.4) which can be written as

$$\delta \nu_{sig} = - \nu \frac{t}{L_1} \delta n = - \nu \frac{t}{L_1} (\omega_p/\omega)^2 \qquad \text{(Hz)} \qquad (4.8.2.1)$$

The active length of the plasma is 10 cm, while the cavity mirror separation is 72 cm. Substitution into equation (4.8.2.1) gives for λ equal to 0.6328 μm

$$N_e = 8.582 \times 10^7 \, \delta \nu_{sig} \qquad (cm^{-3}) \qquad (4.8.2.2)$$

Electron number density at the tube centre deduced from the measured beat shift for different pressure and current values can be seen in figures (4.9a,b). The measured electron number density at the tube centre by this technique is compared with that deduced from the Stark broadening technique. These can be seen in figures (4.10a,b). It is evident that the electron number density shows the same characteristic behaviour as a function of current and pressure.

In figure (4.11) electron number density as a function of current during the decay is plotted with initial current as a parameter. This graph shows the same linear dependence of electron density on current as figure (4.10a). This suggests that the electron number density at any particular time during the decay is the steady state value corresponding to the current at that time.

We now consider the loss processes for He^+ and electrons in order to demonstrate that they are consistent with the electron number density following the discharge current on the time scale involved. We must first consider the cooling of the electrons in the decaying plasma.

The electrons can lose energy through elastic and inelastic collisions, but can also gain energy as a result of superelastic collisions with metastable or other excited states. For electron energies in excess of about 20 eV ($v_e > 10^8$ cm sec^{-1}) inelastic collisions can occur with ground state helium atoms, for which the total cross-sections is around 10^{-18} cm^2. The time between inelastic collisions is therefore around 3×10^{-7} sec at a pressure of 1 Torr. Even the high energy electrons (primary electrons with energies around 200 eV) will cool to around 20 eV in times less than 3 μ sec. The energy gain due to superelastic collisions during this time will be negligible since the metastable number density is 10^{-5} of the neutral atom density and the cross-section for the two processes are comparable (see Chapter VI).

The electrons can only cool below 20 eV by elastic collisions. In elastic collisions the electron looses its energy according to the relation

$$\frac{d\,U(t)}{dt} = -\frac{2m}{M}\,[U(t) - U_T]\,\nu, \qquad (4.3.8.1)$$

where m and M are electron and atom mass respectively, U(t) is the electron energy, U_T is the atom thermal energy and ν is the collision frequency. If we assume ν to be constant[65], then the energy decay is given by

$$U(t) - U_T = \Delta U_o \exp(-t/\tau), \qquad (4.8.3.2)$$

where

$$\tau = M/(2m\nu). \qquad (4.8.3.3)$$

and ΔU_o is the initial energy difference between the electrons and the gas. Substituting for ν in terms of the electron mean free path at 1 Torr, ℓ_o, we obtain for the time taken for the electrons to cool to within 10% of the gas temperature T_g

$$t_o = 1.4 \times 10^{-3} \frac{\ell_o A}{p T_g^{\frac{1}{2}}} \ln \left(\frac{\Delta U_o}{0.1 U_T}\right) \qquad (4.8.3.4)$$

where A is the molecular weight and p is the pressure (Torr) of the gas.

For electrons initially at 20 eV, for a gas temperature of 0.04 eV (300 ^{o}K) and assuming an electron mean free path at 1 Torr of 0.055 cm[66], then we obtain a characteristic time of about 140 μ sec at 1 Torr. The majority of electrons will initially be much cooler than 20 eV (around 0.1 eV) and will hence have a characteristic time around 60 μ sec at 1 Torr. This shows that throughout most of the plasma decay time, the energy loss is due to elastic collision.

We now consider the two loss processes for the electrons, namely diffusion and recombination. In the latter process, recombination can be with the helium ion already present in the discharge or with the He_2^+ which is created during the decay of the plasma. In order to assess the importance of this recombination mechanism we must consider the production rate of He_2^+. The He_2^+ is created basically as a result of the following two processes[67-69]

(a) $He^+ + 2He \xrightarrow{\nu_c} He_2^+ + He$, $\nu_c = 65p^2$ sec^{-1}

(b) $He(2^3S) + He(2^3S) \xrightarrow{\xi} He_2^+ + e$, $\xi = 2 \times 10^{-9}$ cm^3 sec^{-1}

where ν_c and ξ are the reaction conversion frequency and rate coefficient respectively. For a gas density of 3.5×10^{16} cm^{-3}, a metastable density of 5×10^{11} cm^{-3} and an ion number density of 10^{13} cm^{-3} the above two reactions give reaction rates of 6.5×10^{14} cm^{-3} sec^{-1} and 5×10^{14} cm^{-3} sec^{-1} respectively.

The He_2^+ is lost as a result of diffusion (the diffusion coefficient is about 650 ρ^{-1} cm^2 sec^{-1} where ρ is the pressure in Torr[69]) and recombination which occurs mainly through the processes[70,71].

(c) $He_2^+ + e \xrightarrow{\alpha_o} He^* + e$, $\alpha_o = 1.1 \times 10^{-8}$ cm^3 sec^{-1}

(d) $He_2^+ + 2e \xrightarrow{k_e} He_2^* + e$, $k_e = 2 \times 10^{-20}$ cm^6 sec^{-1}

(e) $He_2^+ + e + He \xrightarrow{k_{N_a}} He^* + 2He$, $k_{N_a} = 2 \times 10^{-27}$ cm^6 sec^{-1}.

For an electron density of 10^{13} cm^{-3}, and at an N_a of 3.5×10^{16} cm^{-3}, we find that the collision frequencies for the above reactions are 1.1×10^5, 2×10^6 and 7×10^2 sec^{-1} respectively. Furthermore the diffusion time is about 1.4×10^4 sec which is about one order of magnitude smaller than reactions (c) or (d), so it can be ignored.

Comparison between the total creation rate of He_2^+ (1.15×10^{15} cm^{-3} sec^{-1}) with the recombination collision frequency indicates that He_2^+ population in the discharge is about 10^9 cm^{-3}, which is about four orders of magnitude smaller than the measured He^+ density in the steady state case. Hence the number density of He_2^+ in the discharge can be neglected.

The He^+ is lost in the discharge as a result of ambipolar diffusion (its ambipolar diffusion coefficient is about 550 p cm^2 sec^{-1}[72]), reaction (a) and the following reactions[67,73,74]

(f) $He^+ + e \xrightarrow{\alpha_1} He^* + e$

(g) $He^+ + e + e \xrightarrow{k_{e1}} He^* + e$, $k_{e1} = 7.6 \times 10^{-20}$ cm^6 sec^{-1},

(h) $He^+ + e + He \xrightarrow{k_{ep}} He^* + He$, $k_{ep} = 10^{-11}$ p cm^3 sec^{-1}

Process (f) has a rate coefficient which is several orders of magnitude smaller than the others[73]. In fact it was neglected in most of the published work[67] and process (g) was regarded as the dominant mechanism[74]. The above reactions give collision frequencies of 7.6×10^6 and 10^2 sec^{-1} for an electron number density of 10^{13} and at 1 Torr of He. Again the diffusion time is 1.6×10^4 sec and can be ignored in comparison to reaction (g).

From the above it may be seen that the dominant recombination process is process (g) which gives reaction rate of 7.6×10^{19} cm^{-3} sec^{-1}.

This is five orders of magnitude larger than the recombination rate of He_2^+.

The above study shows that the recombination process initially has a characteristic time less than 1 μ sec. During the decay of the current the electron density is therefore in a steady state condition with respect to the current.

Late in the decay of the current, after say 100 μ sec when the electron density has fallen to about 25% of its initial value, the characteristic time for recombination will have increased by a factor of 16. Eventually it will become comparable to the characteristic times for diffusion loss (160 μ sec at 1 Torr) and current decay.

Table (4.1)

The resonant frequency of an optical cavity consisting of two spherical mirrors with radii b_1 and b_2 separated by distance d is

$$\nu = \frac{c}{2d}[q + (1 + m + n)\, f] \qquad \text{(Hz)} \qquad (1)$$

where

$$f = \pi^{-1} \cos^{-1}\left[\left(1 - \frac{d}{b_1}\right)\left(1 - \frac{d}{b_2}\right)\right] \qquad (2)$$

For each value of (m + n) there is a set of frequencies with common separation (c/2d) corresponding to $\Delta q = 1$. This frequency is a longitudinal frequency and has a transverse mode set. The frequency difference between the mode sets is

$$\Delta\, \nu_{\Delta(m+n)} = \frac{c}{2d}\, f\, \Delta\, (m + n) \qquad \text{(Hz)} \qquad (3)$$

If there are many modes oscillating simultaneously many beat frequencies will result and these are summarized as follows:

Laser (1) b_1 = 100 cm, b_2 = 200, d = 72 cm, $\Delta(m + n) = 1$, f = 0.44

From equation (3) we get $\Delta\nu_1$ = 91.7 MHz

$\Delta(m + n)$	possible beat frequencies frequencies whose sum is $\Delta\ \nu_1$		frequencies at left + $\Delta\ \nu_1$	
	ν_1'	$\Delta\nu_1 - \nu_1'$		
1	40.35	51.35	132.05	143.05
2	80.7	11.0	172.4	102.7
3	29.3	62.4	121.0	154.1
4	69.7	22.0	161.4	113.7

Laser (2) b_1 = 100 cm, b_2 = 100 cm, d = 42 cm, $\Delta(m + n) = 1$, f = 0.39.

From equation (3) we get $\Delta\nu_1$ = 139 MHz

$\Delta(m + n)$	frequencies whose sum is $\Delta\nu_1$		frequencies at left + $\Delta\ \nu_1$	
	ν_2'	$\Delta\nu_1 - \nu_2'$		
1	54.2	84.8	193.2	176.5
2	108.4	30.6	247.9	169.6
3	23.6	115.4	162.6	254.4
4	77.8	61.2	216.8	200.2

$\nu'_{1,2} = [f\, \Delta(m + n) - s]\ \Delta\nu_1$ where s is an integer necessary to make the results less than $\Delta\nu_1$.

Table (4.2a)

λ μm	$N_e = 10^{13}$ cm^{-3} $\frac{1}{2}(\omega_p/\omega)^2 \times 10^9$	$N_e = 10^{15}$ cm^{-3} $\frac{1}{2}(\omega_p/\omega)^2 \times 10^7$
0.488	1.05	1.05
0.515	1.17	1.17
0.6328	1.77	1.77
1.15	5.84	5.84
3.39	50.7	50.7
10.6	496	496

Table (4.2b)

N_e(cm^{-3})	$\frac{1}{2}(\omega_p/\omega_{0.6328})^2$	$\frac{1}{2}(\omega_p/\omega_{1.15})^2$	$\frac{1}{2}(\omega_p/\omega_{3.39})^2$
10^{10}	1.77×10^{-12}	5.84×10^{-12}	50.7×10^{-12}
10^{11}	1.77×10^{-11}	5.84×10^{-11}	50.7×10^{-11}
10^{12}	1.77×10^{-10}	5.84×10^{-10}	50.7×10^{-10}
10^{13}	1.77×10^{-9}	5.84×10^{-9}	50.7×10^{-9}
10^{14}	1.77×10^{-8}	5.84×10^{-8}	50.7×10^{-8}
10^{15}	1.77×10^{-7}	5.84×10^{-7}	50.7×10^{-7}

Table (4.2c)

λ_{nm} (μm)	f_{nm}	α (cm^3)	$2\pi\alpha N^*$
λ = 0.6328 μm		($N^* \simeq 5 \times 10^{11}$ cm^{-3})	
0.5016	0.1514	7.2×10^{-24}	2.3×10^{-11}
0.5048	0.00834	9.3×10^{-24}	2.9×10^{-11}
0.5876	0.609	1.1×10^{-22}	3.4×10^{-10}
0.6678	0.711	-1.96×10^{-22}	-6.2×10^{-10}
0.7065	0.0693	-8.7×10^{-24}	-2.7×10^{-11}
0.7281	0.0480	-5.18×10^{-24}	-1.63×10^{-11}
λ = 1.15 μm			
1.1013	0.0521	5.44×10^{-23}	1.71×10^{-10}
1.1045	0.0553	5.98×10^{-23}	1.95×10^{-10}
1.1225	0.0069	1.31×10^{-23}	4.1×10^{-11}
1.1969	0.123	-1.54×10^{-22}	-4.8×10^{-10}
1.2528	0.0429	-2.57×10^{-23}	-8.1×10^{-11}
λ = 3.39 μm			
2.7600	0.0274	4.4×10^{-23}	4.4×10^{-11}
2.8542	0.0468	9.3×10^{-23}	2.9×10^{-11}
3.3299	0.1510	3.4×10^{-21}	1.1×10^{-8}
3.7026	0.4420	-2.2×10^{-21}	-6.9×10^{-9}
4.0053	0.0240	-6.9×10^{-23}	-2.2×10^{-11}
λ = 0.6328 μm		($N^* = 10^{10}$ cm^{-3})	
0.6563 (Hα)	0.6407	2.59×10^{-23}	1.63×10^{-12}

Expected drifts due to environmental changes

Table (4.3a)

Parameter	$\Delta \nu_q/\nu_q$ per sec: N_e 10^{13} cm^{-3}	N_e 10^{10} cm^{-3}	Atmospheric Temperature	Atmospheric Pressure	Expansion of granite block	Cooling of tube	Optical Path Change
Prevailing conditions	minimum change in the electron density of the hollow cathode	maximum change in the electron density of the He-Ne laser discharge	$\frac{dT}{dt} = 5.5 \times 10^{-5}$ °C s^{-1}	$\frac{dP}{dt} = 2.8 \times 10^{-4}$ Torr s^{-1}	$\frac{dL}{dt} = 3.96 \times 10^{-9}$ cm s^{-1}		$\Delta\theta$ changes by 10^{-6} rad sec^{-1} window thickness of 3 mm, glass refractive index of 1.5 and cavity length of 42 cm.
			Assuming that the fractional open part of the cavity is 0.24				
.6328 μm	2.1×10^{-9}	5×10^{-12}	1.2×10^{-10}	2.4×10^{-10}	5.5×10^{-11}	3.3×10^{-12}	3.79×10^{-9}
1.15 μm	2.1×10^{-9}	5×10^{-10}	2×10^{-10}	4.1×10^{-10}	9.4×10^{-11}	5.6×10^{-12}	3.79×10^{-9}

JITTER

Table (4.3b)

$\frac{\Delta \nu_q}{\nu_q}$

Parameter	Vibration	Draught
Prevailing Conditions	Air born vibration in the frequency range of 300 - 1200 Hz causes jitter of 0.1 MHz	due to the air current the effect of air current causes jitter of 0.1 MHz
λ = 0.6328 µm	2.1×10^{-10}	2.1×10^{-10}
λ = 1.15 µm	3.8×10^{-10}	3.8×10^{-10}

Table (4.3c)

Drifts and Jitters in decaying plasma

The maximum values of the drift and jitter due to environment changes for the factors in tables (4.3a,b) under the same prevailing conditions for decaying plasma conditions of 150 mA and 200 μ sec.

Parameter	change in the electron density of the He-Ne laser discharge	Atmosphere changes in ΔT	ΔP	expansion	cooling	vibration	optical path change	draught
$\frac{\Delta \nu_q}{\nu_q}$	5×10^{-16}	1.7×10^{-13}	3.4×10^{-13}	1.9×10^{-14}	1.1×10^{-15}	7.6×10^{-13}	7.6×10^{-13}	7.6×10^{-1}

Table (4.4)

	Laser 1				Laser 2					
λ (μm)	W_o	Z_A	W_1	R_1	W_o	Z_A	W_2	R_2	δ	x
μm	mm	cm	mm	cm	mm	cm	cm	cm	cm	mm
0.6328	0.29	21	0.46	100	0.31	13	0.34	175	1.54	1.75
1.15	0.38	21	0.62	95	0.42	13	0.45	170	2.1	2.2

Gaussian beam parameters: Laser L, $R_{A_1} = R_{B_1} = 1$ m, d = 42 cm,

Laser 2, $R_{A_2} = 2R_{B_2} = 2$ m, d = 72 cm, see figure (4.1).

W_1, W_2, R_1, R_2 are the beam diameters and radii of curvatures at the photodiode, which is 65 and 23 cm from Laser (1) and Laser (2) respectively.

Table (4.5a)

Δ	$\Delta N_a/\Delta N_e$	Ratio of atom to electron effects at 0.6328 μm
0.45	33	0.23
0.50	17.4	0.12
0.51	13.8	0.09
0.52	10.4	0.07
0.53	7.0	0.05
0.54	3.5	0.025
0.55	0	0
0.56	- 3.59	- 0.025
0.57	- 7.2	- 0.05
0.58	- 10.9	- 0.076
0.59	- 14.7	- 0.103
0.60	- 18.5	- 0.13
0.70	- 60.6	- 0.42
0.80	- 111	- 0.78
0.90	- 172	- 1.21
1.00	- 248	- 1.79
1.30	- 653	- 4.57
1.50	- 1344	- 9.41
1.80	- 28289	-198

Table (4.5b)

Pressure	Time (μ sec)	Δ
3 Torr	15	0.530
	25	0.510
	40	0.525
	55	0.540
	63	0.505
	76	0.525
	82	0.516
8 Torr	10	0.526
	25	0.54
	33	0.500
	43	0.512
12 Torr	12	0.524
	24	0.523
	38	0.526

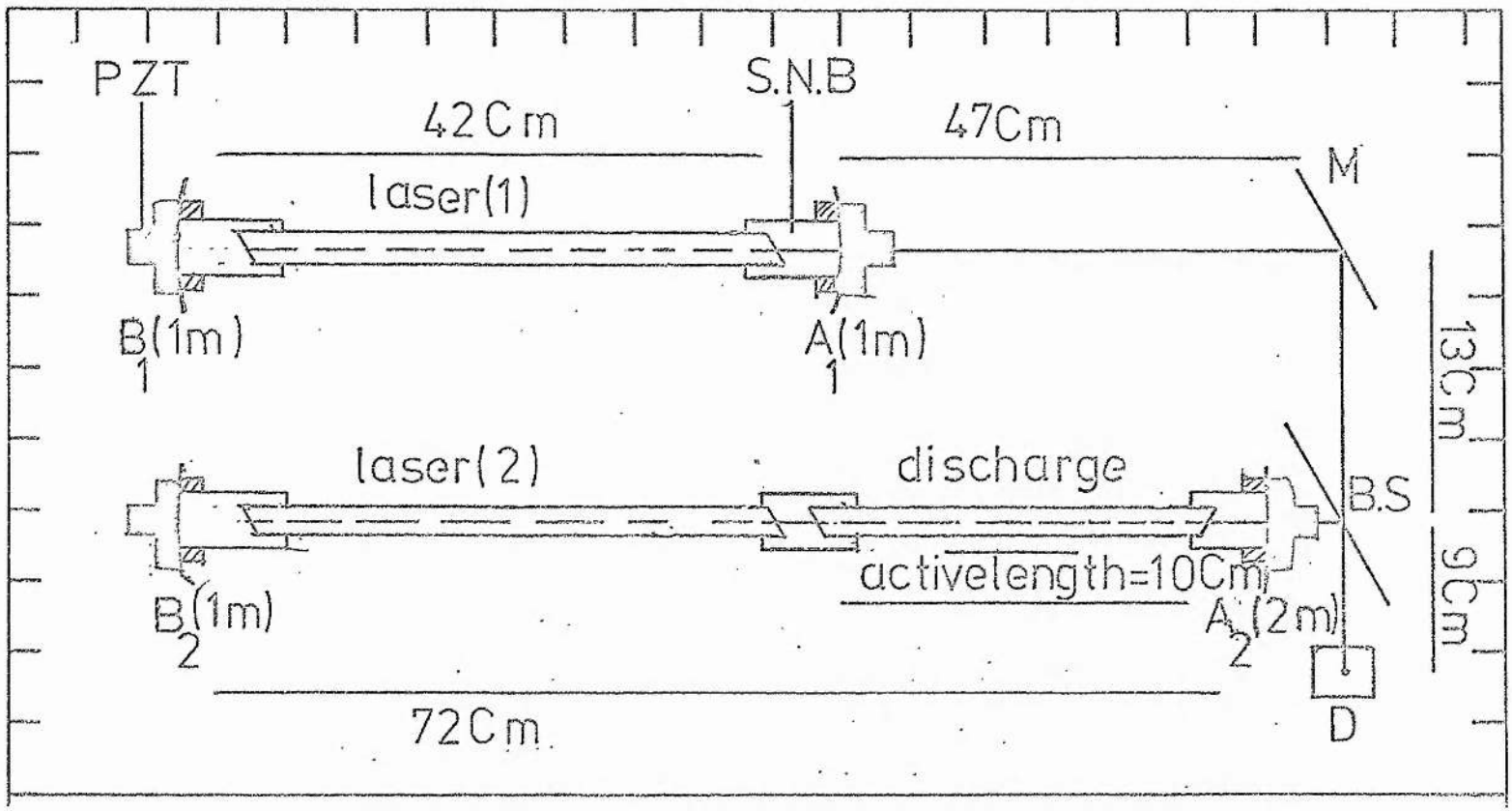

Figure 4.1 · The laser system arrangement laser (1) is reflected by mirror (M) and combined with laser (2) by the beam splitter (BS) and the combined beam was detected by the photodiode D. Each cavity mirror (A_1 ; B_1, A_2 and B_2) mount has a piezoceramic transducer (PZT) and the empty space between the cavity mirror and the laser (discharge in the case of mirror B_1) was filled by sliding nylon bushes (SNB).

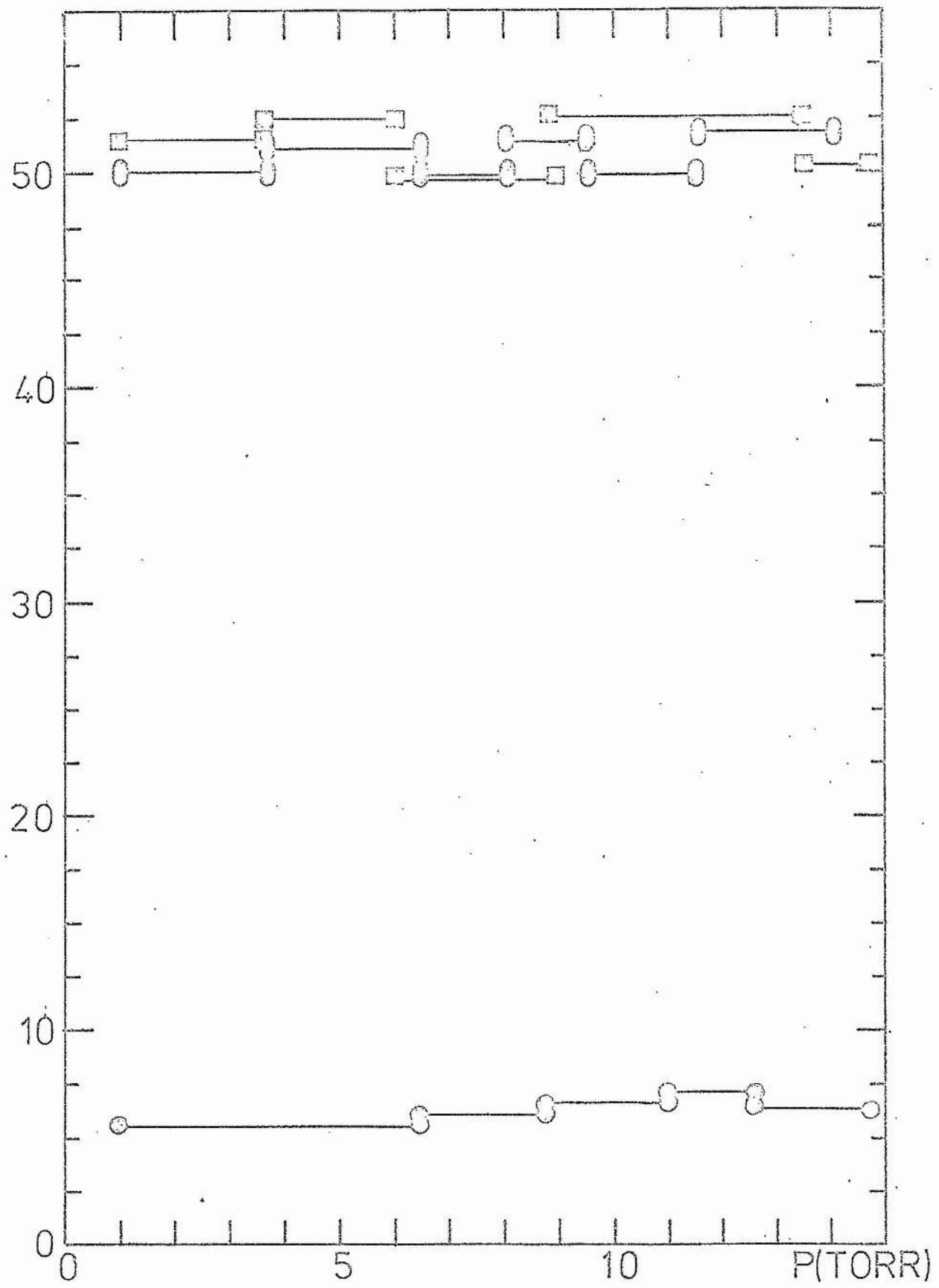

Figure 4.2 . The beat drift as a function of the gas pressure for different gases. ⊙ He, ⬯ Ar and ⬚ N_2.

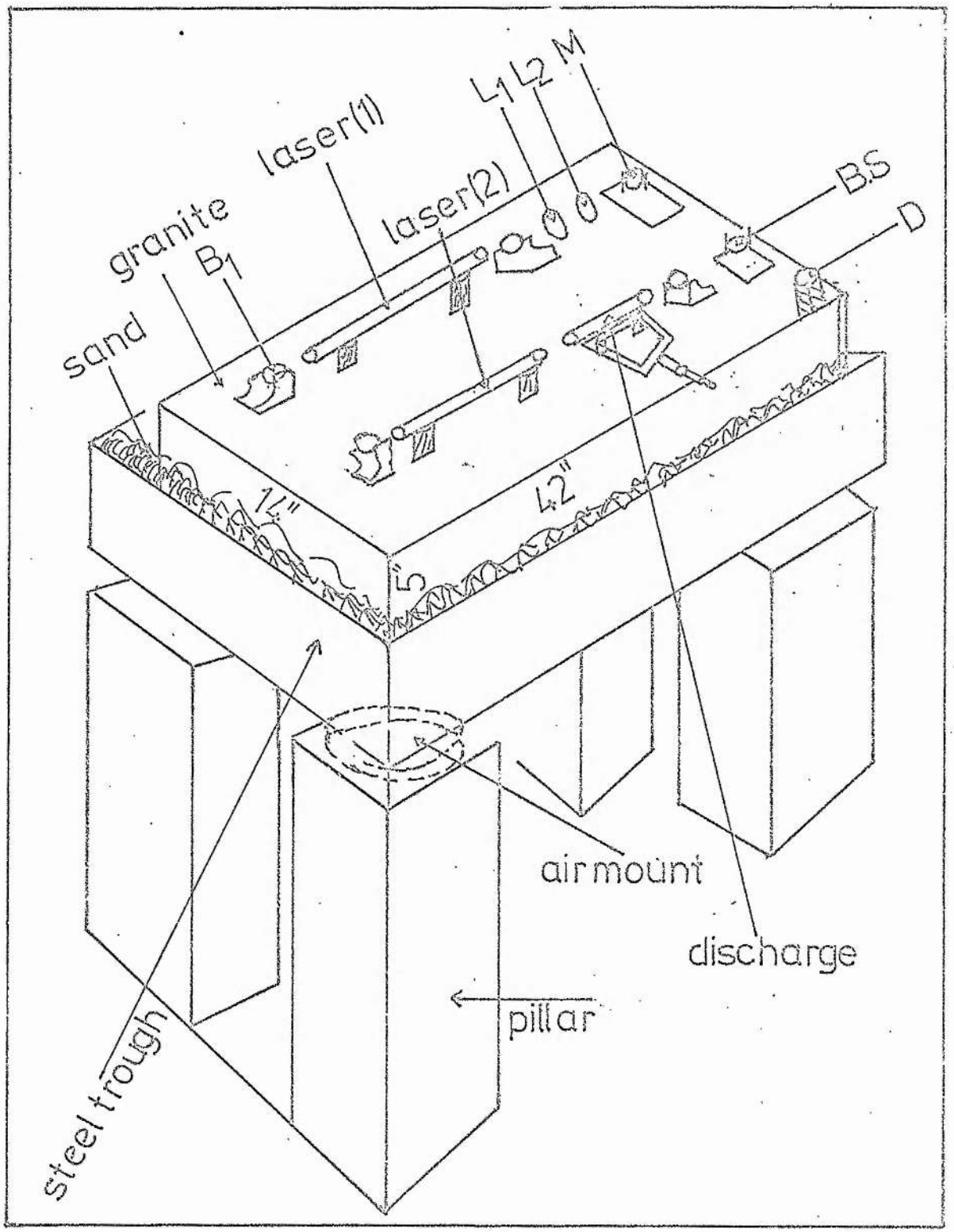

Figure 4.3 . A detailed diagram of the system construction and the laser set up on it.

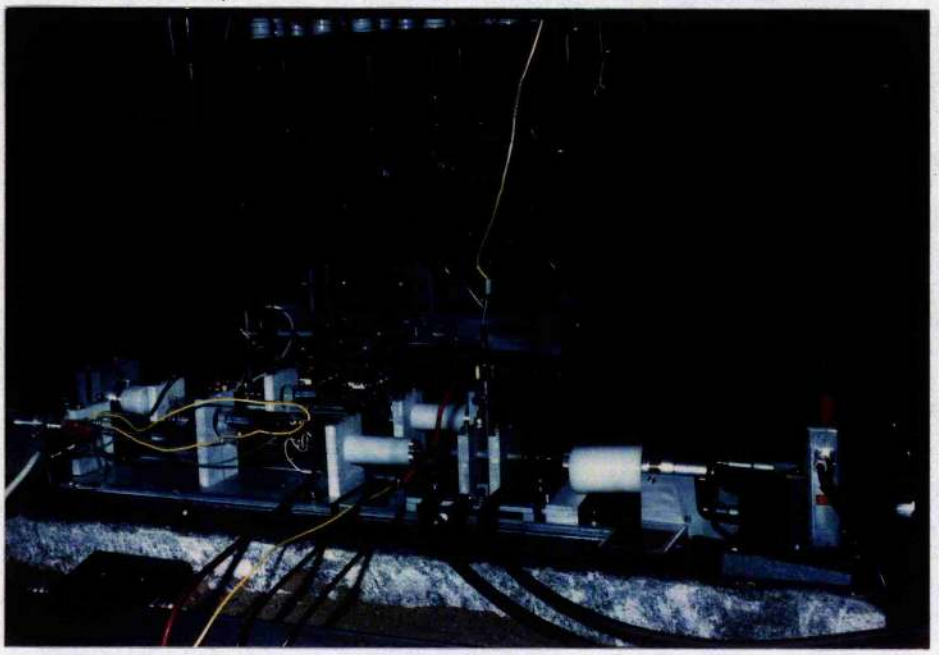

Figure 4.3. The laser heterodyne system.

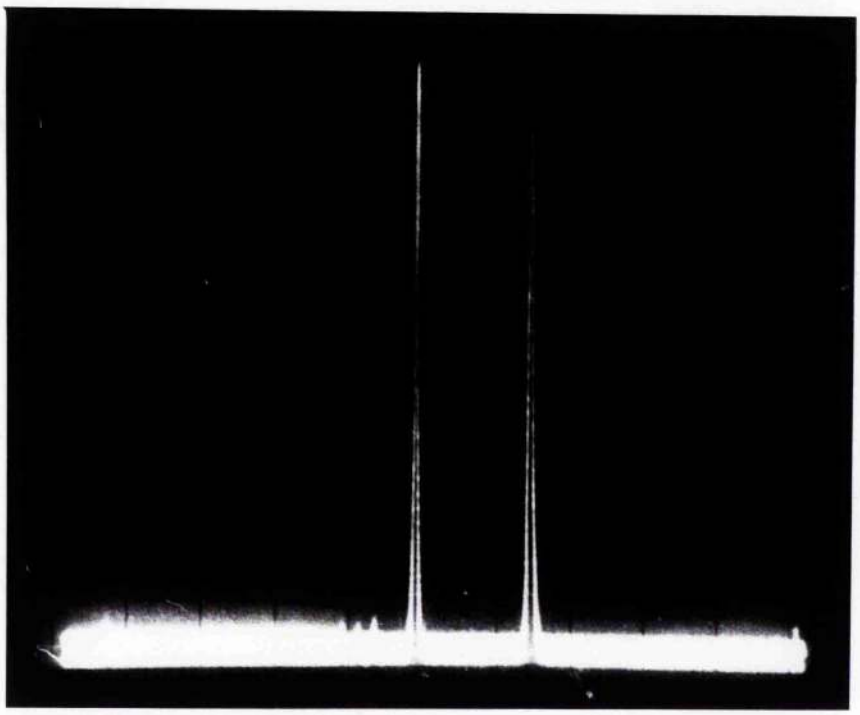

Figure 4.4. A typical beat signal on the spectrum analyser.

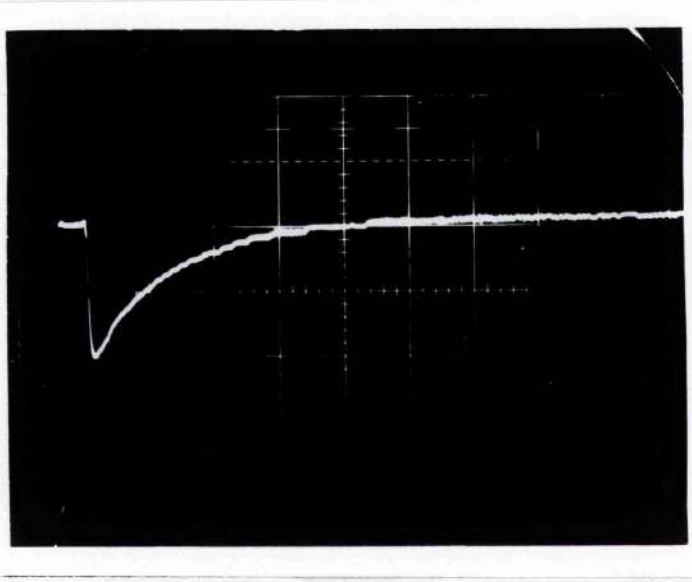

Figure 4.5. A typical current decay. Horizontal 50 μ sec/cm.

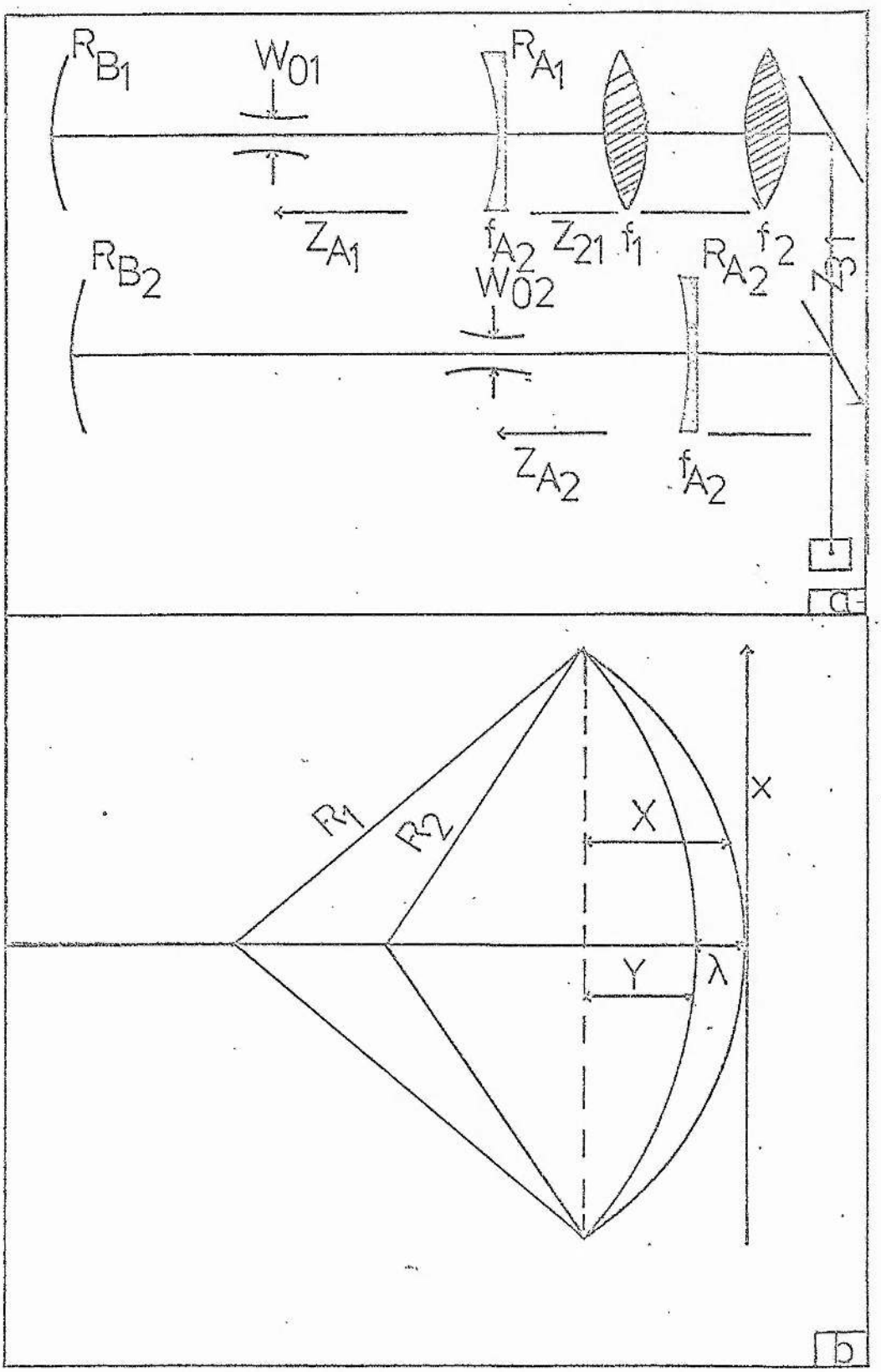

Figure 4.6a,b. Figure a is to illustrate the optical system used for beams diameters and wave curvatures matching. b is to show the coherence between the two wave fronts.

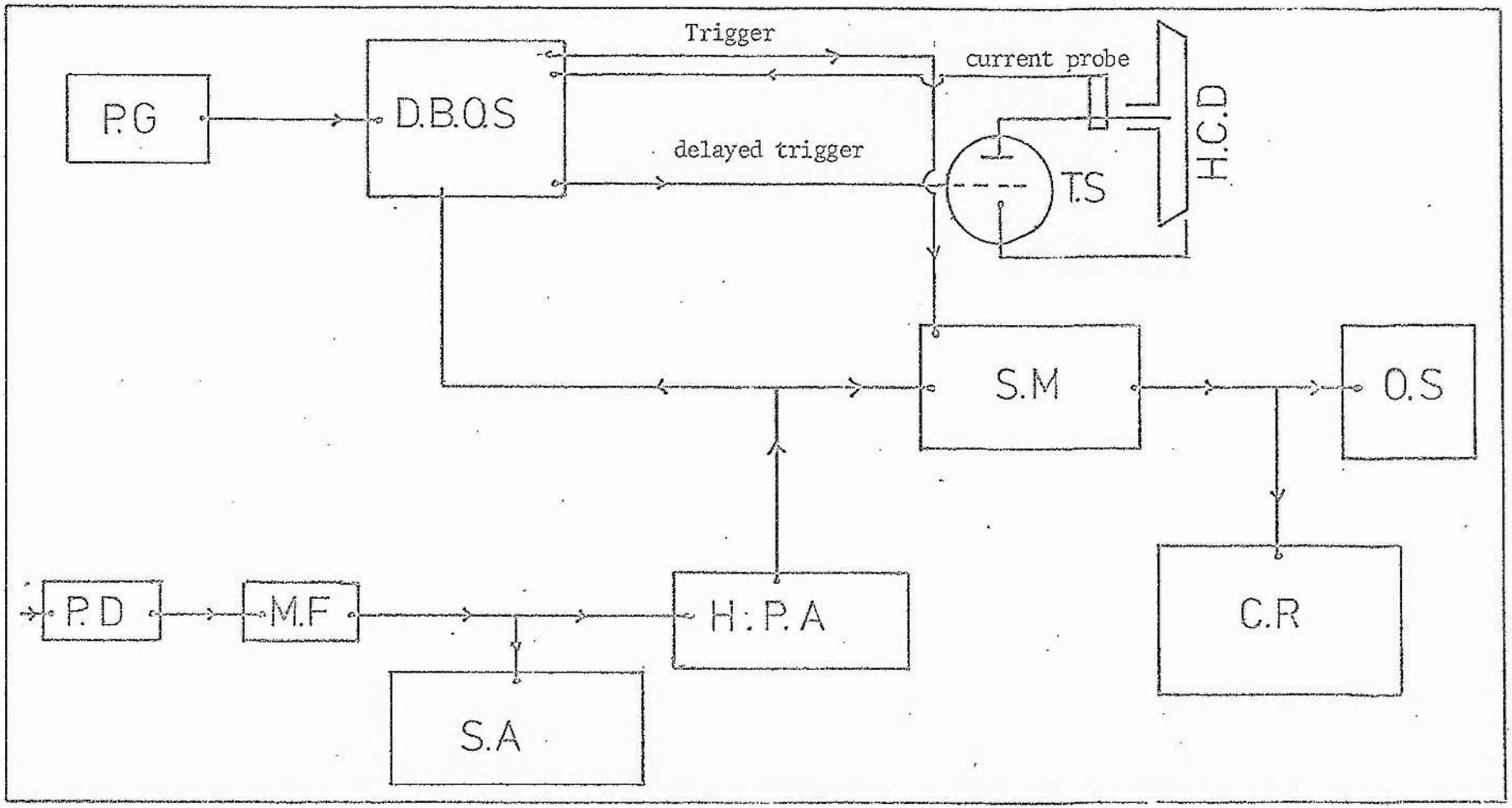

Figure 4.7. A block diagram of the detection system. The beat frequency detected by the photodiode (PD) filtered through the mains filter (MF) and then displayed on the spectrum analyser (SA). The signal is then amplified by (HPA) and then displayed on the dual beam scope (DBOS). This scope is triggered by the pulse generator (PG). The trigger of the (DBOS) triggers the storage memory (SM), the scope (OS) and the chart recorder (CR). A delay trigger from the scope triggers the thyratron (TS) and in turn the discharge (HCD). This delay enables us to display the beat signal before and after the crowbarring of the discharge.

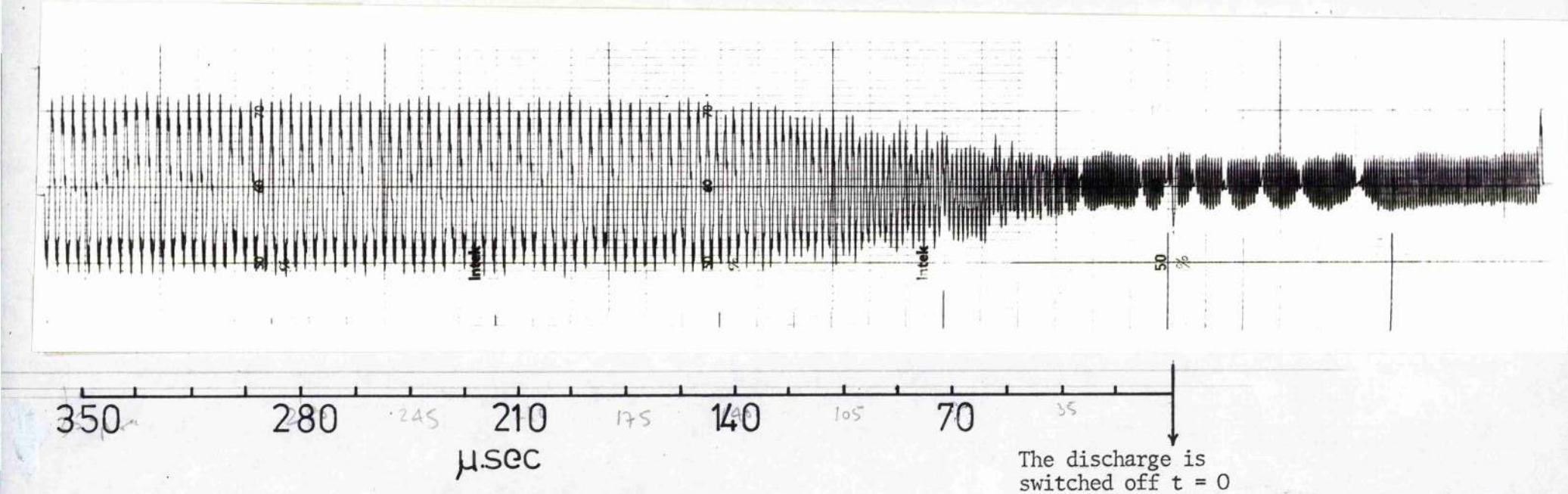

Figure 4.8. A typical chart recorder trace of the beat frequency as the plasma current decays. Notice that the beat frequency decreases as the decay time increases.

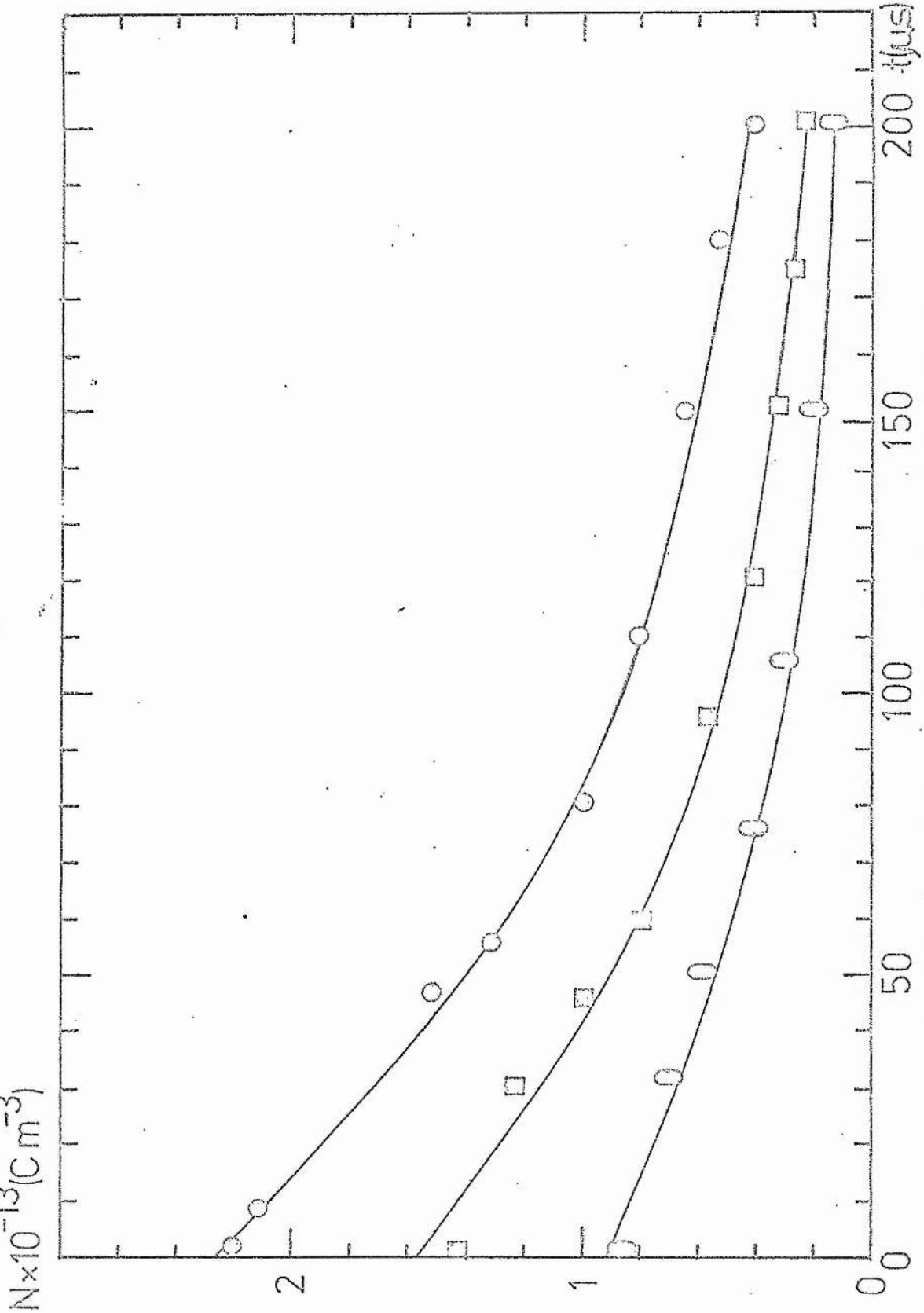

Figure 4.9a . The electron number density as a function of the plasma decay time at constant helium pressure of 5 Torr and initial discharge currents of ○ 150 mA, □ 100 mA and ◯ 50 mA.

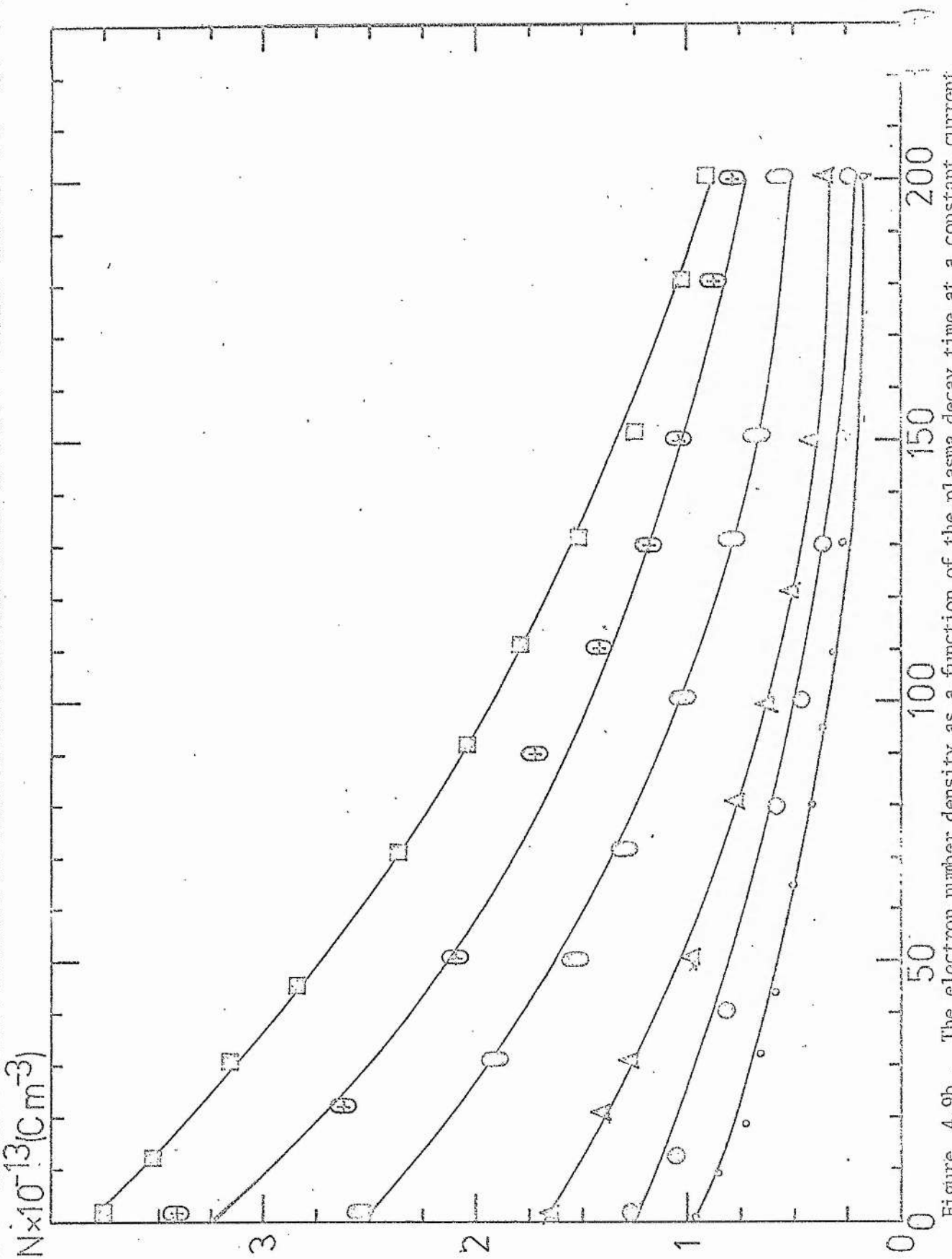

Figure 4.9b . The electron number density as a function of the plasma decay time at a constant current 100 mA and different pressure values ⊕ 1 Torr, ∘ 3 Torr, Δ 5 Torr, □ 10 Torr, ⊙ 12 Torr and ○

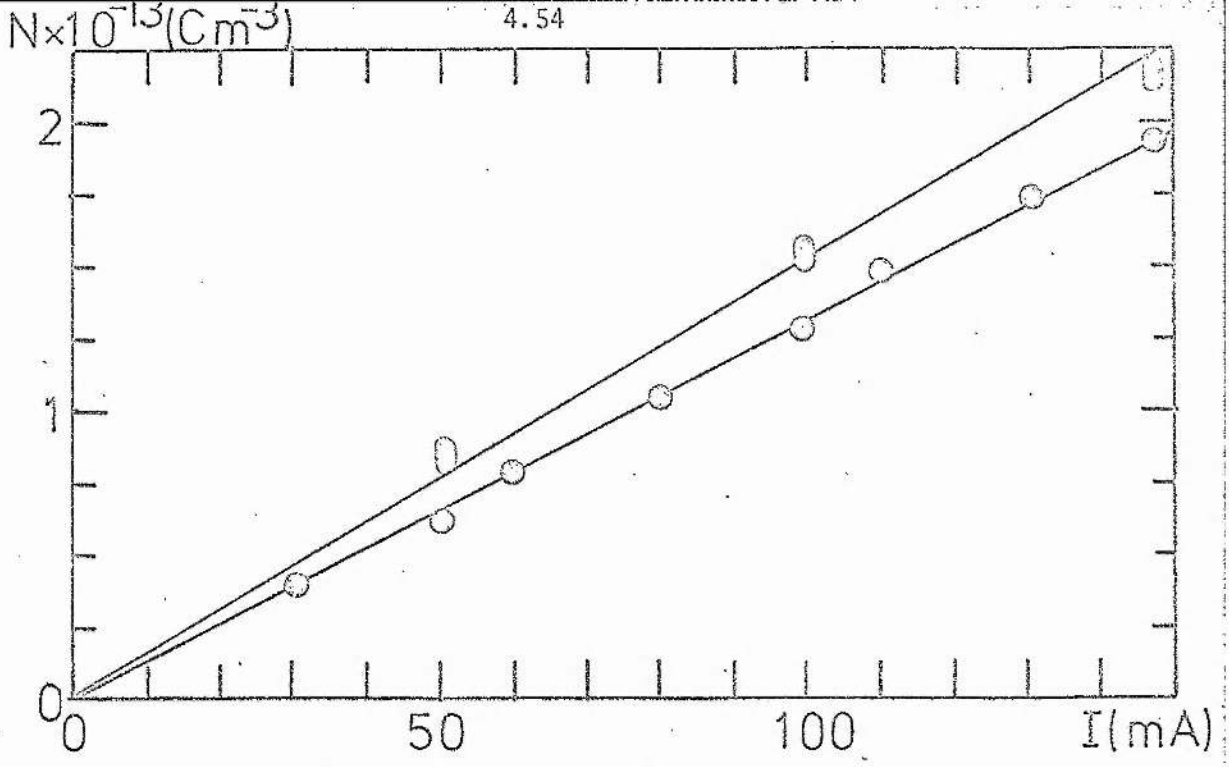

Figure 4.10a . The electron number density as a function of current and a constant pressure of 5 Torr measured by ○ Stark technique and ⊖ by laser heterodyne technique.

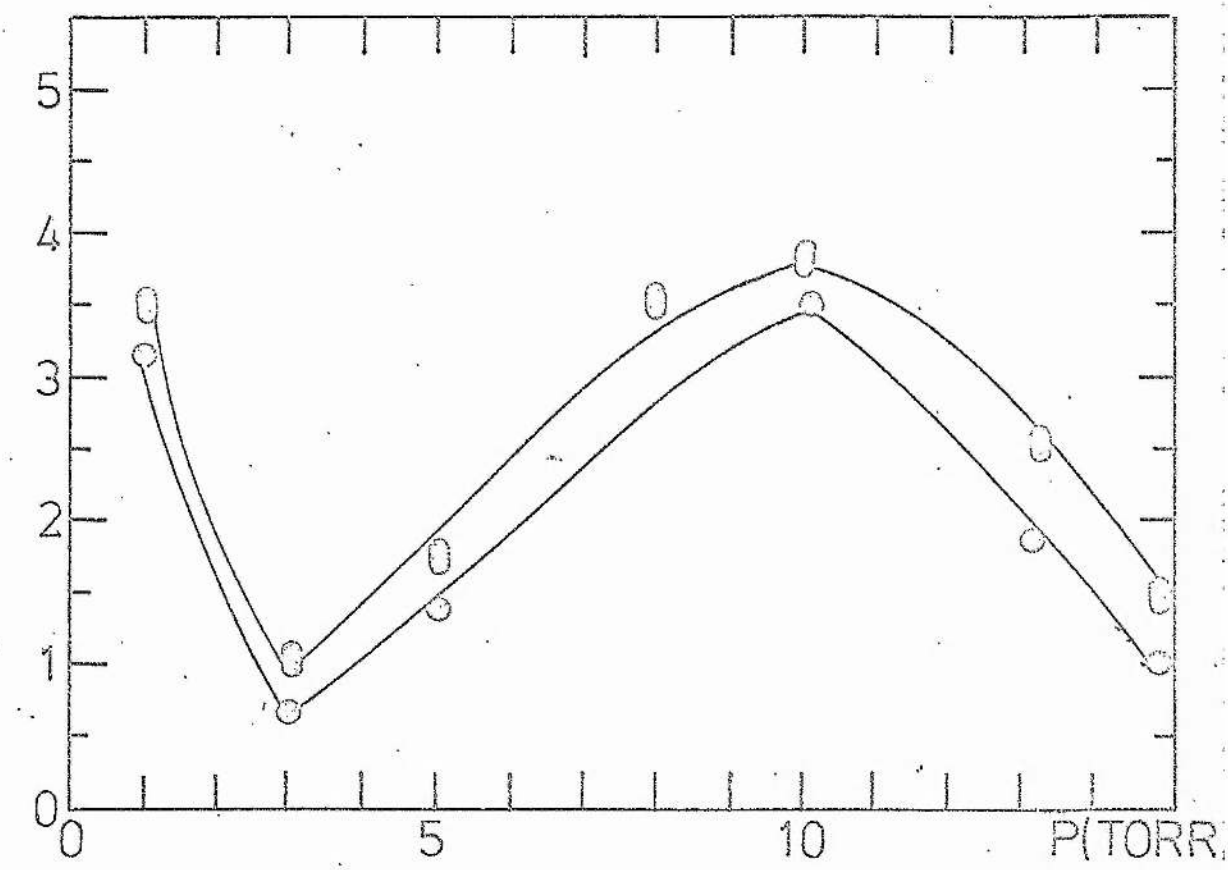

Figure 4.10b . The electron number density as a function of the pressure at a constant current of 100 mA measured by ○ Stark technique and ⊖ laser heterodyne technique.

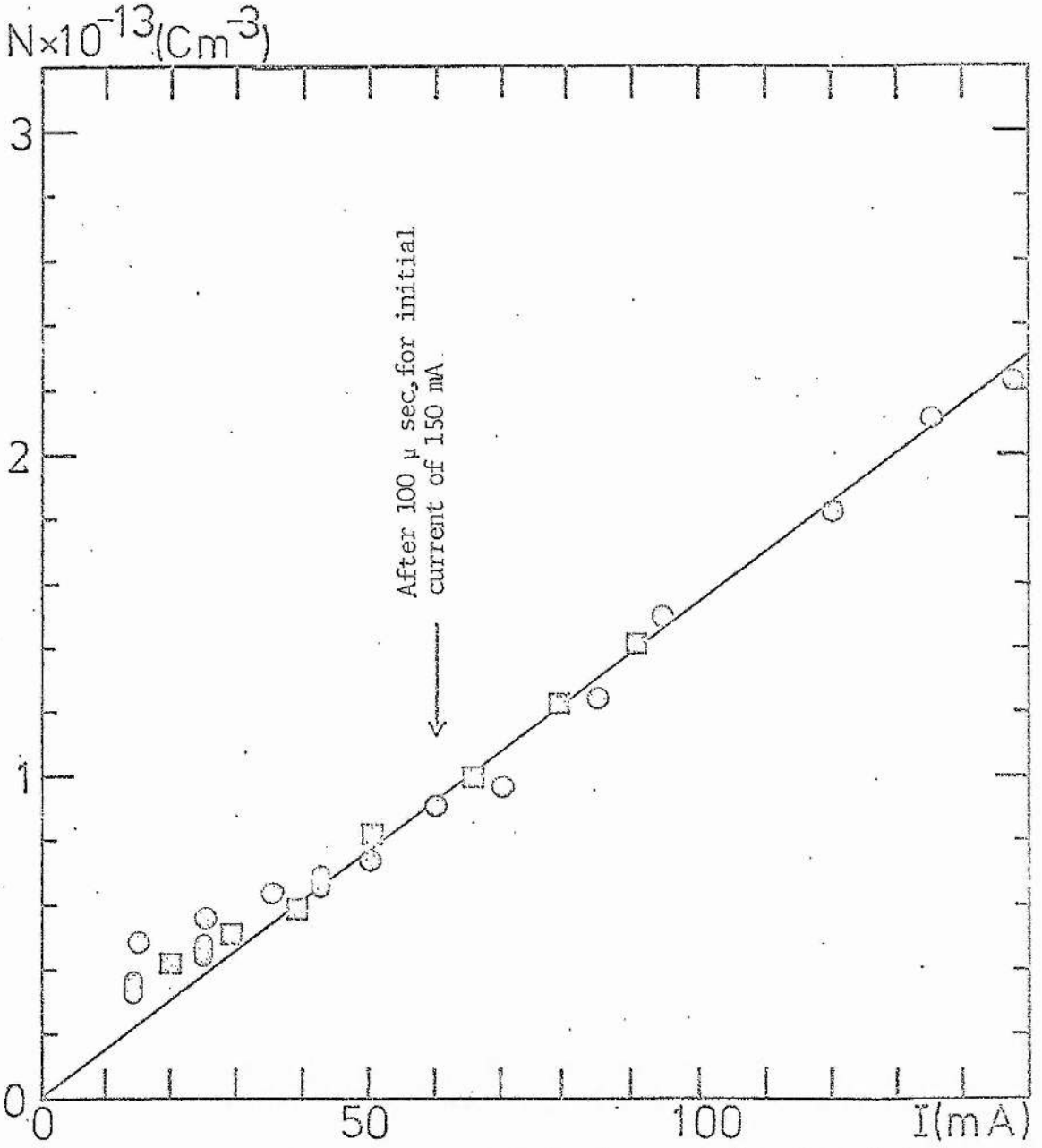

Figure 4.11 . The electron number density as a function of the discharge current at any time during the decay for different initial currents ○ 150 mA, □ 100 mA and ⌀ 50 mA , and a constant pressure of 5 Torr.

CHAPTER V

THE EMISSION RADIAL PROFILES IN THE NEGATIVE GLOW

5.1 Introduction

In a hollow cathode discharge, most of the excitation occurs in the negative glow as a result of collisions between electrons and helium atoms and ions. The colliding electrons are; primary electrons which have energy derived from the cathode fall potential and secondary electrons which result from collisions between primary electrons and atoms.

The primary electrons are created in the cathode dark space. As they enter the negative glow they lose their energy continuously along their path towards the tube centre. The study of the emission radial profiles gives information about the primary electron energy variation as a function of distance from the tube centre. Furthermore, as the electrons move in the discharge they interact with other particles, hence changing the shape of the total electron energy distribution. In this chapter the emission radial profiles of 3889 Å ($3p^3P - 2s^3S$), 5016 Å ($3p^1P - 2s^1S$), 5876 Å ($3d^3D - 2p^3P$), 4686 Å (He II, n = 4-3) and 6560 Å (He II, n = 6-4) will be presented. (see figure 5.1a) The radial profiles reach a maximum at the tube centre at low helium pressures while they reach a maximum value at the edge of the negative glow at high pressures.

The dependence of the emission on the electron number density and energy will be studied by conditioning the cathode surface using the discharge current and by using a transverse magnetic field.

Adding a metal to the discharge may change the electron energy distribution. This will be checked by studying the emission on the cadmium ion transitions at 4416 Å ($5s^2D^2_{5/2}$-$5p^2P_{3/2}$) and 5378 Å ($4f^2F_{7/2}$ - $5d^2D_{5/2}$). (see figure 5.1b)

5.2 Apparatus

The essential optical arrangements can be seen in figure (5.1c). A converging lens images two diaphragms into two circles in the near and far ends of the discharge tube (see figure 5.1d). If the diameters of the

two diaphragms are equal, their images in the discharge tube will approximately define a cylinder with radius r, from which light passes through the diaphragms. Any ray of light passing through the two diaphragms and so collected by the monochromator must have originated from atoms in the above cylinder defined by their images. However, the monochromator will only receive light emitted by these atoms over a small range of angles. This may be looked at as a disadvantage in the gathering power of the system, but a second look shows that if we allow the monochromator to receive light at large angles, this leads to the system accepting light from anywhere in the tube and the whole advantage will be lost.

The two diaphragms S_1 and S_2 are located in the planes P_1 and P_2 respectively, their image planes in the discharge are P_1' and P_2' respectively (see figure 5.1d).

Light from the diaphragm image in P_1' is collected by S_2, since S_2 is less than the tube diameter (6mm), then diffraction at S_2 must be considered. If there is diffraction at S_2, then the light diffracted may pass through S_1 and the field of view is no longer cylindrical. To preserve a cylindrical field of view the radius of S_1 must be less than the end image of the cylinder by an amount[75]

$$\frac{\ell_1}{\ell_1'} \quad \frac{0.61\lambda D}{r} \qquad (5.2.1)$$

where ℓ_1 and ℓ_1' are the conjugate distances to P_1 and P_1', D is the length of the cylinder and λ is the wavelength.

To study the radial profiles, the discharge tube was imaged by a plane laser mirror positioned at the discharge tube end and inclined at 45°. The laser mirror was mounted on a cradle, which could be driven by a micrometer (see figure 5.1c). The radial movement of the tube was achieved by moving the mirror on the cradle across the discharge tube.

This in effect scans the discharge image in front of the two diaphragms and along its axis by 0.5 cm. The latter leads to a change in magnification value by 4% which is negligible. The micrometer was connected to the X-channel of an X-Y recorder, so the micrometer movement scans the recorder.

In the studied discharge the length of the plasma column is dependent on the discharge parameters. To do this experiment the image of the plasma column must always lie between the two diaphragms S_1 and S_2, for only in this case will there by a cylindrical field of view in the plasma and will the light collection efficiency be constant along the axis. From Chapter II we can see that the maximum value of the plasma column is less than 10 cm. Adding to this 0.5 cm introduced from the radial movement of the mirrors, we can say that the plasma column reaches a maximum value of 10.5 cm, which should be taken as the minimum distance between the images of the two diaphragms S_1 and S_2 in the discharge.

The diameter of the diaphragm S_2 is determined by the resolution required. A 100 μ pinhole was used, and for the present magnification (3.6) this gives approximately eighteen resolvable points across the discharge tube.

5.3 Factors affecting the radial profiles

I] The effect of achromaticity: the lens used is a UV achromat of 20 cm focal length. Since the focal length depends on λ, so does the axial extent of the field of view. McKenzie[8] showed that for an optical arrangement similar to this changing λ between 2200 Å and 5900 Å changes the field of view by 8%. In our case λ varies between 3889 Å and 6560 Å, hence the change in the axial field of view is expected to be less than 8%.

2] The instrumental distortion: the instrumental distortion of the radial profiles was studied by Webb[75], and it was found that it depends on the ratio Z, of the aperture image to the tube radius. For Z = 0.2, the distortion is negligible at the tube centre and reaches a value of 7% at the profile edge. In the present case Z is 0.1, so the instrumental distortion is not expected to exceed 7%.

3] Self-absorption: some of the above transitions such as 3889 Å and 5016 Å, terminate on a metastable level, so their radial emission profiles are distorted by self-absorption. The self-absorption was corrected by using the measured (2^3S) and (2^1S) number densities which are presented in Appendix II. It was found that for maximum metastable number density the self-absorption effect does not exceed 14%.

The above considerations suggest that the presented radial profiles should represent the true behaviour of the excitation across the negative glow.

Before any results were taken the system was aligned, first coarsely by a He-Ne laser and finally by a collimating telescope with focal length between zero and infinity.

5.4 The emission of helium neutral and ion transitions

In the following the emission of the aforementioned transitions as a function of the discharge parameters (current and pressure) and their radial profiles will be presented.

5.4.1 The emission as a function of the discharge current and pressure

The emission of 5876 Å, 3889 Å, 5016 Å and 4686 Å at the tube centre as a function of the discharge current and helium pressure can be seen in figures (5.2a,b, in these figures and throughout this chapter the spontaneous emission intensities (SEI) are in arbitary units (AU)). At a constant pressure, the emission increases linearly with the discharge current for the current range of 0-150 mA. This was observed at every radial point in the discharge. The results plotted

in figure (5.2a) are not corrected for changes in the plasma length. If this is done the emission intensity shows a slight sublinear dependence on current. However, the length correction assumes that the plasma is uniform axially and hence there is an over correction.

The above linear dependence was seen on all the He and He^+ transitions investigated, indicating that the populations of the upper levels of the three transitions depend linearly on the discharge current. Hence excited state and ionic state populations follow the behaviour of triplet metastable density and electron number density with current. The singlet metastable density is anomalous in its behaviour as a function of current, saturating for currents higher than 40 mA.

Furthermore, both the He transitions (5016 Å, 3889 Å and 5876 Å) which require electron energy in the range of 20 eV and the He^+ transitions (4686 Å) which require electron energy in excess of 50 eV [76] to be excited behave similarly as a function of the discharge current. At a constant current the spontaneous emission of the above transitions decreases monotonically with increasing helium pressure. This decrease occurs at current values of 0-150 mA and at any radial point in the discharge. These results are not corrected for plasma length changes but even if this is done the monotonic decrease is still observed.

The behaviour of excited neutral and ionic state densities with pressure is to be contrasted with that of the electron and triplet metastable densities. Whereas the former decrease monotonically with increasing pressure, the latter follow the cathode fall potential in its variation with pressure. The behaviour of the singlet number density is again anomalous in that it saturates with increasing pressure after 2 Torr.

5.4.2 The emission radial profiles

The radial profiles of 3889 Å, 5016 Å, 5876 Å, 4686 Å and 6560 Å are presented in figures (5.3a,b).

At low pressures the radial profiles reach a maximum value at the tube centre and at high pressures (p > 12 Torr) the radial profiles reach a maximum value at the negative glow edge while they reach a minimum value at the tube centre.

It is interesting to notice that radial profiles of excited neutral and ionic states are similar in shape to those shown by the singlet and triplet metastable states for all values of pressure and current.

Profiles of the excited ionic states are proportionally greater towards the edges of the discharge compared to those of the excited neutral states. This difference is observed at all pressures. This difference is perhaps due to the large difference in energy required to excite ionic (75 eV, see below) as opposed to neutral (20 eV) states. The proportion of high energy electrons will decrease in moving towards the tube centre, since these originate in the cathode fall region. Hence ionic excitation will be favoured closer to the cathode fall.

The presence of emission on the 4686 $\mathring{A}$ transition at the centre of the discharge is an indication of high energy electrons there with energies of 50 or 75 eV, depending on the process populating the upper level of 4686 $\mathring{A}$(n=4). This level may be populated as a result of electron excitation from the helium neutral ground state, the helium ion ground state or the (2^3S) state. The cross-section for the direct electron excitation from the neutral ground state assumes maximum value of 10^{-20} cm^2[96] at an electron energy of 150 eV. There are no data available about the direct electron cross-sections from either the helium ion ground state or the 2^3S state. However the direct electron excitation cross-section from the helium ion ground state can be compared with the cross-section for excitation from the He^+ ground state to the $1s^2P$ of He^+ which reaches a maximum value of 7.5×10^{-18} cm^2[97] at an electron energy of 50 eV. If we assume that this is the cross-section for direct electron collision from the helium ion ground state to the upper level of 4686 $\mathring{A}$(n=4), we find that for an ion number density of $10^{13} cm^{-3}$, and an electron number densities with energies greater than 75 and 50 eV of

10^{10} and 10^{11} cm^{-3} respectively (see Chapter VI § 6.4) and at 1 Torr the excitation rates for direct electron excitation from the helium ground state and from the ion ground state are 2×10^{15} and 3×10^{14} cm^{-3} sec^{-1} respectively. Hence we can say that direct electron excitation from the neutral ground state is dominant. This conclusion has been reported by many workers[98-100]. It agrees with the experimental results, since excitation from the ion ground state or the (2^3S) state would lead to a super linear dependence of 4686 Å emission on the current, since both the number densities of ions and (2^3S) increases linearly with current.

5.5 The effect of the cathode surface conditioning on the excitation in the negative glow

The excitation in the negative glow depends on, among other things, the electron number density. The electron density in the negative glow has a component originating in the dark space. The flux of these electrons to the negative glow affect the excitation in that region. This effect will be studied by studying the effect of heating the cathode surface by the discharge current and by applying a transverse magnetic field relative to the cathode electric field.

5.5.1 The effect of cathode heating on the excitation of 3889 Å

We have seen before (§ 2.2) that if the discharge was initially operated under high current conditions (> 150 mA), then on reducing the current the cathode fall in potential did not stabilize immediately but monotonically increased or decreased over periods of the order of 10-15 minutes before reaching its original stable value. Using this property it was possible to heat the cathode surface using the discharge current. While the cathode fall potential was decreasing to its original stable value, the spontaneous emission as a function of the cathode fall potential was monitored. The result can be seen in figure (5.4). It is evident from the figure that the emission of 3889 Å decreases as the cathode fall potential increases. The same effect was observed when the triplet metastable density were monitored (see figure 5.4 and Appendix II).

5.5.2 The effect of transverse magnetic field on 3889 Å emission

This effect was studied by applying an axial magnetic field, variable between

0 and 600 G. With this geometry, the magnetic field is everywhere perpendicular to the electric field. The cathode fall potential decreases with increasing magnetic field at all pressures (fig 5.5a). It was found that the cathode fall potential decreased by increasing the magnetic field to about 600 G.

As the magnetic field increased from 0 to 300 G to 600 G the radial profile of the emission at 3889 Å was monitored. It is clear that as the magnetic field increases, the emission of 3889 Å increases. The increase is over all of the radial profile (see figure 5.5b). This effect is consistent with the previously observed dependence of emission on cathode fall potential when current and pressure are kept constant. The decrease of the cathode fall potential and the increase in the emission seem to apply to many species in the hollow cathode discharge[77] and it may be that it is a fundamental feature of the hollow cathode.

It is interesting to compare the above effect with that of introducing Cd into the discharge. The magnetic field decreases the cathode fall potential which results in an increase in the emission of 3889 Å. It was observed that introducing Cd to the discharge (see Chapter II) increases the cathode fall potential and that leads to a decrease in the emission at 3889 Å. This suggests that the magnetic field and the introduction of the Cd affect the emission at 3889 Å through their effect on the cathode fall.

5.6 The emission of 4416 Å and 5378 Å

We have examined two transitions of Cd II, one at 4416 Å, the other at 5378 Å. The excitation mechanism of the former has been suggested as being predominant through Penning excitation[1] while that of the latter through Duffendack excitation[6].

At constant current and pressure, the emission intensity at 4416 Å as a function of the Cd partial pressure reaches a maximum value at an oven temperature of 290°C and then it decreases for any further oven temperature increase (see figure 5.6a).

At constant current and oven temperature the emission at 4416 Å and 5378 Å at the tube centre behaves in a similar way with pressure as the metastable

number density and the ion number density (figure 5.6b). This shows the strongrelation between the emission at 4416 Å and 5378 Å and the metastable and ion (or electron) number densities.

The radial profiles of the above two transitions can be seen in figure (5.7). These radial profiles are similar to those of the He I and He II transitions, for all values of helium pressures and oven temperatures in the range of 270 - 350°C. The dip in the discharge occurs at helium pressure higher than 12 Torr, which suggests that its appearance is due to the geometry of the discharge. However, the dip depth is smaller for the cadmium transitions than that for the helium I and II transitions.

5.7 The general features of the emission in the negative glow

From the aforementioned study we can conclude the following:

1] The emission of He I and He II transitions increases linearly with the discharge current and decreases monotonically with helium pressure.

2] At low pressures the radial profiles of He I and He II transitions reach a maximum at tube centre. As the pressure is increased the negative glow moves towards the tube walls and the radial profiles reveal two separated maxima. The ionic transitions show proportionally greater emission towards the negative glow edge than the neutral transitions.

3] The radial profiles of the Cd ion transitions at 4416 Å and 5378 Å show similar behaviour with pressure to that shown by the He transitions.

4] The effect of conditioning the cathode surface may lead to increase or decrease in emission at 3889 Å according to circumstances. The correlation between changes in the cathode fall potential and excitation at 3889 Å was observed by heating the cathode surface, by increasing the magnetic field and by the introduction of Cd.

5] One of the most important features of the negative glow at high pressures ($p \geq 12$ Torr) is the persistant appearance of the dip. These conclusions will be used in Chapter VI section § 6.6, when the excitation mechanisms in the hollow cathode will be discussed.

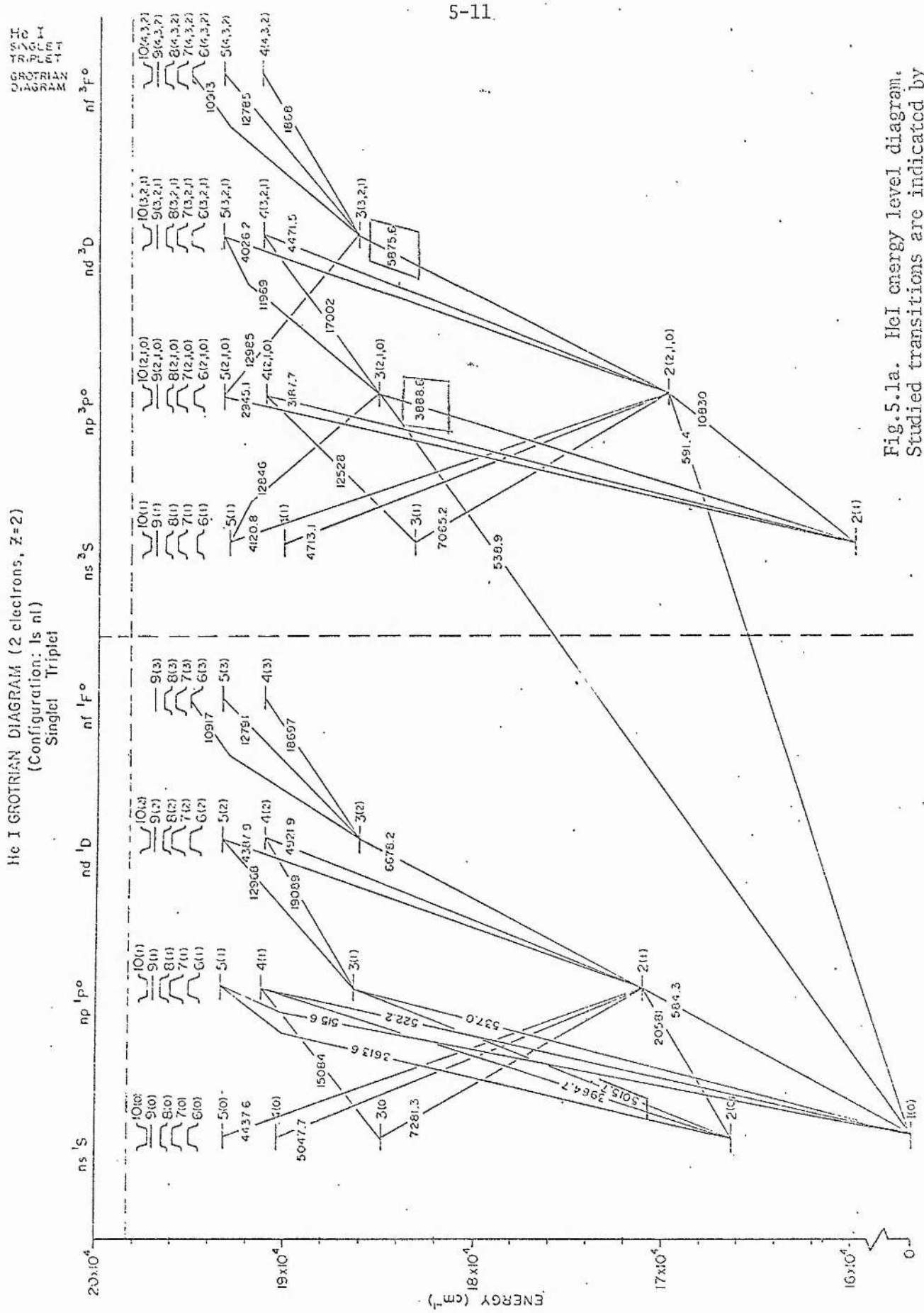

Fig.5.1a. HeI energy level diagram. Studied transitions are indicated by boxes.

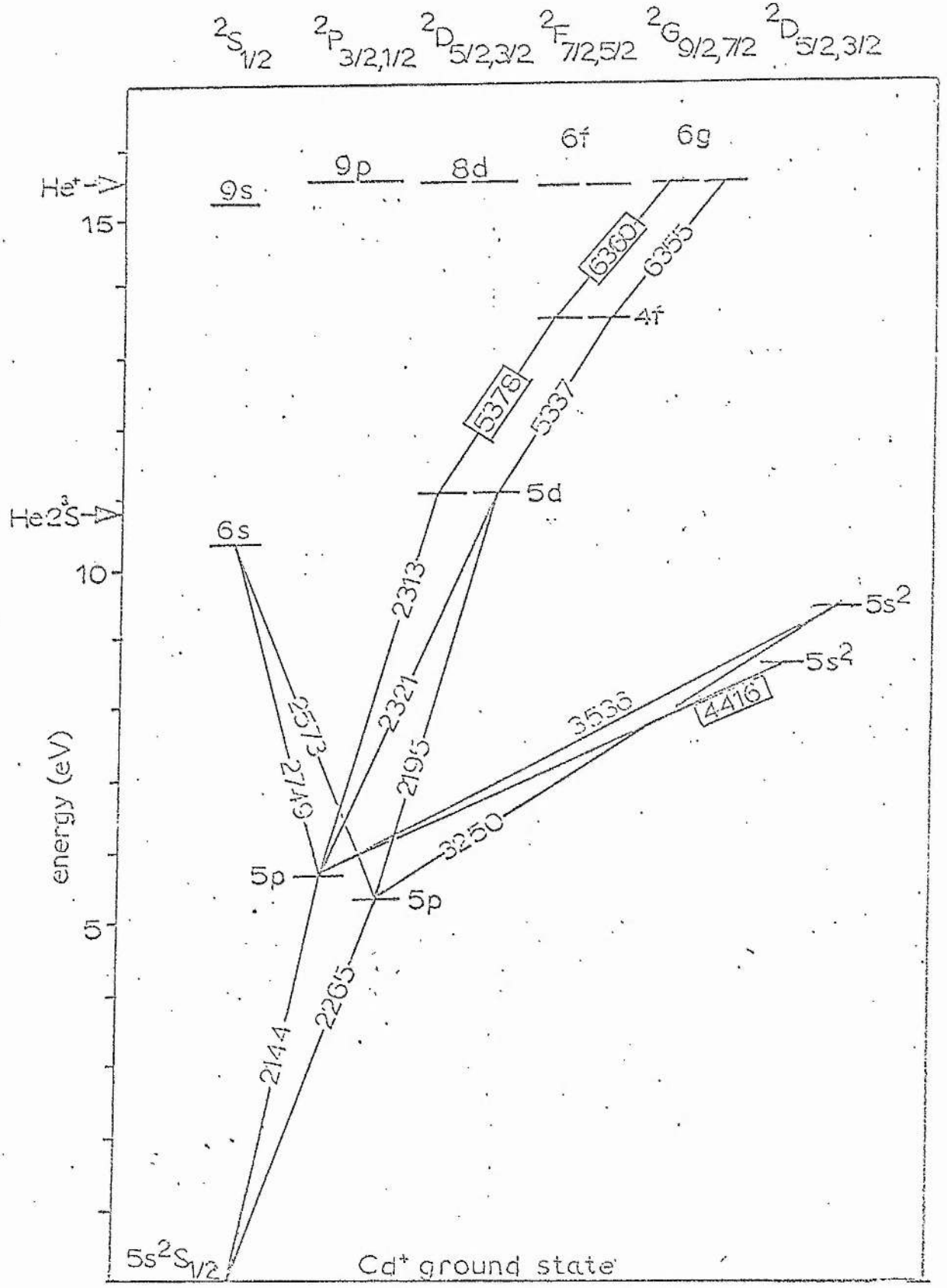

Fig.5.1b. Energy levels of the cadmium ion. Wavelengths are in Å. Studied transitions are indicated by boxes.

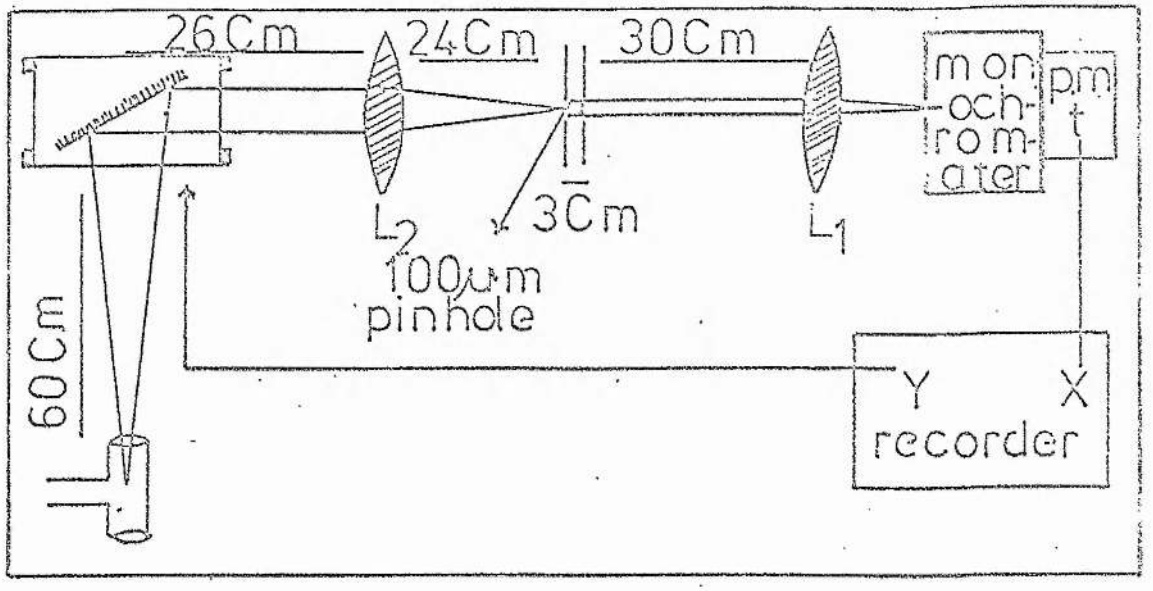

Figure 5.1c, The optical arrangement.

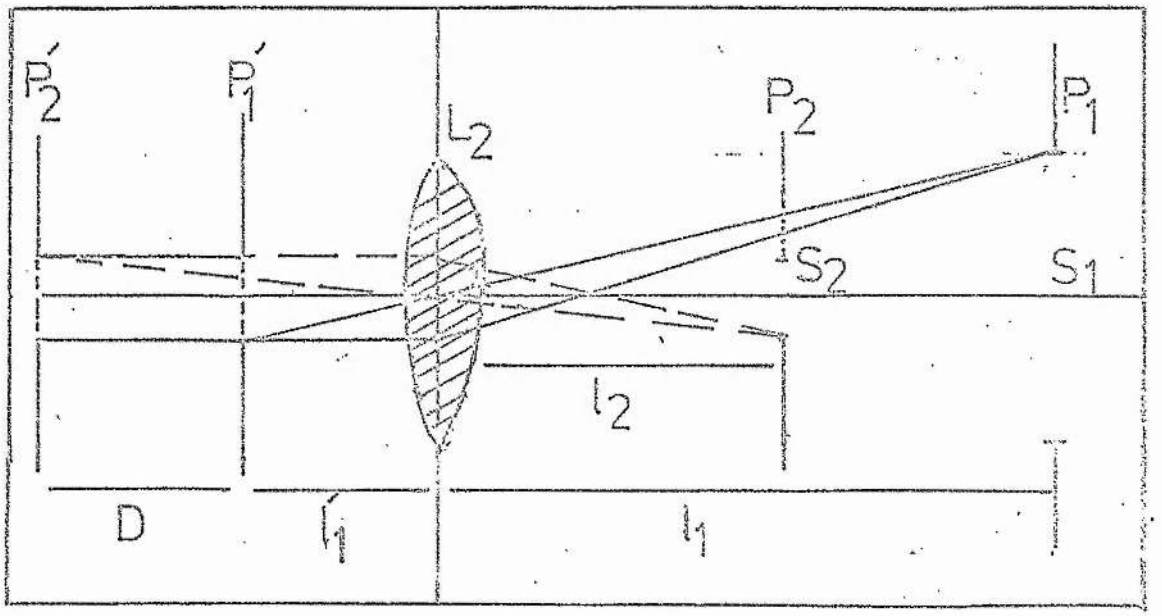

Figure 5.1d The pinholes S_1, S_2 in their planes P_1, P_2 and their images in the planes P_1', P_2' inside the discharge.

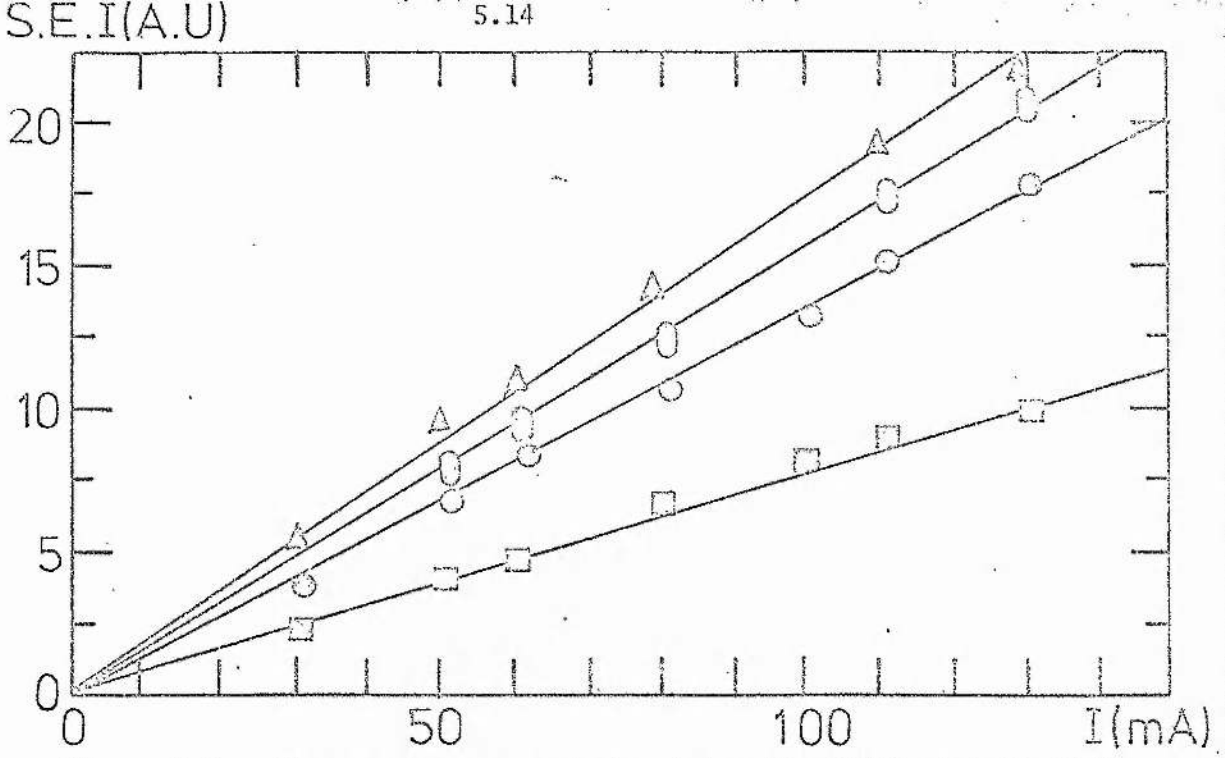

Figure 5.2a. The spontaneous emission intensity (SEI) at a pressure of 1 Torr and different discharge currents for different He I and He II transitions: Δ 5876 Å, ⬯ 5016 Å, ○ 3889 Å and □ 4686 Å.

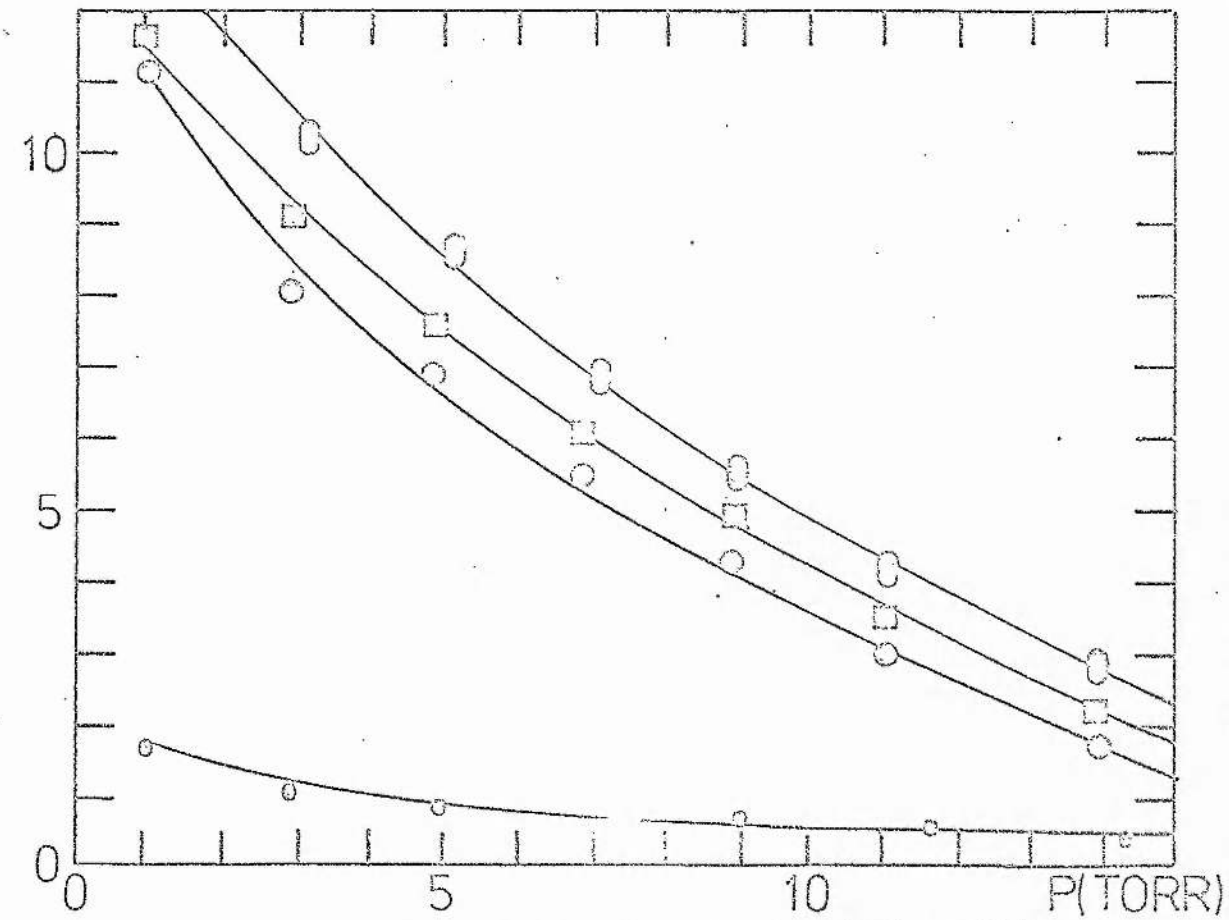

Figure 5.2b. The spontaneous emission intensity (SEI) at discharge current of 100 mA and different pressures for different He I and He II transitions: ⬯ 5876 Å, □ 5016 Å, ○ 3889 Å and ○ 4686 Å.

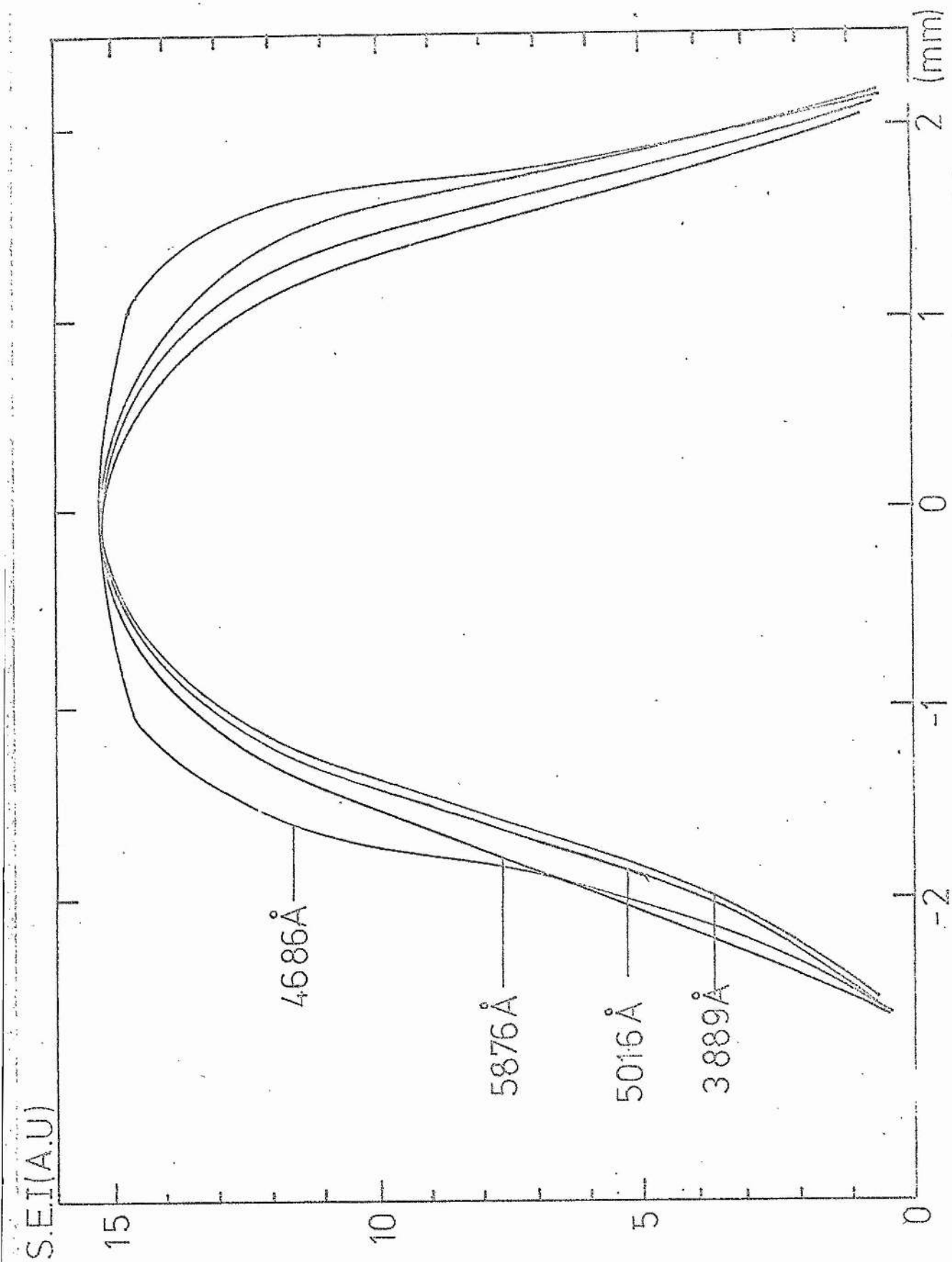

Figure 5.3a. The radial profiles at 100 mA and 8.5 Torr for different He I and He II transitions.

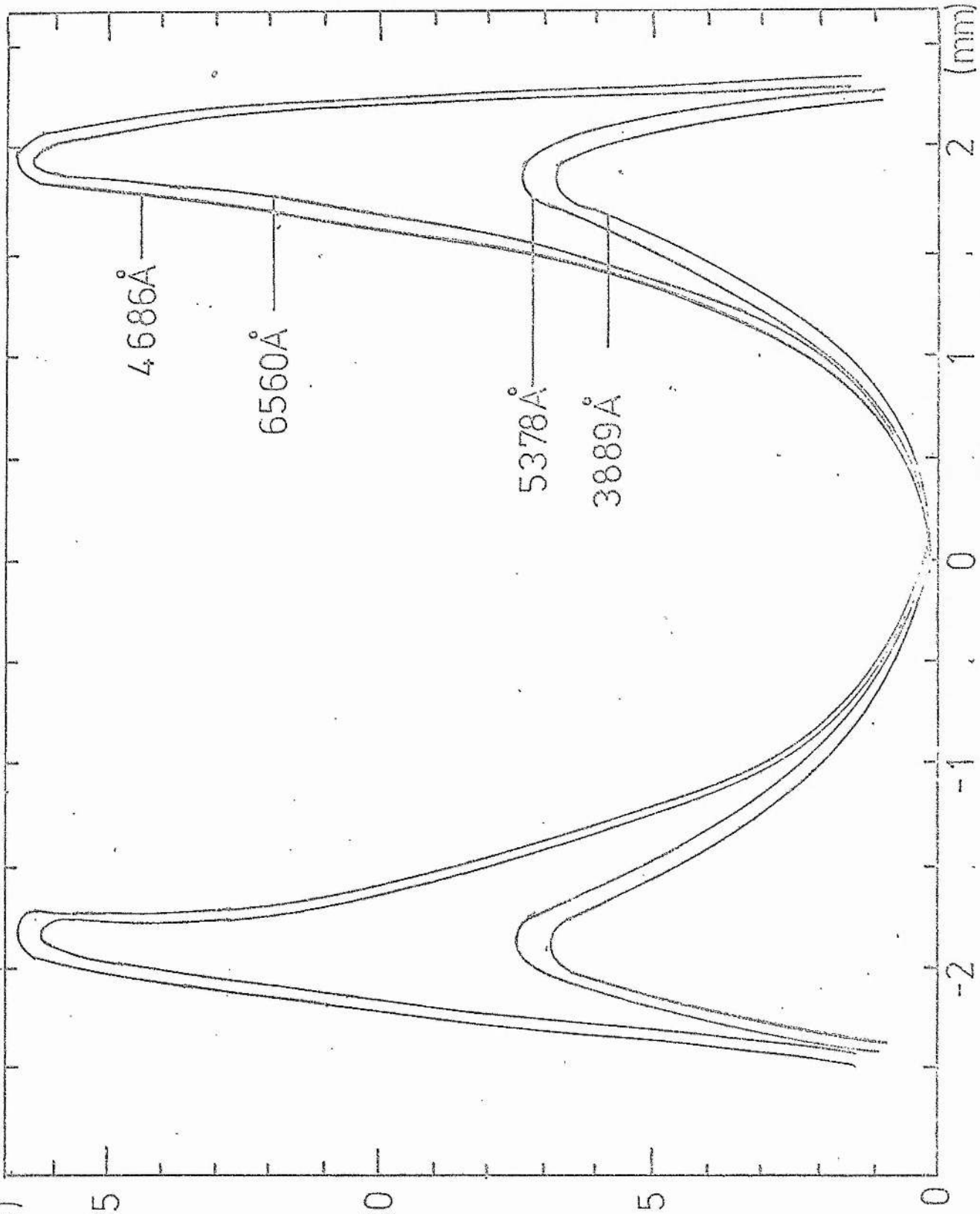

Figure 5.3b. The radial profile at 100 mA and 19.5 Torr for different He I and He II transitions.

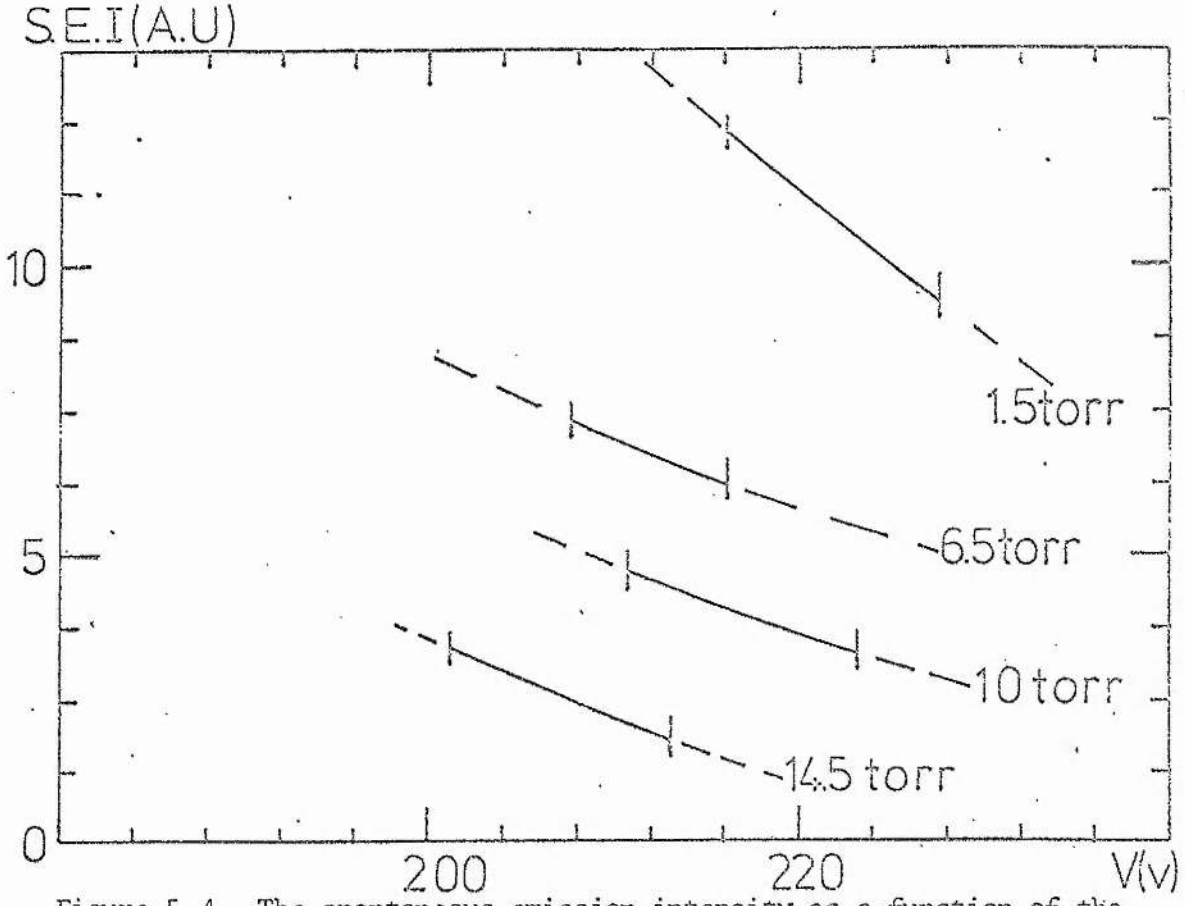

Figure 5.4. The spontaneous emission intensity as a function of the cathode fall potential. The dashed parts of the curves refer to unstable regions of the cathode fall potential, and the solid curves refer to the stable regions.

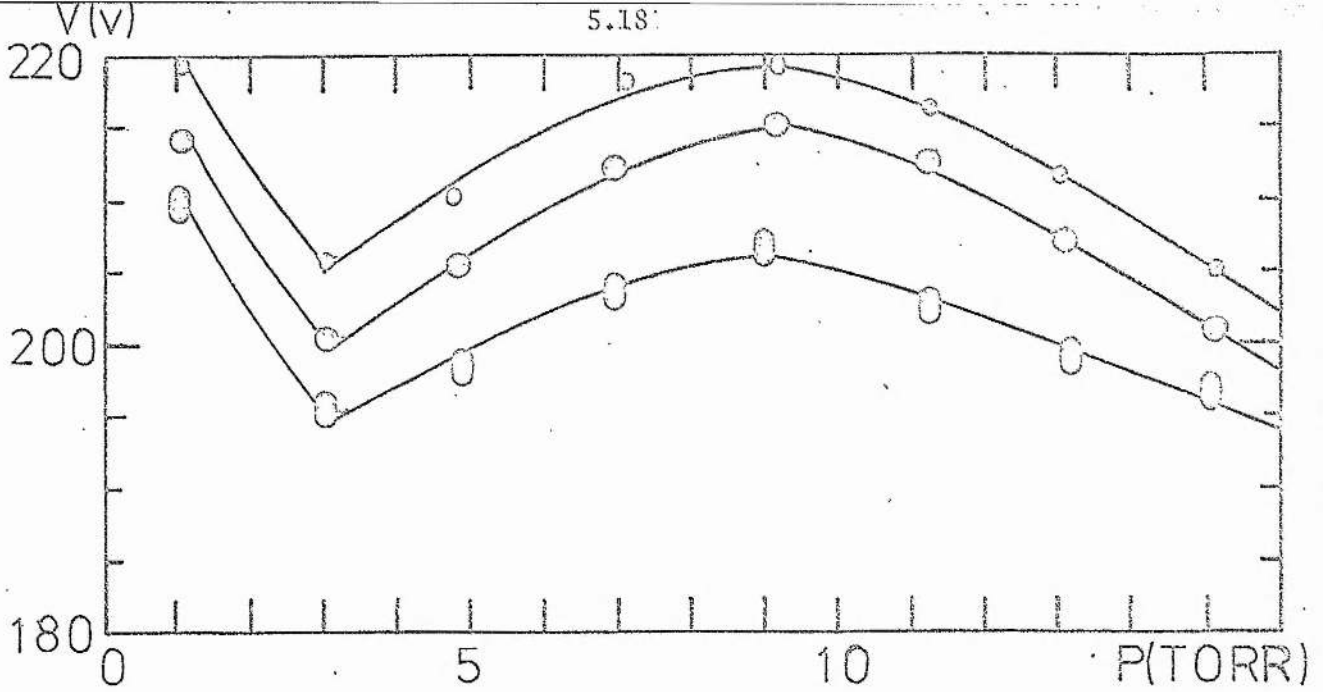

Figure 5.5a. The cathode fall potential as a function of the pressure and constant current of 100 mA for different values of the magnetic field, ⊙ 0 G, ⊙ 300 G and ⊙ 600 G.

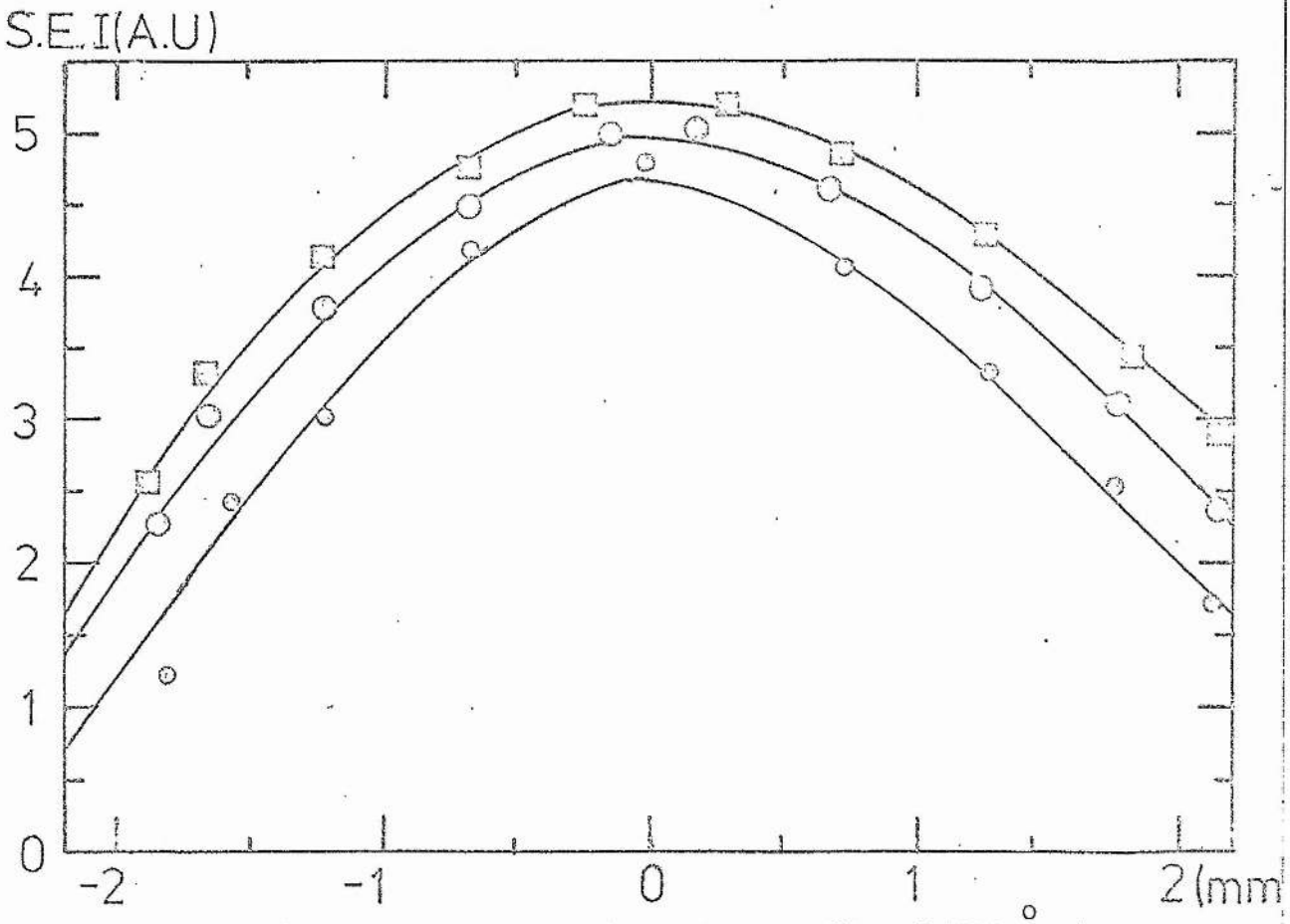

Figure 5.5b. The spontaneous emission radial profile of 3889 Å at 2 Torr and 100 mA for different values of the magnetic field, ⊙ 0 G, ⊙ 300 G and ⊡ 600 G.

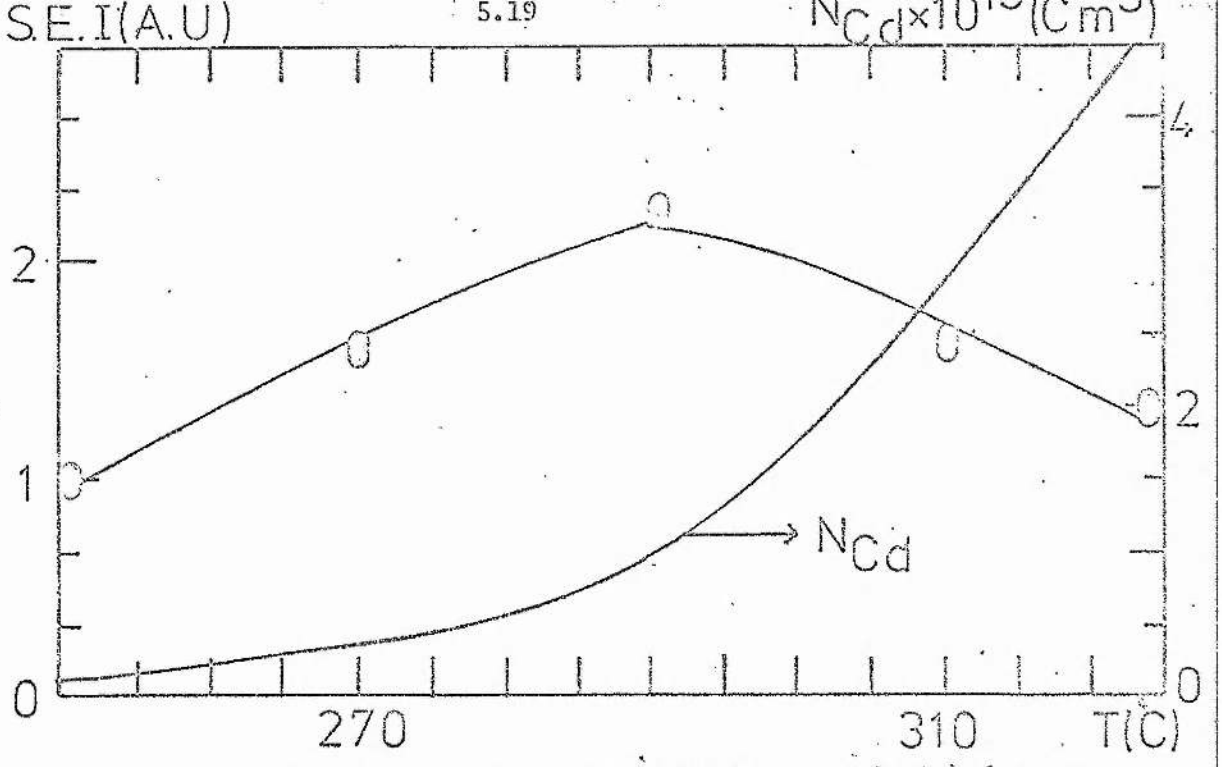

Figure 5.6a. The spontaneous emission of 4416 at 100 mA and helium pressure of 1 Torr as a function of the oven temperature.

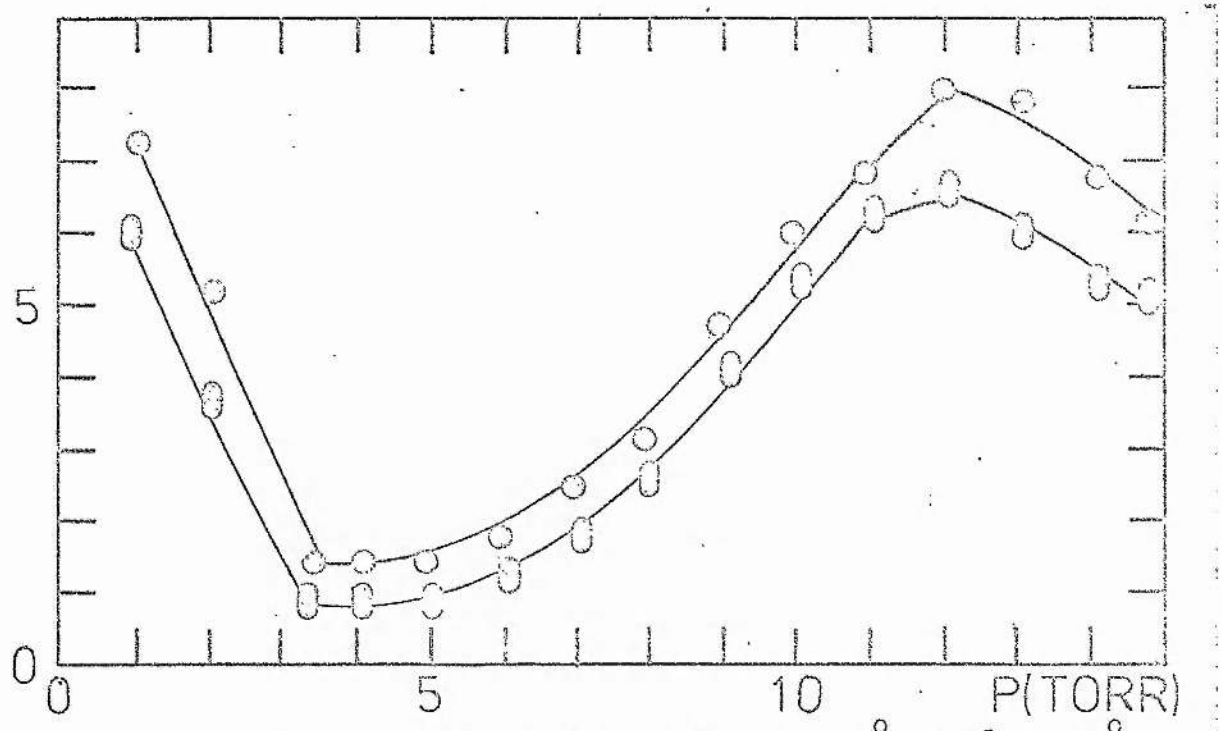

Figure 5.6b. The spontaneous emission of ○ 4416 Å and ○ 5378 Å as a function of the discharge pressure and at a constant current of 100 mA and a cadmium oven temperature of 310°C.

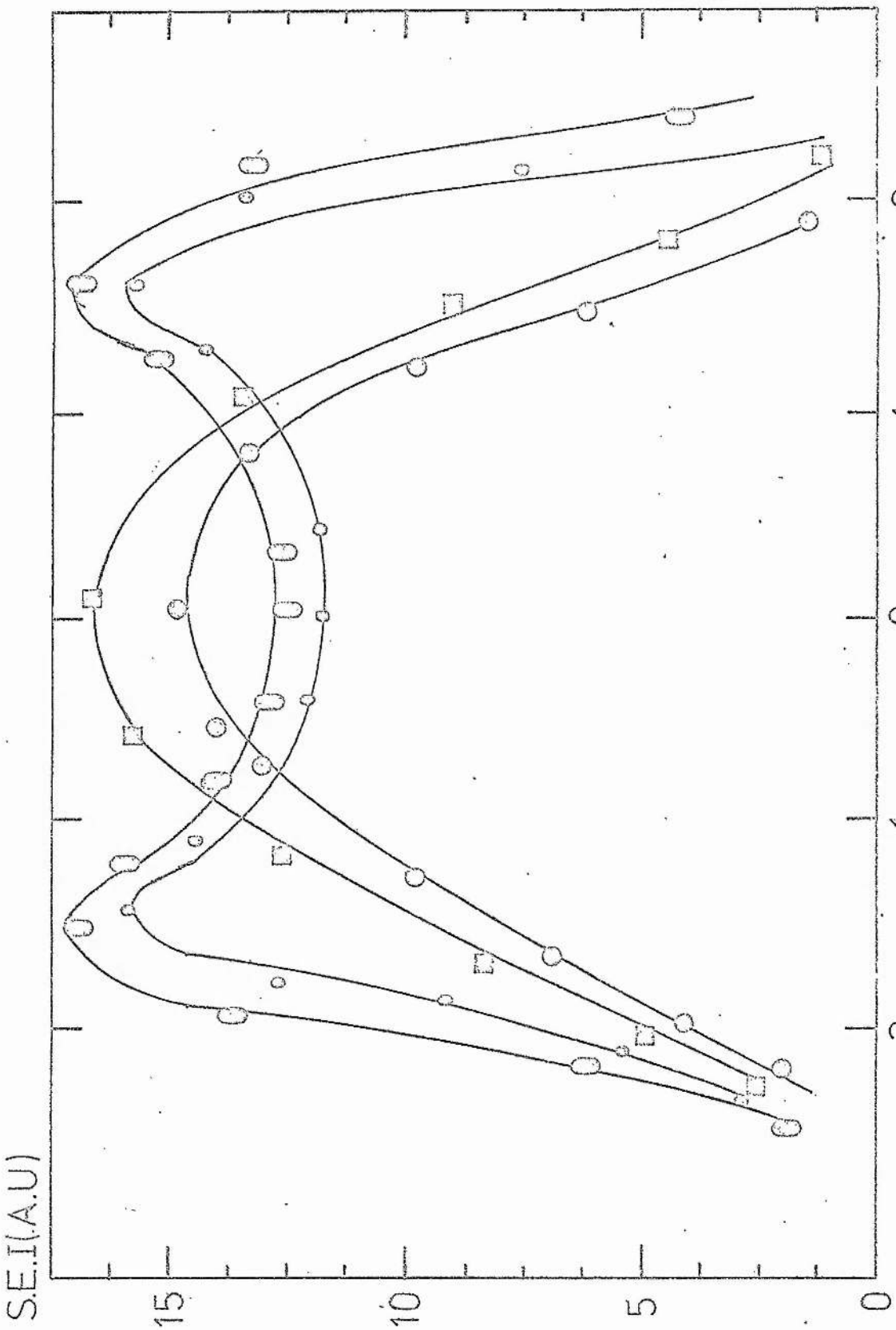

Figure 5.7. The radial profiles of 4416 Å and 5378 Å at constant current of 100 mA, oven temperature of 310°C and for different helium pressures.
□ 4416 Å at 1 Torr, ○ 4416 Å at 18 Torr, ○ 5378 Å at 1 Torr and ○ 5378 Å at 18 Torr.

CHAPTER VI

MECHANISMS OF THE HOLLOW CATHODE DISCHARGE AND THE SPECIES RATE EQUATIONS

6.1 Introduction

In this chapter we discuss the observed behaviour of the number densities of the various particles studied (ions, electrons, metastables, excited states) in relation to the basic mechanisms taking place in a hollow-cathode. The approach is to draw up rate equations describing the steady state number densities, and to evaluate the various parameters in these equations using a model of the hollow cathode discharge. The implications of the observed behaviour and the model into which they fit will then be considered in relation to the hollow cathode as a laser medium.

First of all we summarize the principle experimental findings of the previous chapters.

(1) As the discharge current increases, triplet metastable, electron (or ion) and excited state (neutral or ionic) number densities increase linearly with current (see figures A2.2a, 3.4a, 4.10, and 5.2a). On the other hand the cathode fall potential, the negative glow length, the gas temperature and the singlet metastable number density saturate with increasing current (see figures 2.1a, 2.4b, 2.8a, and A2.1b).

(2) As the discharge pressure increases, the cathode fall potential (see figure 2.1b) behaves distinctively (decreases to a minimum (203 V) at low pressures (3 Torr), then increases with increasing pressure to a maximum (220 V) at 9 Torr, then decreases for further pressure increase) and is followed in this behaviour by the triplet metastable and electron (or ion) number densities (see figures A2.2b, 3.4b and 4.10b). On the other hand the gas temperature, the negative glow length and the singlet metastable number density saturate with increasing pressure (see figures 2.8b, 2.4a and A2.1a). Densities of excited neutral and ionic states decrease monotonically as the pressure increases (see figure 5.2b).

(3) As a function of the cathode fall potential, with both pressure and discharge current constant, the triplet metastable number density and the emission at 3889 Å behave similarly in increasing as the cathode fall potential decreases (see figures A2.3 and 5.4).

(4) The radial profiles of the singlet, triplet and excited states

emission reach a maximum value at the tube centre at low pressures and a minimum at high pressures (see figures A2.4a, A2.4b, 5.3a and 5.3b). The radial profiles of the ionic transitions rise sharply at the edge of the negative glow compared to those of the excited neutral states (see figures 5.3a,b).

6.2 The mechanisms of the hollow cathode discharge

We now consider the basic mechanisms taking place in a hollow cathode discharge, and examine how they differ from those in a conventional cold cathode discharge. In particular we are concerned with how the mechanisms taking place in the dark space affect the negative glow. On the basis of this study we will then be able to draw up the rate equations which in turn determine the populations of the states.

The basic function of the cathode region is to facilitate the transfer of the current from the external electrical circuit into the discharge. This can be brought about by positively charged particles (ions) moving to the cathode surface where they are neutralized or by electrons being ejected from the cathode surface. The latter process requires an energy source to overcome the work function of the surface. In the case of the cold cathode this is achieved through secondary emission processes due to the bombardment of the surface by ions, photons, metastables, etc. The relative contributions to the current at the cathode surface of the above processes depends upon the relative particle fluxes and their secondary coefficients.

The ion flux per unit area per second to the cathode surface is $N_{ic} V_{id}$ where N_{ic} and V_{id} are the ion number density and drift velocity at the cathode surface. Therefore the electron current density at the cathode surface due to the ions is $\gamma_1 e N_{ic} V_{id}$, where γ_1 is the secondary emission coefficient for the ions.

The flux of photons to the cathode surface per unit area per second depends on the excitation in the discharge. If we assume that N_{ed}, V_{ed} and N_e and V_e are the electron number density and velocity in the cathode dark space and the negative glow regions respectively then the fluxes from each region to the cathode surface per unit area per second and consequently the contribution of the photons to the electron current at the surface is

$$N_a N_{ed} f_d < \sigma V_{ed} > \frac{d}{2} \gamma_2 \text{ and } N_a N_e f_g < \sigma V_e > G \gamma_2 .$$

In the above f_d and f_g are the fraction of photons which arrive at the cathode surface from the dark space or the negative glow respectively, σ is the excitation cross-section, d is the width of the dark space and G is a geometrical factor which is equal to $(\frac{R^2 - R'^2}{2R})$ where R and R' are the radii of the discharge tube and the negative glow respectively and γ_2 is the secondary emission coefficient for the photons.

Similarly the flux per unit area per unit time and consequently the contribution of the metastables to the electron current at the cathode surface is $(\frac{GM_1}{\tau_1} + \frac{GM_3}{\tau_3}) \gamma_3$ where M_1 and M_3 are the singlet and triplet metastable number densities respectively in the negative glow and γ_3 is the secondary emission coefficient for the metastables.

The ratio of the electron current density J_{-s} to that of the ions J_{+s} at the cathode surface is given by the relation

$$\frac{J_{-s}}{J_{+s}} = \frac{N_{ic} V_{id} e \gamma_1 + [N_a N_e f_g <\sigma V_{eg}> G + N_a N_{ed} f_d <\sigma V_{ed}> \frac{d}{2}] \gamma_2 e + (\frac{GM_1}{\tau_1} + \frac{GM_3}{\tau_3}) \gamma_3 e}{N_{ic} V_{id} e} \qquad (6.2.1)$$

Equation (6.2.1) suggests that since $\gamma_1 << \gamma_2 < 0.1$[12,16] and since the flux of the metastables is less than the flux of the ions to the cathode surface then the ions carry the greater part of the current at the cathode surface.

The individual effects of ions, photons (from the dark space and the negative glow) and metastables now will be estimated, so the ratio of electron to ion currents at the cathode surface can be estimated.

The secondary emission due to the ion bombardment depends on the ion flux and the secondary emission coefficient γ_1 (see equation 6.2.1) which in turn depends on the energy of the bombarding ions. The ion energy at the cathode surface is not known precisely, but it is estimated to range between 10 to 50% of the cathode fall potential or 20 to 100 eV in our case (an ion velocity of 2.2×10^6 to 7×10^6cm sec^{-1}). This gives γ_1 a value in the range of 0.05[16]. For an ion density of 10^{12}cm^{-3}[12], $N_{ic}\, V_{id}\, e\, \gamma_1$ does not exceed 5×10^{-2} A cm^{-2}.

The secondary emission due to the photons from the dark space or the negative glow depends on the number of photons from each region and on γ_2, which is a function of the wavelength[16]. Most of the excitation in the dark space leads to the emission of UV and vacuum UV radiation (such as the 584 Å(HeI $2p^1P$-$1s^1S$) transition, that is why the dark space is dark) while most of the excitation in the negative glow emits visible radiation. Hence γ_2 varies between 0.1 for photons from the dark space and 10^{-3} for photons from the negative glow respectively[16]. For an electron number density in the dark space of 5×10^{10}cm^{-3} (in the dark space $N_e << N_i$), an electron number density in the negative glow of 5.5×10^{11} (see table 6.1) and electron velocities of 8.4×10^8 and 2.96×10^8cm sec^{-1} respectively we find (assuming $f_g = f_d = 1$[12]) that for a discharge tube of 6 mm diameter and dark space width of 0.1 mm that the effect of photons from the dark space and the negative glow are 2.4×10^{-3} and 2.7×10^{-3} A cm^{-3} respectively. The effect of the metastables, assuming that γ_2 equals γ_3 and a diffusion time of 1.9×10^{-4}sec (see table 6.1), does not exceed 5×10^{-5} A cm^{-2}.

From the above we can see that the effect of ions is dominant (J_{-s}/J_{+s} is about 0.05). However the effect of the photons from the dark space and the negative glow are very important. It must be emphasised that the above conclusion is purely an estimate and there are no experimental results to verify it.

As a result of the positive ion, photon and metastable bombardment of the cathode, new electrons are released. Electrons leaving the cathode surface are accelerated across the dark space. They excite and ionize the gas which results in multiplication of their number by a factor M'. Suppose that for each electron formed in the gas there are ultimately γ_{123} electrons formed at the surface as a result of the various processes. Then for the discharge to be self-sustained the following condition must be satisfied[13]

$$\gamma_{123} (M' - 1) = 1. \qquad (6.2.2)$$

As a result of the multiplication a large number of ion-electron pairs are created. However, because of the large mobility of the electrons their flux from a certain point in the cathode dark space is initially larger than that of the ions. This leads to the accumulation of a large positive ion space charge which leads to the creation of the large field in that region. If the generation of the positive ions is uniform across the dark space region then this leads to a linear electric field[12]. The above discussion shows the relation between the multiplication processes in the cathode dark space, the processes at the cathode surface and the cathode fall potential. (It should be noted that in a normal cathode equation (6.2.2) holds but in this case, only ion bombardment is important.) The form of this relation can be deduced as follows. Assume that each electron forms α ion pairs per unit length of the dark space, then the total number of ions created across d (the multiplication M') is[16]

$$\exp \left(\int_0^d \alpha \, dx\right). \qquad (6.2.3)$$

Defining η', the number of ion pairs formed per electron per volt potential, then we have $\int_0^d \alpha \, dx = \eta' V$.

From equations (6.2.2) and (6.2.3) we can see that

$$V = \frac{1}{\eta'} \ln \left(1 + \frac{1}{\gamma_{123}}\right) \qquad (6.2.4)$$

This equation shows that as the secondary emission at the cathode surface increases the cathode fall potential decreases slowly. From here we can see one of the basic differences between the hollow cathode discharge and a normal cathode. In a hollow cathode, as well as secondary emission due to ion bombardment contributing to the release of electrons, other processes such as photo-emission play a role as well. Consequently γ_{123} is larger and so a smaller cathode fall potential is required to sustain the discharge.

The electric field (created as a result of the accumulation of the positive ion space charge) transfers the ions to the cathode surface so that a current flows. This field decreases linearly as the distance from the cathode surface increases. By applying Poisson's equation, and remembering that the ion number density in the dark space is larger than the electron number density, then it can be shown that the ion current density at the surface is related to the cathode fall potential V, the width of the cathode region d and the ion drift velocity at the cathode surface V_{ic} by the relation

$$J_{+s} = \frac{V_{ic}}{2\pi} \frac{V}{d^2}. \qquad (6.2.5)$$

The electron current density at the cathode surface as a result of the various processes is expressed in equation (6.2.1) and can be written as the sum of four currents which result from the bombardment of ions, photons from the dark space, photons from the negative glow, and metastables as

$$J_{-s} = \gamma_1 J_{+s} + D J_{-s} + G' J_{-g} + G'' J_{-g} \qquad (6.2.6)$$

where J_{+s} is the ion current at the cathode surface, J_{-s} and J_{-g} are the electron currents at the cathode surface and in the negative glow respectively and D, G' and G'' are $\gamma_2 f_d n_d$, $\gamma_2 f_g n_g$ and $\gamma_3 (M_1 + M_3)$ respectively where n_d and n_g are the number of photons bombarding the cathode surface from the dark space and the negative glow respectively.

Assuming that in the negative glow J_{-g} is equal to J and remembering that $(J_{-s} + J_{+s})$ is equal to J at any point in the discharge, then with some algebraic manipulation

$$\frac{J_{+s}}{J} = \frac{1 - D - G' - G''}{1 + \gamma_1 - D} \qquad (6.2.7)$$

From equations (6.2.5) and (6.2.7) we get

$$\frac{J}{p^2} = \frac{V_{ic}}{2\pi} \frac{V}{(Pd)^2} \frac{1 - D - G' - G''}{1 + \gamma_1 - D} \qquad (6.2.8)$$

This equation shows directly that the total current density depends on V_{ic}, (Pd) and the various emission processes at the cathode surface.

It is known that when in equilibrium with a uniform electric field positive ions have a drift velocity which is proportional to the electric field or to its half power, depending on its magnitude. However, in the dark space of a hollow cathode discharge there are doubts about the equilibrium because of the high magnitude of the field. Hence it is necessary to look for a relation between V_{ic} and the cathode fall region parameters by other considerations. This can be done by considering the charge transfer in the cathode dark space region. The existence of this process is indicated by the ion energy at the cathode surface. If the charge transfer mean free path at unit pressure is λ_{+o} then the potential V' at a point λ_{+o} from the cathode is[12]

$$V' = V \left[\frac{2\lambda_{+o}}{Pd} - \left(\frac{\lambda_{+o}}{Pd}\right)^2 \right] \qquad (6.2.9)$$

The energy of the ions arriving at the cathode is equal to eV', and hence we obtain

$$V_{ic} = \left\{ \frac{4\ eV}{M} \left[\frac{2\lambda_{+o}}{Pd} - \left(\frac{\lambda_{+o}}{Pd}\right)^2 \right] \right\}^{\frac{1}{2}} \qquad (6.2.10)$$

where M is the ion mass. If we insert equation (6.2.10) in equation (6.2.8) we get $\left(\frac{J}{p^2}\right)$ as a function of $V^{\frac{3}{2}}$ and $(Pd)^{\frac{5}{2}}$ respectively. Furthermore we can see also the difference between a hollow cathode and a normal cathode where the effect of the photons and the metastables are

negligible.

We have seen before that the discharge is self-sustaining if equation (6.2.2) is satisfied. It can be shown that this equation can be expressed in terms of the secondary emission processes at the surface by the relation[12]

$$(\gamma_1 + \gamma_2 f_d + \gamma_2 f_g + \gamma_3)\, b'\, \eta'\, V \exp\left(\alpha d \left(1 - \left(\frac{V'_e}{V}\right)^{\frac{1}{2}}\right)\right) = 1 \qquad (6.2.11)$$

where b' is the fraction of electrons which have energy higher than the ionization energy and V'_e is the electron energy in the dark space. Equation (6.2.11) can be used to deduce the width of the cathode fall region (Pd) which is

$$Pd = \frac{1}{(\alpha/P)\left(1 - \left(V_e/V\right)^{\frac{1}{2}}\right)} \ln\left[\frac{1}{(\gamma_1 + \gamma_2 fd + \gamma_2 fg + \gamma_3)\, b'\, \eta'\, V}\right] \qquad (6.2.12)$$

Here again we can see that the width of the cathode dark space is also determined by the multiplication in that region and by the various processes at the cathode surface.

As the electrons move across the cathode dark space, their number density becomes larger as a result of multiplication and so they dominate the current at the edge of the dark space. This leads to a decrease in the electric field intensity which defines the boundaries of the negative glow.

Farther from the cathode surface, though the electric field becomes weaker, the electrons are more energetic and their ability for ionization is stronger. However, the thickness of the cathode dark space d, is small compared to the discharge bore, so the energetic electrons make only a few collisions losing a small fraction of their energy in that region. This results in a large number of electrons entering the negative glow from the dark space with energy well above the excitation or the ionization energy of the helium or the metal atoms. Since the energy of these electrons is high, then they are largely responsible for the excitation to metastables or excited or ionizing levels. Hence they are a determining factor in the creation processes leading to the population of (2^1S), (2^3S), ions or the

excited states levels. This can be shown clearly by writing the rate equations of the different species particles.

6.3 The general species rate equations

The behaviour of each particular species is coupled directly to the discharge parameters by the rate equations. In the following we shall assume that N_{eg}, N_{eh}, M_1, M_3, N_a and N_3 are the number densities of cool electrons ($E_e \leq 19$ eV), hot electrons ($E_e > 19$ eV, this means that this group includes the beam electrons) singlet metastables, triplet metastables, helium atoms, and the upper level of 3889 Å ($3p\ ^3P_o$) respectively. All these number densities refer to the negative glow. From the point of view of the rat equations we shall assume that the electron energy distribution can be replaced by two groups of electrons; cool and hot as defined above. The hot electrons are responsible for the excitation and ionization processes, while the cool electrons are responsible for de-excitation processes. This will be discussed further in § 6.4.

The processes which determine the ion (electron) number density are: ionization by electrons, ionization by collisions between two metastable (mainly triplet-triplet, since $\frac{2^3S}{2^1S}$ is about 4 and since the rate coefficients for these reactions are comparable[67], then the $2^1S - 2^1S$ reaction is small in comparison to $2^3S - 2^3S$ reaction, so it will be ignored) diffusion, recombination (three body recombination, two electrons and an ion as we have shown in Chapter IV). Hence the ion (electron) rate equation can be written as follows

$$\alpha_1' N_{eh} N_a + \alpha_2 M_3^2 - \frac{N_{eg}}{\tau_e} - \alpha_3 N_{eg}^3 = 0 \qquad (6.3.1)$$

where α_1', α_2, α_3 and τ_e are the rate coefficients and the diffusion time respectively.

The processes which determine the singlet metastable number density are: direct excitation from the ground state, conversion from (2^3S),

cascade from above, diffusion, ionization, de-excitation to (1^1S), de-excitation to (2^3S), excitation to the higher levels and collision with one or two helium atoms. However it was found that de-excitation to the ground state is negligible[16,78-81] compared to ionization or conversion to (2^3S). Further collision between (2^1S) and one or two helium atoms is also negligible[82]. Hence the (2^1S) rate equation is

$$\beta_1 N_{eh} N_a + \beta_2 M_3 N_{eg} + \beta_3 N_a N_{eh} - [\frac{1}{\tau_1} + (\beta_4 + \beta_5 + \beta_6) N_{eg}] M_1 = 0 \qquad (6.3.2)$$

where β_1, β_2, β_3, β_4, β_5, β_6 and τ_1 are the rate coefficients and the diffusion time of (2^1S).

Similarly the rate equation of (2^3S) can be written as follows:

$$\gamma_1' N_{eh} N_a + \beta_6 M_1 N_{eg} + \gamma_2' N_a N_{eh} - [\frac{1}{\tau_3} + (\gamma_3' + \gamma_4 + \beta_2) N_{eg}] M_3 - \alpha_2 M_3^2 = 0 \qquad (6.3.3)$$

where γ_1', γ_2', γ_3', γ_3 and τ_3 are the rate coefficients and the diffusion time for (2^3S).

The processes which determine the population of the upper level ($3p\ ^3P$) of the 3889 $\mathring{A}$ transition are: direct excitation from the ground state, excitation from (2^3S), diffusion, radiative decay, ionization, de-excitation to (1^1S) and conversion to (2^3S). Here again the de-excitation to (1^1S) is at least one order of magnitude smaller than ionization[16,79,83], so it can be neglected and the rate equation can be written as

$$\gamma_1' N_a N_{eh} + \gamma_4 M_3 N_{eg} - [\frac{1}{\tau_4} + A + (\delta_1 + \delta_2) N_{eg}] N_3 = 0 \qquad (6.3.4)$$

where δ_1, δ_2 and τ_4 the rate coefficients and the diffusion time for N_3 respectively and A is the Einstein A-coefficient.

The above equations describe N_{eg}, N_{eh}, M_1, M_3 and N_3. These are four equations with five unknowns. The solution of these equations cannot be found unless N_{eh} is calculated (by considering the flux of electrons from

the dark space and by considering also all the de-excitation processes in the discharge) or by knowing the ratio N_{eh}/N_{eg}. However, even if this is theoretically possible, because of the lack of information about the various coefficients a systematic study of the particle densities is not possible. Nevertheless this study can be simplified further if we remember that the effect of the upper levels are small since their number densities are expected to be not more than 30%[7] of M_1 or M_3. Further, if we look at the measured parameters we find that at a constant current and in the pressure range of 3 to 10 Torr (where the hollow cathode effect is observed), M_3/N_a, N_{eg}/N_a and N_{eg}/M_3 vary at the most by 20%. This indicates that the behaviour of the discharge is determined strongly by variations in the rate coefficients or in other words by the electron energy distribution variation especially with respect to the hot electrons.

The various rate coefficients in the above equations will be considered after we have discussed the form of the electron energy distribution in the hollow cathode.

6.4 The electron energy distribution in the hollow cathode discharge

Many of the rate coefficients in the rate equations discussed in the previous section are sensitive to the ratio of hot to cool electrons N_{eh}/N_{eg} and to its variation with the discharge parameters. We first of all consider previous investigations on electron energy distributions in hollow cathodes, to see if data are available to calculate the ratio (N_{eh}/N_{eg}) under our discharge conditions. Also it is very important to see if we can calculate from the measured electron energy distribution the relative proportion of beam electrons (N_{eb}) and their contribution to excitation and ionization in the discharge compared to the total due to all the hot electrons.

Borodin and Kagan[84,85] and Kagan and Taroyan[86] have measured the electron energy distribution for a variety of discharge parameters and discharge dimensions and geometries. However, a close look at these

measurements show that these results cannot be used in our case because of the following:

(1) Borodin and Kagan[85] did their measurements in two separate cylindrical tubes both 10 cm long and 1 cm and 2 cm bore respectively, while the bore of our discharge is 0.6 cm. The difference in the bores leads to different values of the ratio of N_{eh}/N_{eg}. This was shown by Borodin and Kagan[85] who found that at a constant current (20 mA) N_{eh}/N_{eg} reached a maximum value at approximately 2 Torr for a discharge tube bore of 1 cm, while this ratio reached its maximum value at a pressure of 1.2 Torr for a discharge bore of 2 cm.

(2) The study which was done by Borodin and Kagan[85] or Kagan and Taroyan[86] is over a very small range of currents and pressures(less than 60 mA and less than 4 Torr). It is also not systematic enough to allow interpolation in the range studied.

(3) Comparing carefully the measurements of Borodin and Kagan[85] with those of Kagan and Taroyan[86] we find that even those measurements taken for similar geometries and for similar discharge conditions do not agree. For example, according to Borodin and Kagan[85] at a pressure of 0.9 Torr the ratio of electrons with energy at 24 eV to those at 2 eV decreases from 7.7×10^{-2} to 3.3×10^{-2} in going from 20 to 40 mA while according to Kagan and Taroyan[86] it increases from 2×10^{-2} to 6.5×10^{-2}.

In conclusion, the extensive measurements of Borodin and Kagan[85] and Kagan and Taroyan[86] are not consistent enough nor systematic enough to be useful in our case.

Recently Gill and Webb[28] measured the electron energy distribution in a planar hollow cathode discharge using a differentially pumped retarding field analyzer. The published electron energy distribution is for a current of 3.5 mA, a pressure of 10 Torr and a cathode dark space width of 1 mm. No systematic study of the variation of the distribution

with discharge parameters was undertaken, which is what we require in this discussion. In spite of the limited information given in that publication[28], the measured electron energy distribution for the above conditions can be used to deduce the relative importance of N_{eb}, N_{eh} to the excitation and ionization at the edge of the negative glow and at its centre, as it will be shown later (see table 6.1).

In spite of the above criticisms all the measurements[28,85,86] show that the electron energy distribution in the negative glow of a hollow cathode is characterized by two fundamental properties.

(1) Its shape is markedly non-Maxwellian and its deviation from that distribution depends on the discharge current and pressure.

(2) There is a beam electron component in the distribution which enters the negative glow from the dark space. This beam electron component has a role to play in excitation and ionization. For example, Gill and Webb[28] found that for the above conditions this component is about 1% of the total number of electrons.

Since measurements by previous investigations cannot be used in our case, it is necessary to deduce some qualitative information about the electron energy distribution from the previous chapters.

(1) Since the total electron density increases linearly with increasing discharge current (§ 3.5 and § 4.8.2) at a constant pressure and since the emissions of He I and He II transitions (§ 5.4.1) (which require an electron energy in excess of 20 eV for excitation) also increase linearly under the same discharge conditions, then we can say that the ratio of hot to cool electrons does not change as the current increases. Since this ratio does not change as we change the discharge current, then it is probably safe to use the electron energy distribution measured by Gill and Webb[28] at a pressure of 10 Torr and current of 3.5 mA in our study at the same pressure value and current range of 10 - 150 mA.

(2) We have seen in Chapter V that the emissions of He I and He II transitions decrease as the pressure increases and this occurs across the whole of the discharge. Since the upper levels of the He I transitions decay radiatively (see table 6.1 for example for 3889 Å), then the above indicates that the number density of the hot electrons decreases as the pressure increases.

(3) The existence of the high energy component originating from the dark space, which has been reported previously, can be seen by comparing the radial profiles of He II and He I transitions (§ 5.4.2). It was found that the He II transitions rise more sharply at the edge than the He I transitions. Since the He II levels require 75 eV for excitation compared to around 20 eV for the He I transitions, the radial emission profiles indicate that there is a source of high energy electrons in the dark space, and that these high energy electrons lose energy as they move across the negative glow.

(4) With increasing pressure the range of the high energy electrons originating from the dark space decreases. This can be seen by comparing radial profiles of He II and He I transitions at high and low pressures (Chapter V).

6.5 The particle number densities

In the following paragraphs the behaviour of the electron and singlet and triplet metastable number densities as a function of the discharge parameters will be discussed.

In table (6.1) typical values of the gain and loss rates associated with the dominant processes determining the electron (ion), singlet, triplet and 3^3P number densities are listed.

6.5.1 The magnitude of the electron number density

As we can see in table (6.1) the dominant creation process of electrons in the glow is ionization. This ionization is counterbalanced

by losses due to recombination and diffusion. The recombination rate in fact is about five orders of magnitude larger than the ambipolar diffusion rate which diminishes as the helium filling pressure increases. Also, total electron loss from the glow by diffusion is prevented by the retarding field in the dark space. The recombination is due to three body collisions (two electrons and one ion). This recombination loss is replenished by ionization within the glow, the flux of electrons to the anode being balanced by the flux of electrons from the dark space.

The electric field in the negative glow is related to the discharge current I and the electron drift velocity V_{eD} by the relations

$$I = A_D \, e \, V_{eD} \, N_e = A_D \, e \, \mu \, P \, \left(\frac{E}{P}\right) \qquad (6.5.1)$$

where A_D is the cross-sectional area of the discharge and μ is the mobility of the electrons.

Because electron loss in the glow is small and also because of the beam component from the dark space, the electric field required to maintain the ionization is also small (see Chapter II and reference 14). Hence under given discharge current conditions, the electron number density is large. This of course means that because of charge neutrality in the glow, the ion number density is also large. This is confirmed by the experimental measurements on electron and ion number densities, and explains the superiority of the hollow cathode over the positive column[7,8] as a medium for charge exchange excitation.

The calculations in table (6.1) confirm that the expected electron number density at the tube edge is about 5×10^{13} cm^{-3}. At the tube centre the calculations (table 6.1) indicate that the electron number density must be in the range of 2×10^{13} cm^{-3}, which is comparable to the measured one. The difference between calculated and measured values at tube centre is perhaps due to underestimating the number density of beam electrons, which play a significant part in the ionization. These

calculations also indicate that the electron number density at 10 Torr reaches a maximum value at the tube edge. That is in general agreement with the behaviour of the radial profiles of metastables and excited states.

6.5.2 The dependence of the metastable number densities on the discharge parameters

It has been shown in Appendix II that the metastable singlet and triplet number densities are different and that they behave differently as a function of the discharge current and pressure. We now discuss these results.

The calculations in table (6.1) show that excitation to the metastable levels is done by both the beam and hot electrons. The predicted number density of the metastable triplet at the tube centre differs from the measured one by a factor of five while the number density of the singlet metastables differ by about two orders of magnitude. At the tube edge the difference between the calculated and the measured values for (2^1S) and (2^3S) number densities are even larger.

The behaviour of (2^1S) and (2^3S) as a function of current and pressure can be discussed as follows:

We have seen before that as the discharge current increases, the ratio of hot to cool electrons stays almost constant. Since direct excitation from the ground state is the dominant process in populating (2^1S) and collisional ionization is the dominant destruction process (see equation 6.2.2 and table 6.1) then the constant value of N_{eh}/N_{eg} explains the observed saturation of the singlet metastable number density. However this does not explain the linear behaviour of the triplet metastable with current.

The explanation of the different behaviour as a function of current and pressure may lie in examining in detail the collisional processes

responsible for populating each of them, so these processes will be studied carefully.

(1) A look at the cross-sections[16,78] for direct excitation to (2^1S) and (2^3S) from (1^1S) by electrons shows that while the cross-section for the process 1^1S to 2^1S increases continuously with electron energy, the excitation cross-section to (2^3S) decreases for electron energies higher than 25 eV. Further the composite cross-section[78] for excitation to (2^3S), which takes into account cascade from higher levels, rises sharply in the vicinity of an electron energy of 20 eV and decreases for energies above 50 eV. The composite cross-section for excitation to (2^1S) changes much more slowly with electron energy reaching a broad maximum around 50 eV. This suggests that changes in the form of the electron distribution above 20 eV may therefore account for the different behaviour of the singlet and triplet metastable number densities with discharge conditions. However the excitation cross-sections to excited singlet and triplet states show a similar behaviour with electron energy to the cross-sections for excitation to the metastable states. For example the cross-sections for electron excitation to the 3^1P and 4^1P states are almost flat for electron energies in excess of 100 eV[83], and this is markedly different from the behaviour of the cross-sections associated with the corresponding triplet states. Yet these excited states / 3^1P, 4^1P, 3^3P number densities are found to behave similarly as a function of discharge current and pressure regardless of whether they are singlets or triplets (Chapter V).

(2) If we look at table (6.1) we find that electron induced conversion from 2^1S to 2^3S or vice-versa is important. However the estimated values for conversion rate coefficients differ from one investigator to another[81,87] by one to three orders of magnitude for 1 eV electrons making a large degree of uncertainty in estimating this effect. Further this gain

mechanism to 2^1S is about an order of magnitude smaller than the electron direct excitation from the ground state. This means that there is not complete mixing between (2^1S) and (2^3S) otherwise they would behave similarly as a function of current and pressure.

(3) If we compare the radial profiles of the excited states (He I and He II) and the metastable number densities (2^1S and 2^3S) we find that they are similar suggesting that diffusion loss of the metastable can not be dominant. This is confirmed by the calculations in table (6.1) where the diffusion loss at 10 Torr is about five orders of magnitude smaller than the ionization loss. The diffusion time for the triplet or singlet metastables in a discharge of 3 mm bore and at 10 Torr is about 1.9×10^{-3} sec. On the other hand the lifetime of 2^3S or 2^1S as a result of collisional destruction by electron conversion from one metastable state to the other and ionization is about 1 μ sec (the radiative lifetime of the excited states is in the range of 9.1×10^{-8} sec[88]). So during 1 μ sec metastables created at the edge of the negative glow diffuse less than 10^{-2} mm. On the other hand, as we increase the gas pressure the hot electrons at the tube centre are decreasing, so they cannot make any excitation at the tube centre which leads to the appearance of the dip (see table 6.1).

(4) From table (6.1) we can see that one of the dominant loss mechanisms is ionization for both the triplet and the singlet metastables. However, the ionization cross-sections[79,80] for both singlets and triplets are similar. This suggests that the ionization loss cannot be used to explain the differencein the behaviour of (2^1S) and (2^3S) as a function of the discharge current and pressure.

In conclusion the estimated rate coefficients in table (6.1) are not consistent with the magnitudes of the metastable number densities, nor can they explain the markedly different behaviour between singlets and

triplets as a function of the discharge parameters. The appearance at higher pressures of a dip in the radial profiles of the number densities is however consistent with decreasing excitation towards the tube centre, because of the loss of beam and hot electrons, in the presence of ionization as the predominant loss mechanism.

A more satisfactory explanation of the behaviour of the metastable number density must probably await a more detailed knowledge of the electron energy distribution and its dependence on current, pressure, position in glow, etc than is available at present.

The relation between metastable number density and cathode fall potential under conditions of constant discharge current and pressure (Appendix II) is probably due to a dependence of cathode fall potential on metastable number density rather than vice-versa. If for any reason the metastable number density decreases, then this leads to a decrease in the corresponding secondary emission process at the cathode. The cathode fall potential must then increase in order to maintain the discharge current by increasing the other secondary emission processes.

When the cadmium is introduced to the discharge another loss process namely the Penning ionization is introduced. This would lead to the observed fall of the triplet metastable number density as the cadmium increases (see Appendix II, figure A2.5).

6.6 The excitation in the negative glow

We have seen that in the negative glow, all the measured He I and He II transitions behave similarly as a function of the discharge current and pressure. On the other hand the radial profiles of He I and He II differ by the sharper rise of He II radial profiles at the negative glow edge. We now consider the behaviour of the 3889 Å transition (an He I transition) as a function of discharge parameters.

The excitation of the cadmium transitions 4416 Å and 5578 Å behave

quite differently from that of 3889Å transition so they will be treated in a separate section (6.6.2).

6.6.1 The excitation of the 3889Å transition

The upper level (3^3P) of the 3889Å transition may be populated by direct excitation from 1^1S or 2^3S. The loss mechanisms for this transition are diffusion (the diffusion time in a discharge of 3 mm bore is 1.9×10^{-4} sec[87]) radiative decay which has a rate of 9.1×10^{-8} sec[88], electron ionization (which has a rate coefficient of 3.5×10^{-8} sec^{-1}) and de-excitation to the ground state (which is negligible compared to the ionization) or to 2^3S (see table 6.1).

The 3^3P level can also be destroyed by excitation transfer or associative ionization[101]. At an He helium pressure of 1 Torr these processes are negligible compared to the radiative decay. At a helium pressure of 10 Torr the associative ionization process is about a factor of two larger than the radiative decay rate while the excitation transfer becomes comparable to the radiative decay.

Table (6.1) shows that direct excitation from the ground state is the dominant mechanism followed by excitation from 2^3S. As the pressure increases the hot electrons in the discharge decrease and that leads to the decrease in the emission. Also as the pressure increases the associative ionization process increases which makes the decrease in the emission more pronounced. The decrease of the emission with the cathode fall potential can be explained in terms of a decreasing electron energy.

The dominance of direct excitation from the ground state is consistent with a linear dependence of emission on discharge current. If excitation to the 3^3P state were predominantly through the 2^3S state, which increases linearly with discharge current, then the 3^3P state emission would show a super linear dependence on current.

6.6.2 The excitation mechamisms of 4416Å and 5378Å

Emission at 4416Å may arise as a result of Penning ionization (which has a reaction rate per cm^3 per sec,PI), electron excitation from the cadmium atom ground state (which has a reaction rate per cm^3 per sec, EG)

and excitation from the cadmium ion ground state (which has a reaction rate per cm^3 per sec, EI). Emission at 5378 Å, may arise as a result of cascade (which has a reaction rate per cm^3 per sec, DI) from the transition 6360 Å ($6\ g^2\ G_{9/2,\ 7/2} - 4\ f^2\ F_{7/2,\ 5/2}$) (which is excited through the Duffendack reaction[6]), electron excitation from the cadmium ground state (EG_1) and electron excitation from the cadmium ion ground state (EI_1). In the following the reaction rates of all the above processes will be compared with each other to determine the dominant process.

(1) The ratio of the excitation rate to the upper level of 4416 Å resulting from electron collisions with the cadmium ground state to that of Penning excitation is

$$\frac{EG}{PI} = \frac{\langle \sigma_{g_1} V_{e_1} \rangle N_e N_{cd}}{\langle \sigma_p . V_{12} \rangle M_3 N_{cd}} \qquad (6.6.2.1)$$

where σ_{g_1}, σ_p are the excitation cross-sections from the cadmium ground state to the upper level of 4416 Å, and Penning ionization respectively, and they are equal to 2.4×10^{-17} cm^2[90] and 4.5×10^{-15} cm^2[91] respectively, and V_{e_1} and V_{12} are the velocity of the colliding electron and helium metastable respectively and they are equal to 2.48×10^8 cm sec^{-1} and 3.85×10^5 cm sec^{-1} respectively. For an electron number density of 10^{11} cm^{-3} and a metastable number density of 5×10^{11} cm^{-3} equation (6.6.2.1) gives (EG/PI) a value of 7×10^{-2}.

(2) The ratio of the excitation rate from the cadmium ion ground state to that from Penning ionization is

$$\frac{EI}{PI} = \frac{\langle \sigma_{i1} V_{e_2} \rangle N_e N_{cd^+}}{\langle \sigma_p V_{12} \rangle M_3 N_{cd}} \qquad (6.6.2.2)$$

where σ_{i1} is the cross for electron excitation from the cadmium ground state to the upper level of 4416 Å and V_{e_2} is the velocity of the colliding electron. The above equation cannot be assessed because of the lack of information about the value of σ_{i1}. However, we can say that for a N_{cd^+} value of 10^{11} cm^{-3}, a N_{cd} value of 10^{13} cm^{-3}, V_{e_2} of equal to 2.84×10^8 cm sec^{-1}, then for $\frac{EI}{PI}$ to equal unity, σ_{i1} must be at least

1.45×10^{15} cm^2. In other words σ_{i1} must be comparable to σ_p, and this is unlikely.

The above suggests that in the present case the population of the upper level of 4416 Å occurs as a result of Penning ionization. The experimental observations are consistent with these calculations as can be seen in figure (5.7b) where the behaviour of the 4416 Å emission as a function of the pressure follows that of the metastables. If the electrons were responsible, then the 4416 Å emission would fall with pressure as the number density of the high energy electron decreases.

(3) The ratio of the excitation rate by electrons from the cadmium ground state to the upper level of 5378 Å to that of Duffendack excitation is

$$\frac{EG}{DI} = \frac{\langle \sigma_{g_2} V_{e_3} \rangle N_e N_{cd}}{\langle \alpha_D V_{12} \rangle N_i N_{cd}} \qquad (6.2.2.3)$$

where σ_{g_2} and σ_D are the cross-sections for electron excitation from the cadmium ground state and charge transfer to the upper levels of 5378 Å respectively and are equal to 10^{-17} cm^2 (this value is approximated from the value of the total ionization cross-section from the cadmium ground state by electron impact which is equal to 7×10^{-17} cm^2[92]) and 7.7×10^{-16} cm^2[93] respectively. The velocities V_{e_3} and V_{12} are the electron and helium ion velocities and equal to 1.73×10^8 cm sec^{-1} and 3.85×10^5 cm sec^{-1} respectively. For N_i equal to N_e we find that $\frac{EG}{DI}$ is about 9.6×10^{-2}, which suggests that the excitation from the cadmium ground state to the upper level of 5378 Å is negligible in comparison to Duffendack pumping.

(4) The ratio of the excitation rate by electrons from the cadmium ion ground state to that of Duffendack pumping is

$$\frac{EI}{DI} = \frac{\langle \sigma_{i2} V_{e_4} \rangle N_e N_{cd^+}}{\langle \sigma_D V_{12} \rangle N_i N_{cd}} \qquad (6.2.2.4)$$

where σ_{i1} is the excitation cross-section from the cadmium ion ground state and V_{e_4} is the electron velocity. An assessment of the above ratio is not possible because of the lack of information about σ_{i1}. However, for a value of V_{e_4} of 2.22×10^8 cm sec^{-1}, then for $\frac{EI}{DI}$ to equal unity it requires that σ_{i2} be equal to 1.34×10^{-14} cm^2. This is about two orders of magnitude larger than the Duffendack cross-section for the upper level of 5378 Å. This value of the cross-section is highly unlikely. This suggests that the upper level of 5378 Å is populated by the Duffendack reaction. Again, the experimental observations are consistent with these calculations as can be seen in figure (5.7b). The emission at 5378 Å follows the ion number density as a function of pressure.

Table (6.1)

3.5 mA
10 Torr
1.5 mm

The relative contribution of beam, hot and cool electrons to the processes in the hollow cathode discharge
The unit is (cm^{-3} sec^{-1})

Processes	beam electrons at edge of glow energy ~ 200 eV* $V \simeq 8.4 \times 10^8$ cm sec^{-1} $N_{eb} = 5 \times 10^{11}$ cm^{-3}	hot electrons 25 $eV^{\pm}$ $V = 2.96 \times 10^8$ cm sec^{-1} $N_{eh} = 2.2 \times 10^{12}$ cm^{-3}	cool electrons 6 $eV^{\pm}$ $V = 1.03 \times 10^8$ cm sec^{-1} $N_{eg} = 4.730 \times 10^{13}$ cm^{-3}
ionization [30]	5.15×10^{21}	2.0×10^{20}	-
three-body recombination [67]	-	-	8.0×10^{21}
Diffusion [87]	-	-	3.0×10^{16}
$1^1S - 2^3S$ [78]	1.47×10^{20}	10^{21}	-
$2^3S - He^+$ [79]	2.52×10^{15}	2.6×10^{17}	3.9×10^{18}
$2^3S - 3^3P$ [89]	4.2×10^{16}	3.3×10^{17}	3.8×10^{18}
$2^3S - 1^1S$ [16,78]	4.2×10^{13}	10^{15}	10^{17}
$1^1S - 3^3P$ [83]	7.35×10^{20}	3.5×10^{19}	-
3^3P radiative [88]	-	-	3×10^{17}
Diffusion of 2^3S [87]	-	-	1.9×10^{12}
$2^3S - 2^1S$ [81,16]	-	-	4.6×10^{19}
$1^1S - 1^1S$ [16]	2.94×10^{20}	6.8×10^{20}	-
$2^1S - He^+$ [80]	8×10^{14}	1.6×10^{17}	10^{18}
$2^1S - 1^1S$ [16]	1.9×10^{15}	1.7×10^{14}	1.6×10^{15}
$2^1S - 3^1P$ [16,89]	1.8×10^{14}	8.3×10^{15}	2.4×10^{17}
$1^1S - 3^1P$ [83]	4.1×10^{20}	2.1×10^{20}	-
$1^1S - 4^1P$ [83]	2×10^{20}	7×10^{19}	-
$2^1S - 2^3S$ [81]	-	-	3.9×10^{17}

APPENDIX I

THE CONSTRUCTION OF THE HOLLOW CATHODE DISCHARGE

A1.1 The construction of the hollow cathode discharge for the steady state case

The objective is to develop a stable hollow cathode discharge capable of evenly distributing the metal vapour atoms (when the metal is used) and operates with current density in the range of 3.5×10^{-4} - 7×10^{-2} A cm^{-2}. This was achieved by employing a multi anode system with a common hollow cathode.

The discharge tube consists of a long cylindrical stainless steel tube (6 mm bore). Stainless steel was chosen because of its good thermal conductivity (this ensures an even temperature distribution), its mechanical strength, and its easy handling. This tube was terminated at each end by a Kovar tube acting as a condenser to prevent the metal (cadmium) from reaching the Brewster angle windows (see figure 1.1d).

A number of tungsten rods (3 mm dia) positioned at appropriate intervals (7.5 cm) along the cathode acted as anodes. Preliminary experiments suggest that this distance is good enough to ensure a uniform discharge by allowing a certain degree of overlapping between the discharges associated with adjacent anodes. Each anode was ballasted separately by 60 W (250 V) lamps to ensure equal division of the total current among them. The anodes are sleeved with quartz and inserted in stainless steel tubes positioned along the hollow cathode structure (see figure A1.1a). The end of each anode is recessed from the bore to reduce the possibility of arcing. Vacuum sealing at the extreme end of the anode was achieved by an O-ring placed around the quartz tube and compressed against the end of the tube with a threaded ring.

A side arm (7.5 cm long, 6 mm bore) through which the gas flows on its way into the tube was placed mid-way between the two anodes and was used as an oven. This ensures even distribution of the metal (cadmium) atoms in

the discharge. The evolution of the metal atoms into the discharge was controlled by controlling the side arm temperature by a Cr-Aℓ thermocouple. The thermocouple was tied around the oven and covered with a thin sheet of asbestos. Care has been taken to ensure good thermal contact between the thermocouple and the oven. The output of the thermocouple was connected to temperature controller (Ether-Digi). This oven structure proved to be effective in eliminating the instabilities in the discharge which result in uncontrolled metal vapour partial pressure.

Cadmium wire of natural isotopic composition is placed inside the oven whose temperature is stabilized to $\pm$ 1°C by the temperature controller. The cadmium vapour enters the discharge tube from the oven through a hole drilled in the tube.

In order to maintain the gas purity a flowing gas system was employed. Helium of 99.995% from a high pressure cylinder, was premixed with the metal in the side oven and pumped out from the tube end. The helium filling pressure was measured by a Bourdon gauge which had been calibrated against a capacitance monometer in the range (0-20 Torr). The tube was driven by a smoothed unregulated DC power supply (5 KV, 1000 mA).

For the tube described above the required voltage to initiate the discharge is nearly 600 V in the above pressure range. The running voltage of the discharge is in the range 200-220 V.

A1.2 Description of the hollow cathode discharge and its circuit which is used in the laser heterodyne experiment

Basically the description given above also applies to the hollow cathode discharge used in the heterodyne experiment. However in the latter case it was necessary to shorten the length of the discharge, to facilitate fitting inside the laser (2) cavity (see figure 4.1).

The rapid switching of the discharge was achieved by employing a thyratron system. This system can be used for crowbarring the discharge. The crowbar system can be seen in figure (A1.1b). It consists mainly of the thyratron (English Electric CX1164) which switches the discharge off during a time of about 200 μ sec.

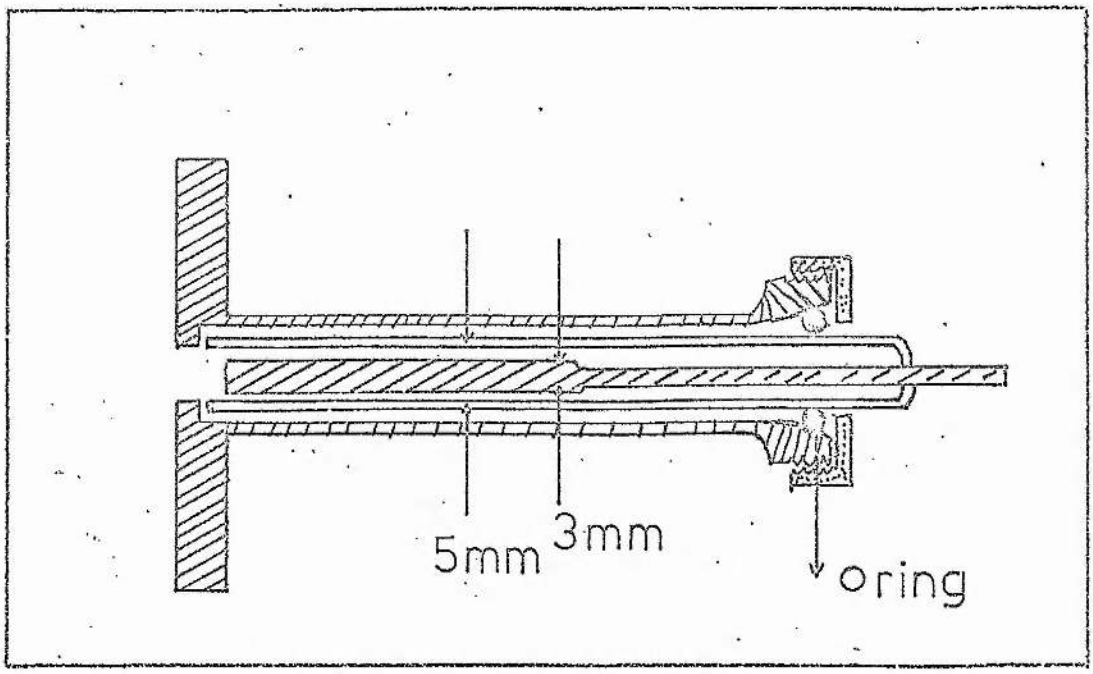

Figure A1.1a. The anode structure inserted inside the steel sleeve.

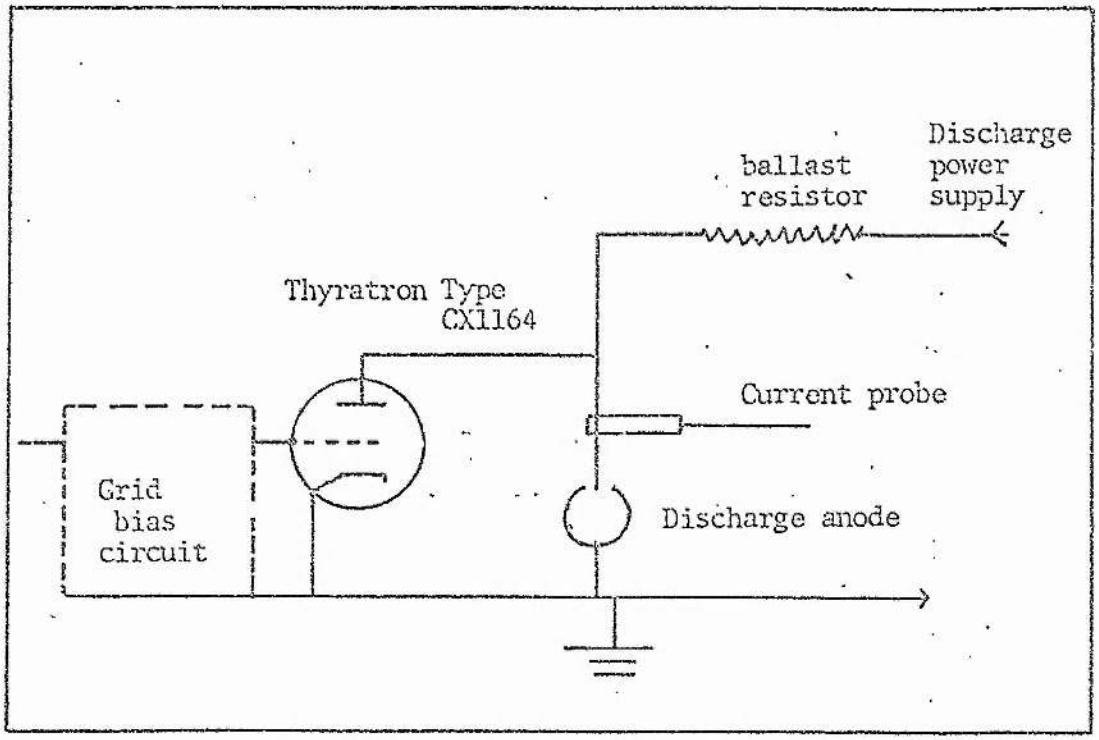

Figure A1.1b. The circuit of the crowbar discharge.

APPENDIX II

METASTABLE NUMBER DENSITIES IN A HOLLOW CATHODE He DISCHARGE

A2.1 Introduction

Metastable number densities are important in assessing the role of the Penning ionization process. Number densities deduced from absorption experiments (which were done by I A McIntosh and M H Dunn), plasma length and Doppler profile measurements described in Chapter II will be presented here because of their relevance to the hollow cathode studies. In the following the results of the above work will be summarized only.

A2.2 Populations of He (2^3S) and He (2^1S) levels

Metastable populations were investigated using two variants of the standard line absorption technique[94,95] to measure the absorption introduced by the hollow cathode discharge at 5016 Å ($3p^1P - 2s^1S$), 3965 Å ($4p^1P - 2s^1S$) and 3889 Å ($3p^3P - 2s^3S$).

In the first method a separate helium discharge was used as an illuminating source, while in the second the self-absorption of the discharge was measured using the technique due to Harrison[95]. In both cases the effect of different discharge lengths was examined by running different numbers of anodes. The absorption per unit length, and hence the population densities, were found to be independent of the number of anodes for those conditions where the negative glows of adjacent anodes do not overlap (see § 2.2). The results to be discussed below apply to the case of only one anode operating.

Population densities were deduced from the measured absorptions using the plasma length measurements (see § 2.2), and the measured linewidths of the transitions (see § 2.6). Allowance was made for the hyperfine splitting of the triplet[7] transition at 3889 Å and for the different linewidth of the illuminating source used in the first method.

In deducing populations from the measured absorptions, we have assumed negligible populations in the upper levels of the transitions monitored. This assumption was confirmed by comparing the ratio of the

absorption coefficient at 5016 Å with that at 3965 Å - these two transitions share a common lower level - when no systematic deviation from the value of 3.7, expected in the absence of upper level populations was found[7].

In figures (A2.1a,b), the singlet metastable density at the tube centre is shown as a function of discharge current and discharge pressure respectively. The singlet density saturates with increasing discharge current at currents above about 40 mA. The singlet density is independent of pressure in the range 2 - 15 Torr, after initially decreasing with increasing pressure below 2 Torr. In figures (A2.2a,b) the dependence of triplet density on discharge current and discharge pressure respectively is shown. Unlike the singlets, the triplet density increases approximately linearly with the current up to the maximum currents used (150 mA). This behaviour was found to occur over the whole pressure range investigated. Also comparison of figure (A2.2b) and figure (2.1b) shows that the triplet density has similar behaviour to the cathode fall in its variation with pressure. Likewise this behaviour occurred over the whole current range investigated. So in both cases the singlet and triplet densities behave quite differently with discharge parameters.

We have already pointed out that it is possible to vary the cathode fall potential, at constant current and pressure, away from its usual stable value. We have measured the variation of triplet metastable density (at tube centre) as a function of the varying cathode fall. These measurements are shown in figure (A2.3) where the dotted curves refer to unstable regions of the cathode fall potential, and the solid curves to the stable regions. It can be seen that at constant current and pressure the triplet metastable density decreases monotonically with increasing cathode fall potential. The characteristic pressure behaviour associated

with the triplet densities arises because of the varying locations of the stable regions of the discharge on the curves of figure (A2.3).

A2.3 Radial profiles of metastable densities

The radial distribution of metastable densities was investigated by measuring the variation in line absorption across the hollow cathode using the optical arrangement described in Chapter V. In figures (A2.4,a,b) the radial profiles for the singlet and triplet densities are shown for a constant current of 100 mA and for a range of pressures from 1 to 30 Torr. The radial resolution is about $\pm$ 0.25 mm. Both singlet and triplet densities show a broad maximum at the tube centre at low pressures (around 2 Torr); are approximately constant across the bore in the intermediate pressure range (2 - 10 Torr); and show a minimum at tube centre for high pressures (> 10 Torr), the peaks in density having now moved towards the tube wall. The different variation in singlet and triplet densities with pressure, already discussed in (§ A2.2), is also apparent in these radial profile measurements.

A2.4 Influence of cadmium on metastable densities

As cadmium is introduced into the discharge at constant current and helium pressure, by increasing the temperature of the cadmium oven at the gas inlet, the cathode fall in potential increases. At the same time the triplet metastable number density decreases. This behaviour is shown in (A2.5). The cathode fall potential increases with the increasing cadmium neutral density, while the triplet metastable density increases.

The dependence of triplet metastable density on cathode fall is therefore similar to the case where the discharge is operated in an unstable region (§ A2.2). At constant discharge current and pressure the triplet metastable density appears to be determined by the cathode fall potential.

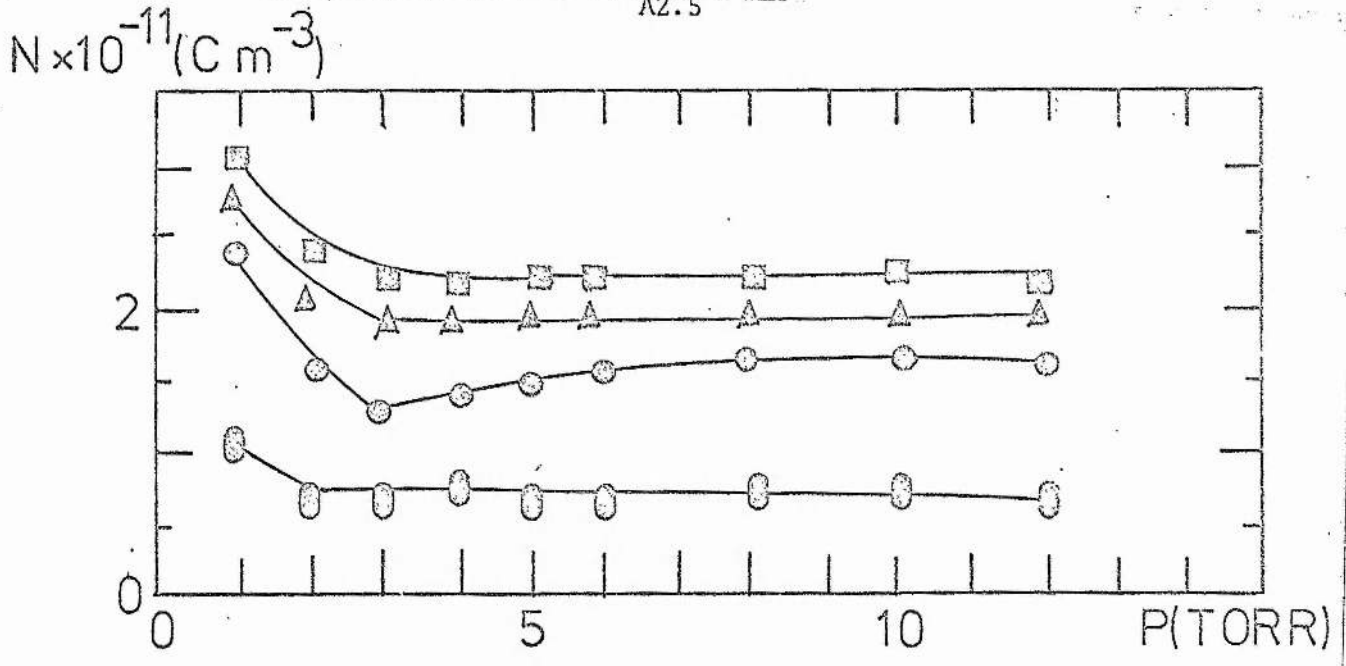

Fig A2.1a . The singlet metastable number density (cm^{-3}) as a function of pressure for different current values
20 mA, 40 mA, 100 mA and 140 mA.

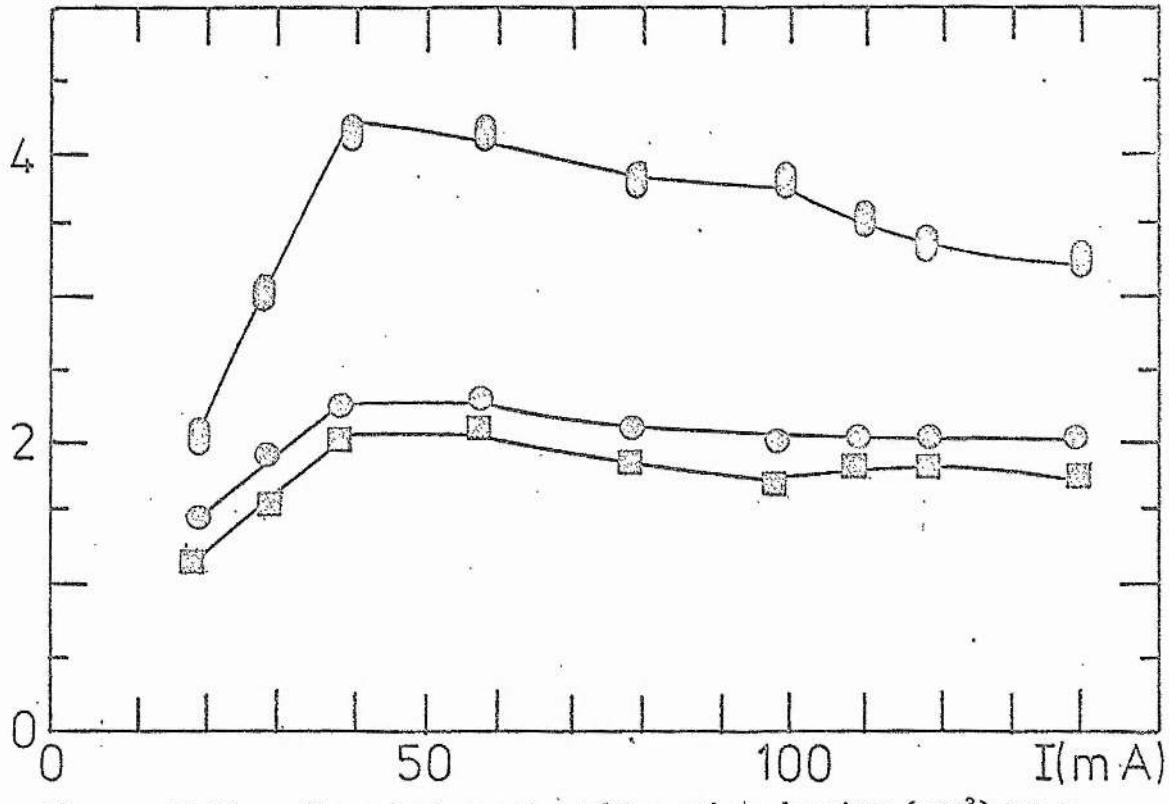

Figure A2.1b . The singlet metastable number density (cm^{-3}) as a function of current for different pressures
1 Torr, 6 Torr, and 10 Torr.

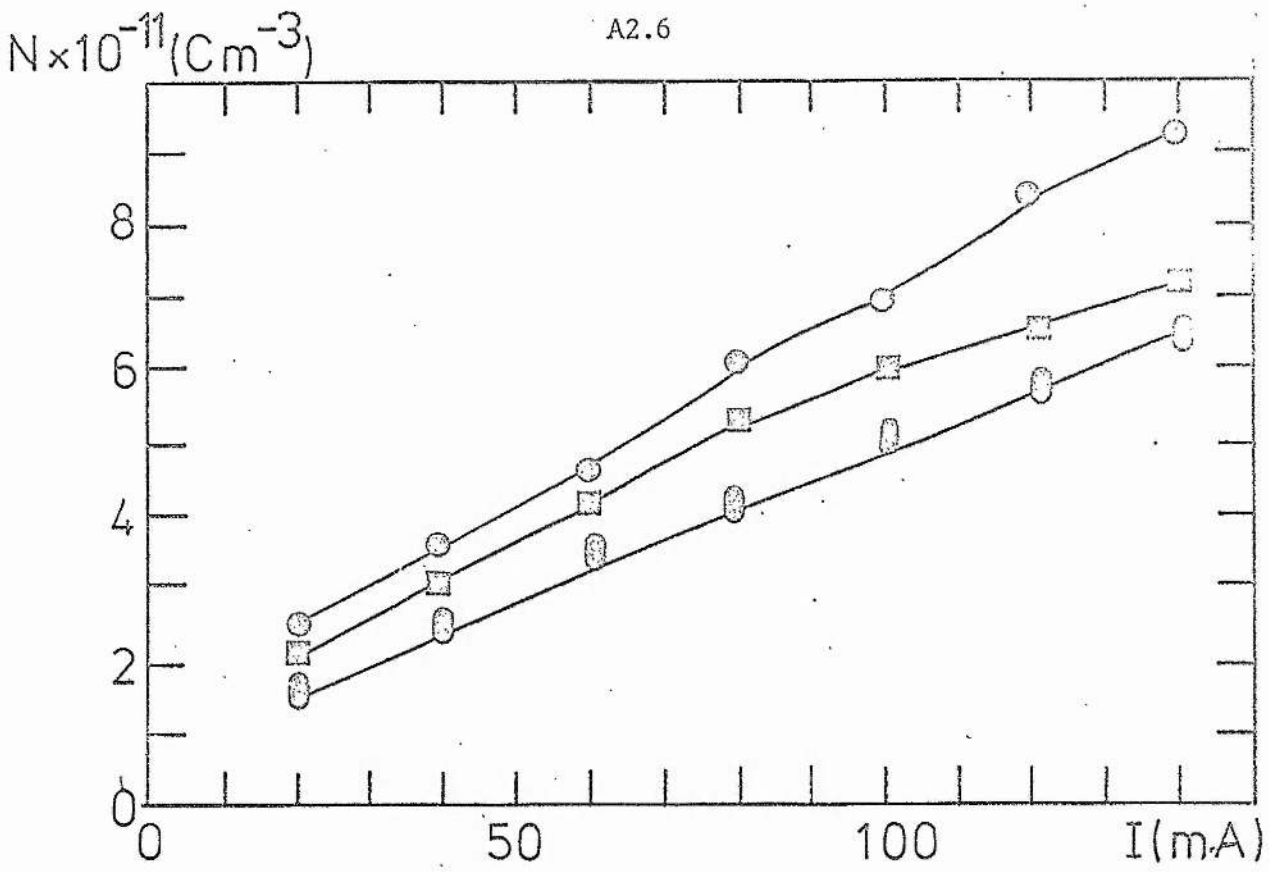

Fig A2.2a . The triplet metastable number density (cm^{-3}) as a function of current at different pressures
▣ 1 Torr, ▯ 6 Torr, ○ 10 Torr.

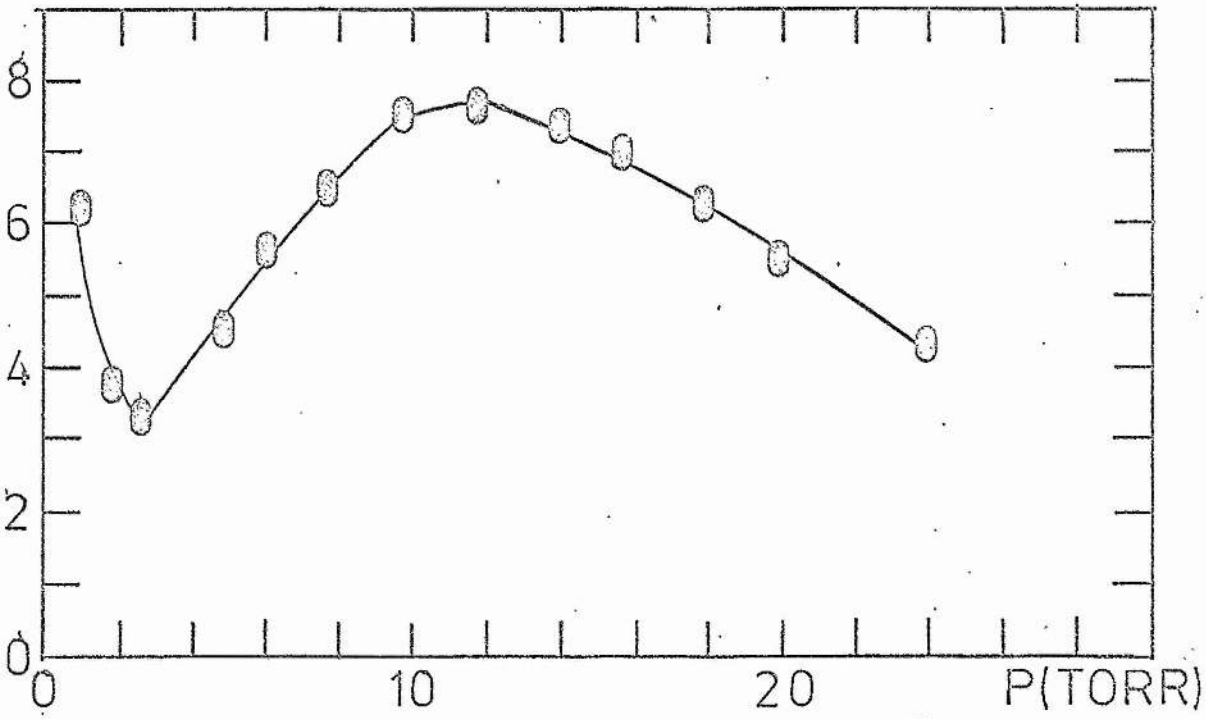

Fig A2.2b . The triplet metastable number density (cm^{-3}) as a function of pressure at a constant current of 100 mA.

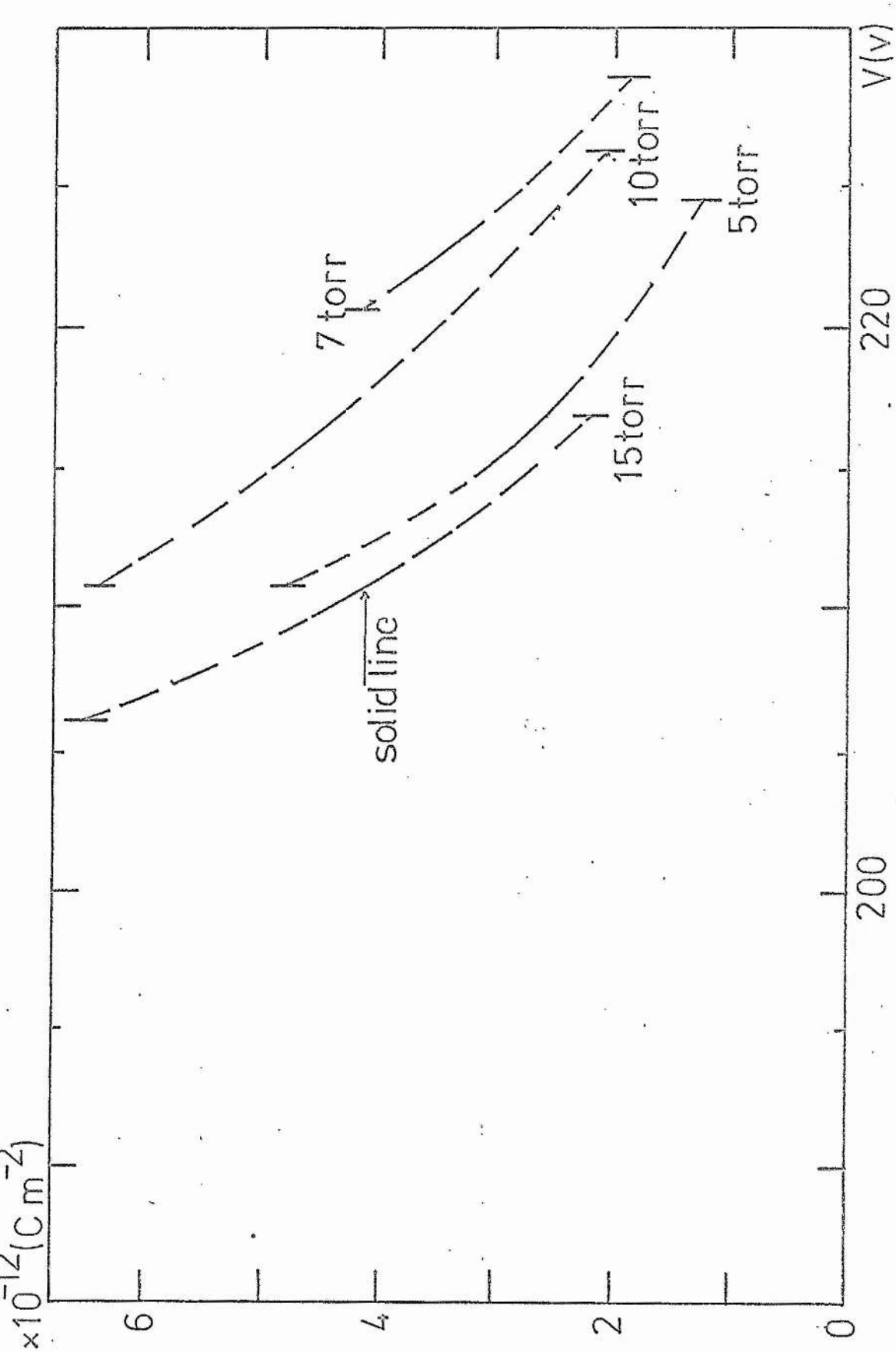

Fig A2.3 . The triplet metastable number density multiplied by discharge length (cm^{-2}) as a function of cathode potential V for a constant current of 100 mA and pressure values of 15 Torr, 5 Torr, 10 Torr and 7 Torr respectively. The solid lines represent the stable operating regime of the discharge.

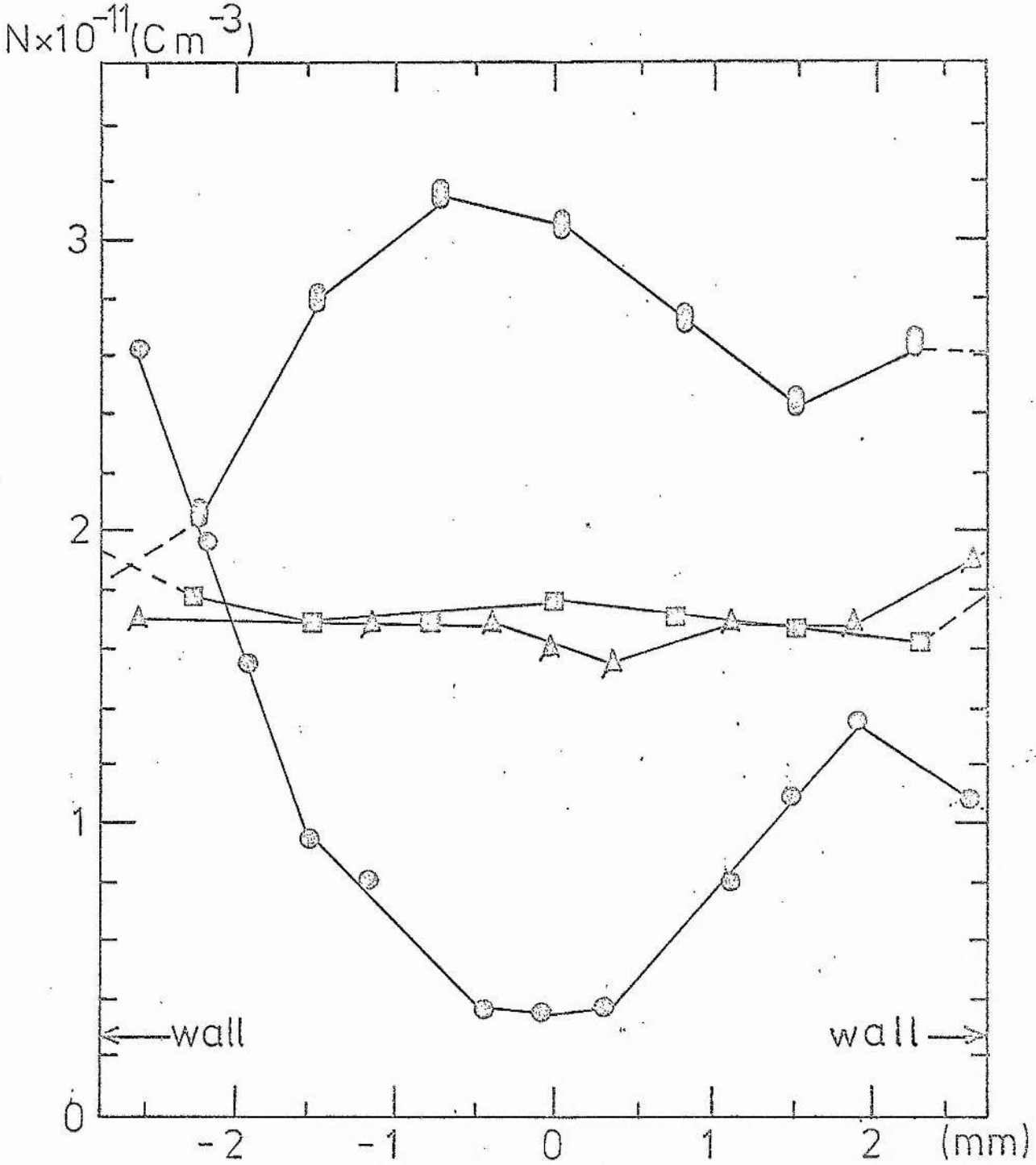

Fig A2.4a . The Radial measurements of the singlet metastable number density (cm^{-3}) at a current of 100 mA and pressure values of ⊖ 1 Torr, ⊡ 3 Torr, △ 10 Torr and ⊙ 30 Torr. Tube bore 6 mm.

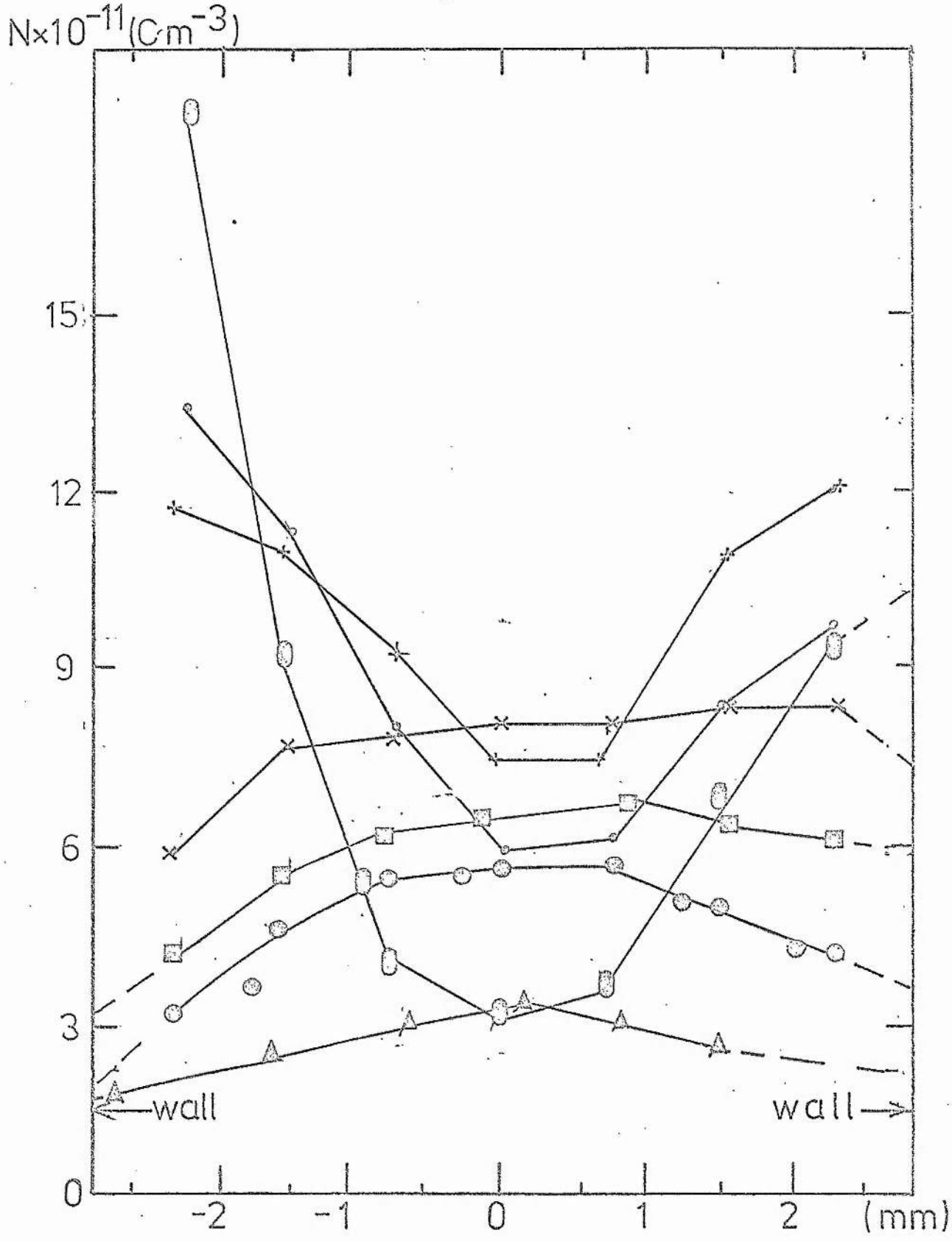

Figure A2.4b. Radial measurements of the triplet metastable number density (cm^{-3}) at a current of 100 mA and different pressure values of □ 1 Torr, △ 3 Torr, ○ 6 Torr, X 10 Torr, + 14 Torr, ◦ 20 Torr and ⬯ 30 Torr. Tube bore 6 mm.

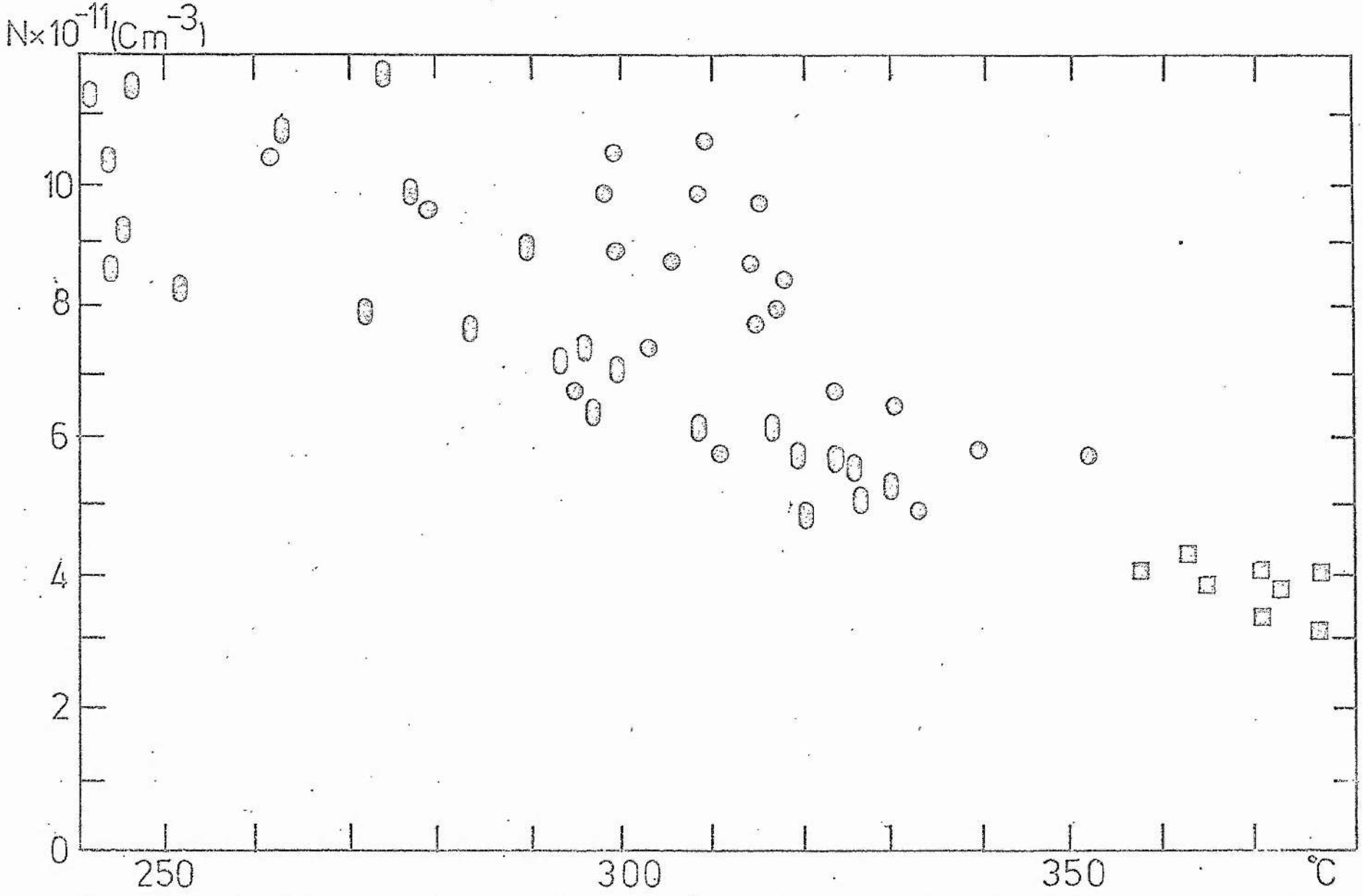

Fig A2.5 . The triplet metastable number density (cm^{-3}) as a function of the cathode fall potential as the Cd oven temperature is increased from 230 to 300°C. Operating conditions 100 mA and 8 Torr. The different symbols represent different experimental runs.

APPENDIX III

CONVOLUTION OF LINE PROFILES DUE TO STARK AND DOPPLER BROADENINGS

The line profile of the Hβ transition is a composite profile of Stark, Doppler and Lorentzion (instrumental) profiles. It is also affected by the hyperfine splitting which assumes a constant value of 10.2 GHz.

Stark and Doppler profiles depend on the electron number density and temperature and the gas temperature, while the Lorentzian profile depends on the finesse of the interferometer.

A computer programme (IBM 360/144) was run to study the convolution of the Stark and Doppler profiles (see figure A3.1).

The values of the Stark line profile $S(\alpha)$ (α is the reduced wave length and is defined by the relation $\alpha = \frac{\Delta\lambda}{F}$, figure 3.1a) was taken from Griem[19], for a range of electron number densities and electron temperature of 5000 $\overset{o}{K}$ ($\frac{r_o}{\rho_D} \leq 0.247$). The values of $S(\alpha)$ were calculated by Griem[19] using Baranger and Mozer[23,24] electric field distribution. Since this distribution depends on $\frac{r_o}{\rho_D}$ then as $\frac{r_o}{\rho_D}$ varies, so does the width of the Baranger and Mozer electric field distribution vary. It was shown in Chapter III (figure 3.1c) that as $\frac{r_o}{\rho_D}$ varies from 0.2 to 0.8 the full width at half maximum varies only by 44%. In our case $\frac{r_o}{\rho_D}$ is about 0.54 (see table 3.2) hence the full width at half maximum for the fine profile $S(\alpha)$ which was calculated by Griem[19] differs from the line profile expected in our system by less than 20%. Furthermore in both cases the general line shapes are similar. Hence $S(\alpha)$ which was calculated by Griem can be taken to represent the Stark profile in our system.

The Doppler profile was calculated for a gas temperature of 600 $\overset{o}{K}$. An example of the generated profiles can be seen in figure (3.2). These profiles are convoluted with the hyperfine structure effect to produce the overall profile (see figure 3.2) which is similar to the measured profile (see figure 3.3).

```
// FOR
* IOCS (CARD, TYPEWRITER).
LIST SOURCE PROGRAM
      DIMENSION AM(70), SAM(70), F(3), A(70), P(100),
      READ (2.24), SAM (I = 1.35)
      READ (2.25), F, DW, D,
      DO 3T = 2.35
3     SAM (J + 34) = SAM (J)
      SAM (70) = 0.086
      AM (1) = 0.0
      DO 4J = 2.35
4     AM (J + 34) = - AM(J)
      AM (70) = - 0.35
      DO 8J = 1.3
      WRITE (1.27), F(J)
      DO 6I = 1.70
6     A(I) = F(J) *AM(I)
      P(1) = 0.0
      DO 7K = 2.100
7     P(K) = P(K - 1) + ((2 *DW + A(35))/50.0
      DO 8L = 1.50
      CON = 0.0
      CO 9K = 1.70
9     CON = D *EXP (-((P(L) - A(K))/DW) **2)
            *SAM(K) *F(J) *0.01 + CON
8     WRIT (1.26) P(K), CON
27    FORMAT (1F 10.5)
```

```
24    FORMAT (8F 10.5)
25    FORMAT (5F 10.5)
26    FORMAT (2F 10.5)
          CALL # EXIT
      END
```

Figure A3.1. Listing of the program used to generate the composite profile of Hβ.

References

1. W T Silfvast, Appl Phys Lett 13 169 (1968)
2. J P Goldsborough, J Quantum Elect QE5 133 (1969)
3. W T Silfvast and M B Klein, J Appl Phys Lett 17 400 (1970)
   M B Klein and W T Silfvast, Appl Lett 18 482 (1971)
4. K G Hernqvist, Laser Focus 9 39 (1973)
5. W T Silfvast, Phys Rev Lett 27 1489 (1971)
6. J M Green and C E Webb, J Phys B Atom Molec Phys 7 1968 (1974)
7. P G Browne and M H Dunn, J Phys B Atom Molec Phys 6 1103 (1973)
8. A L McKenzie, Thesis, University of St Andrews (1975)
9. W K Schuebel, Appl Phys Lett 16 470 (1970)
10. A J Palmer, Appl Phys 41 3906 (1970)
11. C C V Voorhis and A G Shinston, Rev Sci Inst 12 257 (1941)
12. P F Little and A von Engel, Proc Roy Soc A224 209 (1954)
13. C Francis, Handbuch der Physik, Gas discharges 22-II, Berlin, Germany, Springer-Verlag
14. V S Borodin, Y M Kagan and R I Lyagushchenko, Sov Phys Tech Phys 11 887 (1967)
15. V M Tkachenko and V E Tyutyunik, Radio Phys Quant Elect Translation of IZ.V.UZ Radio Fizika 16 1766 (1973)
16. A von Engel, Ionised gases, Oxford, at the Clarendon Press (1965)
17. E A Ballik, Appl Opt 5 170 (1966)
18. I Ya Fugal, D A Myshkis and O N Gregorshchenko, Opt and Spet 31 282 (1971)
19. H R Griem, Plasma Spectroscopy, McGraw-Hill Company (1964)
20. J M Anderson, Appl Phys 31 511 (1960)
21. H R Griem, A C Kolb and K Y Shen, Phys Rev 116 4 (1959)
22. H Margenau and M Lewis, Rev Mod Phys 31 569 (1959)
23. M Baranger and B Mozer, Phys Rev 115 521 (1959)

24. B Mozer and M Baranger, Phys Rev 118 626 (1960)

25. R G Breene Jr, The Shift and Shape of spectral lines, Pergamon Press, Oxford, London, New York, Paris (1961)

26. C R Vidal, J Copper and E W Smith, Ast Phys J Suppl 25 37 (1973)

27. A Maitland and M H Dunn, PhysFluids 6 586 (1963)

28. P Gill and C E Webb, J Phys D Appl Phys 10 299 (1977)

29. P Kepple and H R Griem, Phys Rev 173 317 (1968)

30. S C Brown, Basic Data of plasma physics, second edition, MIT Press (1966)

31. E W Rothe, L L Marina, R H Neynober and S M Treyilla, Phys Rev 125 582 (1962)

32. S J B Corrigan, Chem Phys 43 4381 (1965)

33. K T Compton, Phys Rev 22 333 (1923)

34. J D Cobine, Gaseous conductors, theory and engineering applications, Dover publication INC New York (1958)

35. J D Walker Jr and R M St John, Chem Phys 61 2394 (1974)

36. S Chapman and T G Cowling, The Mathematical Theory of non-uniform gases, Cambridge at the University Press (1952)

37. V A Ankudinov, S V Babashev and E P Andreev, Sov Phys JETP 21 26 (1965)

38. W L Wiese, M W Smith and B M Glennon, Atomic Transition probabilities NBS Washington DC (1966)

39. C Candler, Atomic Spectra and the vector Model, Hilger and Watts Ltd London (1964)

40. D E T F Ashby and D F Jephcott, Appl Phys Lett 3 13 (1963)

41. J B Gerardo and J E Verdeyen, Appl Phys Lett 3 121 (1963)

42. D A Baker, J E Hammel, and F E Jahoda, Rev Sci Inst 36 295 (1965)

43. J B Gerardo and J E Verdeyen, Proc IEEE 52 690 (1964)

44. J B Gerardo, J T Verdeyen and M A Gusinov, J Appl Phys 36 3562 (1965)

45. J B Gerardo and J T Verdeyen, J Appl Phys Lett 6 185 (1965)

46. J B Gerardo and M A Gusinov, J Appl Phys 40 2533 (1969)

47. H Malamud, Rev Sci Inst 36 1507 (1965)

48. J T Verdeyen, B E Cherrington and M E Fein, Appl Phys Lett 9 360 (1966)

49. C S Liu, J T Verdeyen and B E Cherrington, J Appl Phys 40 201 (1969)

50. O S Zuker, J Appl Phys 42 306 (1971)

51. J G Eden and B E Cherrington, J Appl Phys 44 4920 (1973)

52. A Dalgarno and A E Kingston, Proc Roy Soc 259 424 (1960)

53. J P Goldsborough, Appl Opt 3 267 (1964)

54. Hirschfelder, Curtiss and Bird, Molecular theory of liquids and gases, Wiley, New York, London (1954)

55. A Maitland and M H Dunn, Laser Physics, North Holland Publishing Company, Amsterdam (1969)

56. J W Foreman Jr, Appl Opt, 6 821 (1967)

57. A E Siegman, Proc IEEE 54 1350 (1966)

58. O E Delange, IEEE Spect 2 77 (1968)

59. A Maitland, Proposal for research and development of laser measurements techniques, University of St Andrews

60. C Freed, IEEE Quantum Elect 7 404 (1968)

61. A J Wallard, PhD Thesis, St Andrews University (1972)

62. C R C Handbook of Chemistry and Physics 53rd Edition (1972 - 1973)

63. W S Spinks, Vacuum Technology, Chapman and Hall (1963)

64. L B Loeb, The Kinetic Theory of Gases, McGraw-Hill Book Company Inc New York and London (1934)

65. R W Crompton, M T Elford and K L Jory, Aust J Phys 20 369 (1967)

66. H J Oskam, Philp Res Rep 13 352 (1958)

67. R Deloch, P Manichicort, M Cheret and F Lambert, Phys Rev A13 1140 (1976)

68. F E Niles and W W Robertson, J Chem Phys 42 3277 (1965)

69. G E Veatch and H J Oskam, Phys Rev 184 202 (1969)

70. A W Johnson and J B Gerardo, Phys Rev A5 1410 (1972)

71. J Berland, M Cheret, R Deloch, A Confalance and C Manus, Phys Rev A6 887 (1970)

72. M A Biondi and S C Brown, Phys Rev 75 1700 (1949)

73. J B Hasted, Physics of Atomic Collisions, London Butterworths (1964)

74. C B Collins, H S Hicks, W E Wells and R Burton, Phys Rev A6 1545 (1972)

75. C E Webb, J Appl Phys 39 5441 (1968)

76. H M Grimly and K G Emeleus, Brit J Phys 16 281 (1965)

77. C Popovici and M Somesan, Elect Lett 1 31 (1965)

78. P A Miller, J T Verdeyen and B E Cherrington, Phys Rev A4 692 (1971)

79. D R Long and R Geballe, Phys Rev A1 260 (1970)

80. L Vriens, T F M Bansen and J A Smith, Physica 40 229 (1968)

81. D J T Morrison and M R H Rudge, Proc Phys Soc 91 565 (1967)

82. A V Phelps and J P Molnar, Phys Rev 89 1202 (1953)

83. R M St John, F L Miller and C C Lin, Phys Rev 134 A888 (1964)

84. V S Borodin and Yu M Kagan, Opt and Spect 18 546 (1964)

85. V S Borodin and Yu M Kagan, Sov Phy Tech Phys 11 131 (1966)

86. Yu M Kagan and A S Taroyan, Opt and Spect 35 120 (1973)

87. A V Phelps, Phys Rev 99 1307 (1955)

88. R G Fowler, T M Holzberlein, C H Tozabron and S J B Carrigan, Proc Phys Soc 84 539 (1964)

89. V I Ochkur and A M Petrun'kin, Opt and Spect 14 245 (1963)

90. S P Varshavskii, A M Mityureva and N P Penkin, Opt and Spect 29 341 (1970)

91. L D Schearer and F A Padovani, J Chem Phys 52 1618 (1970)

92. E Vokaty and K Masek, Czeck J Phys B 22 776 (1972)

93. G J Collins, J Appl Phys 44 4633 (1973)

94. A G C Mitchell and M W Zemansky, Resonance radiation and excited atoms, Gambridge University Press (1961)

95. J A Harrison, Proc Phys Soc 73 841 (1959)

96. J F Sutton and R B Kay, Phys Rev A 9 697 (1974)

97. R J W Henry and J J Matese, Phys Rev A 14 1368 (1976)

98. E T P Lee and C C Lin, Phys Rev 138 A301 (1965)

99. N P Romanov, Opt and Spect, 26 376 (1969)

100. R J Anderson and R H Hughes, Phys Rev A 5 1194 (1972)

101. H F Wallenstein and W W Robertson, J Chem Phys 56, 1411 (1972).